

PhD Dissertation 13/2009

Well flows and root water uptake: Impact of local hydraulic properties on larger scale subsurface water extraction

Christoph Schneider

ISSN 1860-0387

Well flows and root water uptake:

**Impact of local hydraulic
properties on larger scale
subsurface water extraction**

Well flows and root water uptake:

**Impact of local hydraulic
properties on larger scale
subsurface water extraction**

Dissertation

zur Erlangung des akademischen Grades doctor rerum naturalium

(Dr. rer. nat.)

vorgelegt dem Rat der Chemisch-Geowissenschaftlichen Fakultät der

Friedrich-Schiller-Universität Jena

von

Dipl.-Ing. Christoph Schneider

geboren am 1. September 1980 in Schleiz/Deutschland

Supervisor: Prof. Dr. Sabine Attinger

Co-supervisor: Dr. Anke Hildebrandt

Diese Dissertation ist während meiner Beschäftigung als wissenschaftlicher Mitarbeiter am Department für Hydrosystemmodellierung innerhalb des Helmholtz-Zentrums für Umweltforschung - UFZ in Leipzig entstanden.

Promotionskommission:

Prof. Dr. Kai-Uwe Totsche	Friedrich-Schiller-Universität Jena, Vorsitzender
Prof. Dr. Sabine Attinger	Friedrich-Schiller-Universität Jena, Gutachter
Prof. Dr. Insa Neuweiler	Leibniz Universität Hannover, Gutachter
Prof. Dr. Georg Büchel	Friedrich-Schiller-Universität Jena
Prof. Dr. Sascha Oswald	Universität Potsdam

Die Dissertationsverteidigung fand am 21. Oktober 2009 in Jena statt.

This work was kindly supported by the Helmholtz Impulse and Networking Fund through the Helmholtz Interdisciplinary Graduate School for Environmental Research (HIGRADE).

ISSN 1860-0387

Copyright © 2009 by C. L. Schneider

All rights reserved. No part of the material protected by this copyright notice may be reproduced or utilised in any form or by any means, electronic or mechanical, including photocopying, recording or by any information storage and retrieval system, without the prior permission of the author.

Author email: christoph.schneider@ufz.de

Zusammenfassung. Der Anstieg der Weltbevölkerung und der Klimawandel werden die Menschheit in den nächsten 50 bis 100 Jahren vor große Herausforderungen stellen. Diese globalen Veränderungen werden sowohl zu einem Anstieg des Trinkwasserbedarfs als auch regionenspezifisch zu einem erhöhtem Wasseranspruch von Pflanzen führen. Von den Folgen auftretender Trockenperioden sind in Europa aktuell vor allem die Mittelmeerländer, insbesondere Spanien, betroffen. In solchen Gebieten kann der zu erwartenden Wasserknappheit nur durch intensivere Bewässerung des landwirtschaftlich genutzten Landes nachgekommen werden. Weltweit entstammen etwa 20 % des für Bewässerung eingesetzten Wassers dem Grundwasserspeicher, 50 % des Trinkwasserbedarfs und 40 % des industriellen Wasserverbrauchs werden durch die Nutzung von Grundwasser abgedeckt. Die weltweiten Auswirkungen sinkender Grundwasserstände aufgrund intensiver Wasserentnahme können in Gebieten wie der Nordchinesischen Ebene oder dem mexikanischen Mezquital Valley sowie in und um Großstädte wie Mexiko-Stadt, Bangkok, Sanaa, Tokio, Madras oder Shanghai beobachtet werden. Um die Wasserressourcen der Erde, besonders in den genannten Gebieten, nachhaltig nutzen und bewirtschaften zu können ist ein umfassendes Verständnis des hydrologischen Kreislaufs notwendig.

Der Mensch entnimmt dem Untergrund hauptsächlich aus tieferen Schichten Wasser, indem er Brunnen installiert. Pflanzen hingegen decken ihren Wasserbedarf hauptsächlich durch die Wurzelwasseraufnahme aus der oberen, ungesättigten Bodenzone ab. Um geeignete Aussagen über die momen-

tane Bewirtschaftung treffen zu können oder die Auswirkungen möglicher Szenarien vorherzusagen sind diese Prozesse nachzubilden. Modelle der Wasserentnahme aus dem Untergrund, sei es durch Brunnen oder durch Pflanzen, beziehen sich meist auf die Größenskala, auf der der Mensch verkehrt (im Meter- bis Kilometerbereich). Etablierte Modelle der Grundwasserentnahme gehen auf dieser Skala von einem Aquifer konstanter Leitfähigkeit aus. Der Extraktionsprozess wird dabei durch Brunnenfunktionen abgebildet. Gegenwärtige Vegetations- und Klimamodelle beinhalten eine Beschreibung der Wurzelwasseraufnahme auf der Skala ganzer Pflanzengemeinschaften. Beide Ansätze bilden den Einfluß kleinskaliger Prozesse durch die Verwendung einfacher, äquivalenter Parameter ab (äquivalente Leitfähigkeit bzw. Wurzeldichteverteilung). Die relevanten Fließprozesse solcher Wasserentnahmen finden jedoch auf kleinerer Skala statt und können durch solche Ansätze nur unzureichend beschrieben werden.

Der Grundwasserfluss wird durch die hydraulischen Eigenschaften des Aquifers bestimmt - natürliche Grundwasserleiter weisen dabei gleich auf mehreren Skalen räumliche Heterogenitäten dieser Eigenschaften auf. Darüber hinaus ist in der ungesättigten Bodenzone die Durchlässigkeit des Mediums zusätzlich durch den lokalen Wassergehalt charakterisiert. Der Wasserfluss im Boden wird dabei durch die nichtlineare Abhängigkeit der hydraulischen Leitfähigkeit vom Wasserpotential beeinflusst. Sinkt dieses ab, so verringert sich auch die ungesättigte Durchlässigkeit. Dieser Bereich kann je nach Bodenart mehrere Größenordnungen umspannen.

Das Hauptziel dieser Doktorarbeit ist es beide Extraktionsprozesse effektiv zu beschreiben und den Einfluss lokaler Inhomogenitäten bzw. Nichtlinearitäten hydraulischer Mediumseigenschaften auf den gesamten Entnahmeprozess zu quantifizieren. Dieser Arbeit liegt dabei die Annahme zu Grunde, dass lokale hydrologische Prozesse die Wasserentnahme auch auf einer größeren Skala beeinflussen. Der Einfluss dieser lokalen Eigenschaften entsteht durch die Ausbildung starker lokaler Strömungsgradienten innerhalb des radialen Fließfeldes. Den Begriff lokal verwenden wir hier stets gleichbedeutend mit sich in unmittelbarer Nähe der Entnahmestelle befindend.

Im ersten Teil untersuchten wir den Fall der Wasserentnahme aus einem gespannten Aquifer. Dieser liegt zwischen zwei nahezu undurchlässigen Schichten. Die Mächtigkeit des Grundwasserleiters wird als konstant angenommen, da der Wasserspiegel nicht über die obere Deckschicht steigen kann. Der hydraulische Druck in einem solchen Leiter liegt oberhalb dieser Schicht. Die auftretenden Brunnenströmungen können aufgrund der Ausrichtung des Fließfeldes in Radialkoordinaten beschrieben werden. Für den Spezialfall der Grundwasserentnahme aus Aquiferen konstanter Leitfähigkeit (homogene Grundwasserleiter) existieren analytische Lösungen. Dies sind im stationären Fall die Formel von Thiem und bei transienter Betrachtung die Brunnenformel von Theis. In dieser Arbeit wird von der realistischeren Bedingung einer Grundwasserentnahme aus einem heterogenen Aquifer ausgegangen. Die hydraulischen Eigenschaften werden dabei einer statis-

tischen Verteilung folgend durch die Parameter Mittelwert, Varianz und Korrelationslänge beschrieben.

Zur Charakterisierung von Grundwasserbrunnenströmungen durch äquivalente hydraulische Eigenschaften heterogener Medien existiert bereits eine Reihe von wissenschaftlichen Arbeiten. Äquivalente Werte werden in diesen Arbeiten als homogene Ersatzwerte des subskaligen Grundwasserflusses auf der betrachteten Skala angesehen. In dieser Arbeit wählen wir für die Beschreibung der Grundwasserentnahme einen anderen Ansatz. Wir unterscheiden hierzu zwischen bisherigen äquivalenten und der hier verwendeten adaptiv-vergrößerten (coarse grained) Eigenschaft des Mediums. Die Methode des Coarse Graining ist eine räumliche Mittelungsprozedur. Die Volumenmittlung wird auf die Gleichung der radialen Grundwasserbrunnenströmung angewendet. Die Filterbreite des Coarse Graining ist in diesem Fall radial-abhängig. Die Anwendung der Methode resultiert in einer adaptiv-vergrößerten hydraulischen Eigenschaft, die als Funktion des radialen Abstands zum Brunnen die Druckgradienten und den jeweiligen Wasserfluss an allen Punkten des Strömungsfeldes verbindet. Die adaptiv-vergrößerte Beschreibung gilt im Unterschied zum äquivalenten Parameter gleichzeitig an verschiedenen Radien der Brunnenströmung des durch das heterogene Medium fließenden Grundwassers. Dieser Ansatz berücksichtigt besonders die lokalen hydraulischen Prozesse in der Nähe des Pumpbrunnens, d.h. die auftretenden Strömungsgradienten und den Einfluss der lokalen Wasserdurchlässigkeit.

Die hydraulische Leitfähigkeit eines heterogenen Aquifers kann über mehrere Skalen variieren. Wir führten für die Modellierung der Grundwasserbrunnenströmung eine Skalenseparierung der Heterogenitäten durch und unterschieden dabei zwischen großskaligen (Meter bis Kilometer) und kleinskaligen (Zentimeter bis Meter) Brunnenströmungen. Auf dieser kleinen Skala ist die hydraulische Konduktivität die den Wasserfluss dominierende Variable. Kleinskalige Brunnenströmungen besitzen eine Ausdehnung im Bereich von mehreren Metern und sind somit durch das heterogene Konduktivitätsfeld charakterisiert. In diesem Fall liegt die Aquifermächtigkeit im Längenbereich der horizontalen Fließprozesse. Deshalb untersuchten wir kleinskalige Pumpversuche für künstliche Aquifere, die Heterogenitäten in horizontaler als auch vertikaler Richtung aufweisen.

Vergrößert man den betrachteten Bereich auf Meter bis Kilometer, so treten neue Heterogenitäten in den hydraulischen Eigenschaften des Mediums auf. Auf dieser Skala ist es die hydraulische Transmissivität des Aquifers, die den Grundwasserfluss bestimmt. Großskaligere Brunnenströmungen dehnen sich bis zu mehreren hundert Metern aus und werden somit von den Heterogenitäten des Transmissivitätsfeldes beeinflusst. Die horizontale Ausbreitung des Absenktrichters liegt dabei um ein vielfaches über der vertikalen Ausdehnung des Aquifers. Dieser Umstand lässt es zu die Auswirkung des heterogenen Transmissivitätsfeldes auf die Brunnenströmung nur in horizontaler Richtung zu untersuchen. Wir begannen daher zunächst mit einer

Betrachtung großskaliger Brunnenströmungen, dem sich die kleinskaligen Untersuchungen in allen drei Raumdimensionen anschlossen.

Die adaptiv-vergrößerte Gleichung wurde auf beiden Skalen der Grundwasserentnahme, d.h. sowohl für die größerskalige Transmissivität als auch für die kleinerskalige Konduktivität, durch Anwendung der Methode des Coarse Graining und einer Renormierungsgruppenanalyse abgeleitet. Zunächst betrachteten wir den Einfluss der Transmissivität auf großskalige Brunnenströmungen. Als ein wichtiges Ergebnis stellte sich heraus, dass großskalige Brunnenströmungen vor allem in der Nähe des Extraktors stark von der lokalen Transmissivität abhängen. Im Fernfeld des Pumpversuchs nähert sich die adaptive-vergrößerte Transmissivität dem äquivalenten Wert für eine uniforme Strömung, dem geometrischen Mittel des Transmissivitätsfeldes, an. Der Übergang zwischen der lokalen Transmissivität im Nahfeld und dem geometrischen Mittel im Fernfeld wird durch die (horizontale) Korrelationslänge bestimmt. Für den Fall einer Ensemble Mittelung mehrerer Pumpversuche entfiel der Einfluss der lokalen Transmissivität auf den gemittelten Absenktrichter und wurde in der adaptiv-vergrößerten Transmissivitätsformel durch das harmonische Mittel ersetzt. Dieses ist über das geometrische Mittel und die Varianz des Feldes definiert. Die statistischen Parameter des heterogenen Transmissivitätsfeldes wurden mittels Monte-Carlo-Simulationen künstlicher Pumpversuche invers abgeschätzt.

Die Ergebnisse großskaliger Pumpversuche übertrugen wir auf Brunnenströmungen kleinerer Ausdehnung. Diese kleinskaligen Pumpversuche wer-

den durch die sowohl in vertikale als auch horizontale Richtung variierende Leitfähigkeit beeinflusst. Die Methode des Coarse Graining wurde aus diesem Grund auf eine dreidimensionale Mittelungsprozedur erweitert. Dies resultiert in einer Formulierung des hydraulischen, adaptiv-vergrößerten Konduktivitätsfeldes. Zusätzlich zu dem geometrischen Mittel, der horizontalen Korrelationslänge und der Varianz kommt in dieser Gleichung noch der Einfluss des Anisotropieverhältnisses zum Tragen. Dieses Verhältnis ist als der Quotient zwischen horizontaler und vertikaler Korrelationslänge definiert. Ähnlich zu der inversen Abschätzung der Parameter großskaliger Pumpversuche wurden die vier genannten statistischen Parameter des adaptiv-vergrößerten Konduktivitätsfeldes für kleinskalige Brunnenströmungen abgeschätzt.

Der zweite Teil dieser Arbeit beschäftigt sich mit der Modellierung der pflanzlichen Wurzelwasseraufnahme aus dem Boden, der sogenannten ungesättigten Zone. Ähnlich der Grundwasserentnahme aus der gesättigten Zone wird hierfür in die Wasserflussgleichung für die ungesättigte Zone (Richards Gleichung) ein Senkenterm eingeführt. An Stelle der Wasserentnahme durch den Pumpbrunnen trat die Wasserextraktion durch die Pflanze. In Analogie zum ersten Teil der Arbeit erforschten wir den Einfluss der hydraulischen Eigenschaften in unmittelbarer Nähe der Senke, d.h. der Wurzel, auf den gesamten Wasserextraktionsprozess der Pflanze. Da die hydraulischen Eigenschaften des Bodens im Unterschied zur Grundwassergleichung auch vom lokalen Wassergehalt abhängen, ist die Richards Gleichung, die

die Wasserbewegung der ungesättigten Zone beschreibt, nichtlinear. Interessierte uns in den Studien zur Grundwasserentnahme die räumliche Heterogenität der Leitfähigkeiten, stand in diesem Teil der Dissertation die Nichtlinearität der Potential-Fluss-Beziehung im Mittelpunkt unserer Untersuchungen der Wurzelwasseraufnahme.

Die Wurzelwasseraufnahme wird in aktuellen Vegetations- und Klimamodellen durch eine bewuchsspezifische Wurzeldichteverteilung parametrisiert. Dabei wird dem Bodenwassermodell ein Ausdruck für die vertikale Wurzelwasseraufnahme entlang der Bodentiefe hinzugefügt. Dieser Senkenterm ergibt sich, in dem der atmosphärische Transpirationsbedarf der betrachteten Pflanzenart über die Wurzeldichteverteilung auf die Bodenschichten verteilt wird. Der Wasserbedarf der Pflanze wird durch ein Potentialkonzept ausgedrückt - der Wasserfluss findet entlang eines Druckgradienten zwischen Bodenwasser und Atmosphäre statt. Das Austrocknen einzelner Schichten führt in diesen Modellen zu einer reduzierten Wasseraufnahme und damit zu einer verringerten Transpiration.

Die Annahme, dass eine erhöhte Wurzeldichte zu einer erhöhten Wasseraufnahme beiträgt, basiert auf der Vorstellung, dass die Vergrößerung der Wasseraufnehmenden Fläche zu erhöhten Aufnahmeraten führt. Ein Problem dieser Art von Parametrisierung der Wurzelwasseraufnahme begründet sich darin, dass der Zusammenhang zwischen Wurzelstruktur und Wasseraufnahme durch Wurzeldichteverteilungen unzureichend repräsentiert ist. Des Weiteren ist auch der radiale Anstrom des in Wurzelnähe befindlichen

Bodenwassers in solchen Modellen unzureichend abgebildet, obwohl diese den Gesamtaufnahmeprozess beeinflussen. Aktuelle Studien zeigen, dass nicht die Aufnahme­fläche allein, sondern vor allem die Potentialverteilungen im Wurzel- und Bodensystem verantwortlich für die Wasseraufnahme sind. Dies ist im Einklang mit der Beobachtung, dass Pflanzen bei gleicher Wurzeldichte­verteilung, entsprechend den momentanen Bodenfeuchtebedingungen ihre Wasseraufnahmeprofile deutlich ändern können. Hierzu müssen zwei Prozesse zusammen betrachtet werden: (1) Der Wasserfluss innerhalb des Bodens zur Wurzel hin, sowie (2) der Wasserfluss innerhalb des Wurzelsystems bis zum Übergang in den Stamm.

In dieser Arbeit wurde der Wasserfluss innerhalb des Bodens zur Wurzel zunächst in einem "Split root experiment" numerisch nachgebildet. Dazu modellierten wir die Wasserentnahme aus zwei Bodenkompartmenten gleicher räumlicher Dimension und hydraulischer Eigenschaften, aber unterschiedlicher Durchwurzelungsdichte. Der Fokus lag dabei auf der Untersuchung des Einflusses der lokalen hydraulischen Gradienten des Wasserpotentials in Wurzelnähe. Es zeigte sich, dass die zeitliche Entwicklung dieser Gradienten in dem jeweiligen Bodenkompartment das Gesamtwasseraufnahmeverhalten beeinflusste. Obwohl die Wurzeldichte in beiden Schichten konstant gehalten wurde, veränderte sich die Verteilung der Entnahmeraten zwischen den beiden Bodenschichten über die Zeit hin beträchtlich. Dies war besonders in der Periode der Fall, als der Bodenwassergehalt noch nicht limitierend auf die Wasseraufnahme wirkte. Unsere Ergebnis-

se bestätigen die Annahme, dass in Vegetations- und Klimamodellen die Modellierung der Wasseraufnahme über die Wurzeldichtevertelung zu einer Unterschätzung der Wasserentnahme aus weniger stark durchwurzelten Schichten führt. Diese klassischen Ansätze zeigen demzufolge eine verfrühte Verringerung der pflanzlichen Transpirationsleistung.

Eine bedeutende Rolle für die Vorhersage der Wasseraufnahme gesamter Wurzelsysteme spielt die korrekte Vorhersage des Wasserpotentials an der Schnittstelle zwischen Wurzel und Boden. Dessen richtige Abschätzung ist das Ziel des letzten Abschnittes dieser Doktorarbeit, indem die Wurzelwasseraufnahme für explizite Architekturen modelliert wurde. Die Verteilung des Wasserpotentials innerhalb der Wurzel hängt in erster Linie von den auf diesem Fließpfad zu überwindenden hydraulischen Widerständen ab. Dabei unterscheidet man den radialen Fließpfad vom Wurzeläußeren über den Cortex zu dem Xylem und den axialen Fließpfad innerhalb der Wasserleitbahnen des Wurzelxylem. Der Wertebereich der hydraulischen Wurzelwiderstände für den radialen und axialen Fluss werden innerhalb der wissenschaftlichen Gemeinschaft anhaltend diskutiert. Während die axialen hydraulischen Wurzelwiderstände durch das Poiseuillesches Gesetz durch die Anzahl, den Radius und die Länge der Leitbahnen relativ gut beschrieben werden können, weisen experimentelle Messungen des radialen Fließwiderstandes verschiedener Studien eine Variabilität von mehr als einer Größenordnung auf. Aus diesem Grund simulierten wir die Wurzelwasseraufnahme parallel für zwei Szenarien mit stark unterschiedlichen radialen

hydraulischen Widerständen. Diese wurden dabei altersabhängig durch ihre Wurzelordnung parametrisiert. Das für diese Aufgabe entwickelte Wurzelwasseraufnahmemodell beinhaltet sowohl den Anstrom des Bodenwassers an die einzelnen Wurzeln als auch den Wasserfluss innerhalb des explizit generierten Wurzelsystems. Während die Wurzelarchitektur in diesem Modell die räumliche Verteilung möglicher Wasserentnahmestellen im Boden vorgibt, sorgt die Verteilung des Wasserpotentials im Wurzelsystem für die anzunehmenden Aufnahmeraten an den jeweiligen Stellen. Um statistische Aussagen über das Aufnahmeverhalten einzelner Pflanzen gleichen Typs treffen zu können, wurden wiederholt Simulationen für verschiedene Realisierungen von Wurzelsystemarchitekturen einer bestimmten Pflanzenart (Sorghum) durchgeführt. Unsere Resultat zeigen, dass sich die Wasseraufnahme innerhalb verschiedener Individuen der gleichen Art unterscheidet. Je nach Parametrisierung des radialen Wurzelwiderstandes äußert sich dies (1) für geringere radiale Widerstände in stark variierenden Wasseraufnahmeprofilen über die Bodentiefe trotz vergleichbarer Wurzeldichtevertelung oder (2) für höhere radiale Widerstände in stark unterschiedlichen Wasserpotentials innerhalb des Wurzelsystems der einzelnen Realisierungen. Diese Ergebnisse sind ein wichtiger Beitrag zur Verbesserung gegenwärtiger Implementierungen der Wurzelwasseraufnahme in Vegetations- und Klimamodellen.

Zusammenfassend verdeutlicht diese Arbeit die Relevanz subskaliger Prozesse für die Wasseraufnahme von Pflanzen als auch für die Grundwas-

serentnahme. Wenn die Gesamtaufnahme auf größerer Skala richtig abgeschätzt werden soll, müssen demzufolge lokale Prozesse in Betracht gezogen werden. Parametrisierungen durch äquivalente Mediumseigenschaften sind zu diesem Zweck nicht ausreichend.

Abstract. This thesis deals with describing the flow of subsurface water towards a sink. We investigate the local impacts of hydraulic properties close to the extractor on the overall flow process. This is done for two examples of water extraction, that is well pumping groundwater and root water uptake from the soil.

Although these two topics, root water uptake and well pumping, differ in many ways, they also share some similarities. Regarding the flow process, in both cases water moves along a radial pathway through a porous medium towards the point of discharge. The water potential field that drives the water flow hence develops strong gradients in the vicinity of the sink.

Nevertheless, root water uptake and well pumping show important differences considering the flow process. While water uptake of plant roots occurs in the unsaturated zone, groundwater is pumped from the saturated zone. Studying water flow in the unsaturated zone becomes complicated by the fact that the hydraulic conductivity depends not only on the porous media material properties, but is also a nonlinear function of the soil water potential.

For a confined, fully saturated aquifer, hydraulic conductivity does not depend on the water potential itself. In this case, assuming the subsurface hydraulic properties to be homogeneous, analytical solutions can be derived (Theis and Thiem approach). However, aquifers typically exhibit spatial heterogeneities at multiple scales. Taking this into account, we applied a spatial filtering procedure (Coarse Graining) to the radial flow equa-

tion governed by the heterogeneous character of the pumped aquifer. The coarse grained field is supposed to represent both, the statistical properties of the heterogeneous aquifer and the corresponding process quantities like hydraulic head and discharge simultaneously. Whether the aquifer's corresponding hydraulic property is transmissivity or conductivity depends on the scale of pumping. Here, we use a separation of scales and divide typical well flows into small scale (a few meters) and large scale (hundreds of meters). Thus, we applied two concepts, (1) one for the interpretation of large scale well flows governed by the coarse grained aquifer transmissivity and (2) the other for deriving the coarse grained conductivity field for small scale well flows.

The second part of this thesis is concerned with modeling the below ground mechanism of root water uptake. Compared to well flows, we still focused on applying a sink term to the flow equation. Here, the water is removed by the plant root. For water flow in the unsaturated zone, the flow equation is highly nonlinear since the hydraulic conductivity depends on soil water potential. Thus, we considered rather the nonlinearity in the flow-to-potential relationship than the spatial heterogeneities. Similarly as in the well flow study, the hydraulic properties in the vicinity of the sink (root) affect the water extraction process significantly because of the local conductivity drop when soil dries out.

In a first step, we investigated how local hydraulic gradients in soil water potential influences overall root water uptake. For this we apply a numerical

split root model experiment with two soil compartments of same size and soil hydraulic properties but different rooting density. We show that the temporal development of the local gradients influences the pattern of root water uptake. While rooting density distribution stayed constant with time, the distribution of root water uptake changed considerably, particularly for the period when soil moisture was not yet limiting uptake. We find that the parameterizations in SVAT models tend to underestimate water uptake from less densely rooted layers.

Besides regarding the potential gradients in the vicinity of the root, in the last part of this thesis we included another significant process at the plant scale that is the variation of potentials within the root system. Therefore, we simulated the water uptake of an ensemble of root system realizations. Our results suggest that root water uptake behavior might vary greatly between individuals of a particular species. This challenges the state-of-the-art approach modeling root water uptake at the soil plant continuum by using a vertical function of root abundance. Additionally the developed root water uptake model was able to give a precise estimate of the water potential at the root collar that is necessary for extracting a given amount of water from the soil.

In summary, this dissertation shows two examples where small scale hydraulic properties close to the water extraction point strongly influence larger scale water extraction. In this cases, local subscale processes need to be taken into account in order to model the system behavior on the scale of

human interaction. This thesis proposes solutions to describe, model and quantify this subscale effects of water extraction from the subsurface.

List of Symbols and Abbreviations

Symbol	Description
r [m]	radial distance
x, y, z [m]	cartesian coordinates
t [s]	time
h [m]	hydraulic head
ψ [m]	matric potential
Φ [m ² s ⁻¹]	matric flux potential
ϱ [m ³ m ⁻³ s ⁻¹]	rate
q, v [m s ⁻¹]	volumetric flux
J, Q, S [m ³ s ⁻¹]	volumetric flow rates
θ [m ³ m ⁻³]	volumetric water content
Θ [m ³ m ⁻³]	normalized (or relative) water content
K [m s ⁻¹]	hydraulic conductivity
D [m ² s ⁻¹]	hydraulic diffusivity
κ [m ² s ⁻¹]	hydraulic conductance
T [m ² s ⁻¹]	hydraulic transmissivity
R [sm ⁻²]	hydraulic resistance
C [m ⁻¹]	water capacity/storativity
r_w [m]	well radius
r_d [m]	outer domain radius (range of pumping test)
z_a [m]	aquifer thickness

ξ_i [m]	correlation length in i-th direction
I_h, I_v [m]	horizontal/vertical integral scale
σ_f [–]	variance
e [–]	anisotropy ratio
w_f [–]	correlation function
ϕ [–]	soil porosity
θ_s [–]	saturated volumetric water content
θ_r [–]	residual volumetric water content
α [m ^{–1}]	soil specific parameter
n [–]	soil specific parameter
m [–]	soil specific parameter
r_0 [m]	root radius
r_b [m]	radial distance from root center to the point where bulk water potential appears
r_d [m]	half root distance
r_{disc} [m]	radial disc size
l_r [m]	root segment length
$l_r^a(z)$ [m]	accumulated root length at depth z
$P_{l_r}(z)$ [–]	fraction of total root length at depth z
L_l^a [m m ^{1–}]	accumulated root length per soil depth
L_V^a [m m ^{–3}]	accumulated root length per volume (RLD)
z_d [m]	rooting depth

$\Delta z_k [m]$	thickness of soil layer k
$K_{pr} [m s^{-1}]$	root radial hydraulic conductivity
$\chi_{pr} [sm^{-1}]$	root radial hydraulic resistivity
$R_r [sm^{-2}]$	root radial hydraulic resistance
$R_a [sm^{-2}]$	root axial hydraulic resistance
$r_c [m]$	radial thickness of the root cortex
$\nu [s^{-1}]$	ordinary frequency
RLD	Abbrev. for root length density
RWU	Abbrev. for root water uptake

“The little things.

The big things in life.”

The Lost Patrol

Contents

Zusammenfassung / Abstract	I
List of Symbols and Abbreviations	XVII
1 Introduction	1
1.1 Motivation	1
1.2 Outline	4
2 Theoretical background I: subsurface water flow and well flows	11
2.1 Flow in porous media	11
2.1.1 Porous media	12
2.1.2 Transition to continuum scale	12
2.1.3 Mass balance: continuity and diffusion equation . . .	14
2.2 Subsurface	17
2.3 Groundwater flow	19
2.3.1 Well flows: radial groundwater flow	20

2.3.2	Natural heterogeneity of hydraulic properties	23
2.3.3	Separation of scales	27
3	Large scale well flows in the saturated zone	35
3.1	Introduction	35
3.2	Model	44
3.3	The concept of equivalent and coarse grained conductivity .	45
3.4	Coarse Graining radially convergent flow toward a well . . .	48
3.4.1	Uniform filtering	50
3.4.2	Nonuniform spatial filter for radially convergent flow toward a well	54
3.4.3	Numerical simulations	55
3.5	Interpreting an ensemble of pumping tests	59
3.5.1	Results for coarse grained transmissivities	63
3.5.2	Convergence of ensemble averaging	65
3.6	Interpretation of single pumping tests	68
3.7	Inverse modeling	73
3.7.1	Estimating correlation length and geometric mean .	74
3.7.2	Estimating the field Variance in ensemble averaged drawdowns	76
3.8	Conclusion	77
4	Interpreting small scale pumping tests	87

4.1	Introduction	87
4.2	Model	90
4.3	Coarse Graining for 3-dimensional short range well flows . .	91
4.4	Inversion of 3-D pumping test data by Firmani et al. (2006)	95
4.4.1	Numerical setup	96
4.4.2	Step I: estimation of horizontal integral scale, geometric mean and variance	98
4.4.3	Step II: additional estimation of anisotropy ratio . .	100
4.4.4	Limitations of the proposed procedure	103
4.5	Summary and conclusion	103
4.6	Appendix	105
5	Theoretical background II: unsaturated water flow and root water uptake	109
5.1	Soil water flow	110
5.2	Root water uptake	114
6	The split root modeling study in the unsaturated zone	129
6.1	Introduction	129
6.2	Background	133
6.3	Methods	136
6.3.1	Microscale Models Type I, Richards' equation for flow towards a single root	137

6.3.2	Microscale Model Type II: Simplifications for flow towards a single root	140
6.3.3	Microscale Model Type III: Inclusion of root radial resistance	140
6.3.4	Special case: root-water uptake for a split root experiment in linear soil	142
6.3.5	Macroscale Model	143
6.3.6	Model Scenarios and Input	143
6.4	Results	145
6.4.1	Modeled macroscopic uptake considering only soil resistance with a nonlinear Richards' equation	145
6.4.2	Comparison with simplified approaches	150
6.4.3	Modulation of macroscopic water uptake by plant factors: plant resistance	153
6.5	Discussion	156
6.6	Conclusion	161
6.7	Appendix: Derivation of the Linear Split Root Experiment	164
7	Effects of root system on plants water uptake	175
7.1	Introduction	175
7.2	Models and methods	179
7.2.1	Bulk water flow in the unsaturated zone	180
7.2.2	The hydraulic root water uptake model "aRoot"	182

7.2.3	The root architecture model	191
7.2.4	The RLD model	193
7.2.5	Model input and scenarios	193
7.3	Results	195
7.3.1	Influence of root architecture and hydraulic root pa- rameters on root water uptake behavior	195
7.3.2	Influence of root architecture on uptake profiles . . .	197
7.3.3	Influence of root architecture on critical point of wa- ter uptake limitation	200
7.4	Discussion	204
7.5	Summary and conclusions	207
8	Synthesis	217
8.1	Summary and Conclusions	217
8.2	Outlook	222
	Acknowledgements/Danksagung	227
	Curriculum Vitae	231

Chapter 1

Introduction

1.1 Motivation

Water stored in the surface and subsurface is essential for humans and all other known forms of terrestrial life. But only about 1 percent of the fresh-water available on Earth is easily accessible surface water stored in rivers, lakes or man made storage facilities (0,105 million km^3), where another 1 percent counts for net precipitation falling on land. The vast majority, namely 98 percent of the available fresh water, is stored in the subsurface that is mainly groundwater and to a less extent soil moisture (together 10,53 million km^3 , all data by Gleick (1996)).

Today, the total global groundwater withdrawal is estimated to be between 600 and 700 km^3 /year (Zektser and Everett, 2006). In this sense, groundwa-

ter provides about 70% of the piped water supply in the European Union, it forms a cornerstone of the Asian “green agricultural revolution” and supports rural livelihoods across extensive areas of sub-Saharan Africa (after Foster and Chilton (2003)). Groundwater is available almost everywhere on Earth, but cannot always be reached easily. Globally it is estimated to provide at least 50% of current potable water supplies, 40% of the industrial water demand and 20% for water use in irrigated agriculture (Zektser and Everett, 2006).

The unsaturated soil reservoir forms only a minor water storage compared to groundwater. While groundwater reservoirs residence times are often counted in decades, centuries or even millennia, water resides in the soil reservoirs on much shorter time scales due to its smaller dimensions. Soil water either stems directly from rainfall or indirectly from agricultural irrigation. The principle users of soil water are plants. Water that is stored in this part of the subsurface plays a fundamental role for vegetation growth and composition. However, most of the water that enters the plant via its roots does not stay there. Less than 1% of the water withdrawn by the plant is actually assimilated. The rest of the water moves to the leaf surfaces where it transpires to the atmosphere while stomata are open for carbon uptake. This shows that soil moisture also affects the feedback between the atmospheric water reservoir and the terrestrial part of the Earth (Rodriguez-Iturbe et al., 2007).

Soil water content is important for the water cycle such as for evapotranspiration, the generation of overland flow or groundwater recharge by percolation. The movement of water on, above, and below the surface is affected by global change. The 2008 IPCC report on climate and water (Bates et al., 2008) states that observed warming over several decades has been linked to changes in the hydrological cycle such as increasing atmospheric water vapor content, changing precipitation patterns, intensity and extremes and changes in soil moisture and runoff. Supplementary, the latest world water development report (World Water Assessment Programme, 2009) notes that the demand for freshwater will increase by about 64 billion cubic meters a year due to population growth. The majority of the additional three billion people expected by 2050 will be in developing countries, where many of these regions are already water scarce.

Due to the expected global changes, the need for water will increase worldwide. Also, the dynamics of the water cycle will alter under the described modifications. Not only, but especially because of these expected changes, a sound understanding of the underlying processes is required to develop sustainable management tools. For this aim, models have been developed. Many of these models operate at the scale of human interest, that is at the landscape scale of tens of meters up to several kilometers. For example, groundwater extraction is very often modeled by well functions (Theis or Thiem model) assuming the medium to be homogeneous. Plant available water is estimated by vegetation specific water uptake functions.

A discrepancy often exists in these models between the scale of human interaction and the scale where the relevant process occurs. For example, geologic structures of aquifers are neglected, if they are smaller than the resolution of the groundwater flow model or, soil water extraction by plants is often described as water removal from the bulk soil although the process of water flow in both cases takes place at much smaller scale.

The focus of this work is on two examples of water extraction from the subsurface, one from saturated and one from unsaturated media: well pumping and root water uptake. In both cases local processes show an impact on the larger scale. In one case this is due to the small scale heterogeneity of the hydraulic aquifer, in the other it is caused by the water saturation dependent hydraulic properties of soil, both in combination with steep local flux gradients.

Our main hypothesis is that singular small scale hydraulic properties close to the water extraction point essentially determine larger scale water removal. In a more general form, this hypothesis has been revealed many times in the field of upscaling theory.

1.2 Outline

Chapter 2 will shortly introduce the theory of water flow through porous media. It especially covers the aspects of radial groundwater flow and therefore motivates the following Chapters 3 and 4. These both have in

common that the concept of Coarse Graining is applied to a radial field of water flow through a heterogeneous confined aquifer. However, we will make the distinction between large (Chapter 3) and small scale (Chapter 4) well flows and particular stress the differences between current approaches of introducing heterogeneity into radial groundwater flow and our coarse grained approach.

In Chapter 3, we investigate numerically the effects of spatial heterogeneity of hydraulic transmissivity on the performance of large scale well flows. We propose a procedure for estimating the statistical properties of the heterogeneous transmissivity field under radial flow conditions and present a new mathematical approach for interpreting an ensemble and single large scale pumping tests. By applying the spatial filtering technique Coarse Graining, we derive an explicit formula for the coarse grained aquifer transmissivity. Repeating numerical pumping tests over several aquifer realizations (Monte Carlo Simulations), we test the applicability of the derived formula for nonuniform radial flow configurations and show results for the statistical parameter estimates like the mean, variance and correlation length.

The established method for interpreting large scale pumping tests (Chapter 3) is extended to small scale pumping tests in Chapter 4. Starting at the larger scale and then extend these findings to the smaller scale is due to reasons of simplicity. Since the aquifer can be treated as quasi two-dimensional at the large scale, it releases the progression of the proposed procedure. In contrast small scale well flows have to be interpreted in

three dimensions. This is due to the fact that the vertical extent (aquifer thickness) is within the same order of magnitude as the horizontal extent. Therefore, the heterogeneity of the hydraulic conductivity varies in both, the horizontal and the vertical direction. Focusing on the small scale interpretation in Chapter 4, we develop a method to estimate the statistical properties of the hydraulic conductivity field. In addition to the parameters geometric mean, horizontal correlation length and variance, our inverse estimation procedure will include also the anisotropy that characterizes the ratio between the horizontal and vertical correlation length.

In Chapter 5 we complete the derivation of general principles for water flow in the subsurface that is the water flow in the unsaturated zone and especially root water uptake.

Regarding the root water uptake in the unsaturated zone, we focus on the nonlinear nature of soil water flow. Therefore, we investigate the effect of the local hydraulic conductivity decrease around roots when soil gets dry. This is explored by a numerical split root experiment within Chapter 6. Simulating the water uptake from two compartments of different root density, we test the applicability of the widely used root length density approach for parameterizing root water uptake.

In Chapter 7, we will extrapolate these findings to the root system scale. In contrast to the split root experiment, plant water uptake is simulated for explicit root architectures. We present a stand alone root water uptake model (named aRoot), which calculates the sink term for any bulk soil

water flow model taking into account water flow within and around a root network. The variable determining the plant regulation for water uptake in our approach is the soil water potential at the soil-root interface. We apply this model to investigate the role of root architecture on the spatial distribution of root water uptake.

Some overlap exist between the theoretical Chapters 2 and 5 and Chapters 3, 4, 6 and 7. This was unavoidable since the latter are self explanatory paper based manuscripts that have been or will be published in scientific journals.

Bibliography

- Bates, B.C. et al. (2008). *Climate Change and Water*. Tech. rep. Intergovernmental Panel on Climate Change, IPCC Secretariat, Geneva.
- Foster, S. S. D. and P. J. Chilton (2003). “Groundwater: the processes and global significance of aquifer degradation”. In: *Philosophical Transactions B* 358, pp. 1957–1972. DOI: 10.1098/rstb.2003.1380.
- Gleick, P. H. (1996). *Water resources*. Ed. by S. H. Schneider. Vol. 2. Encyclopedia of Climate and Weather. New York: Oxford University Press, pp. 817–823.
- Rodriguez-Iturbe, Ignacio et al. (2007). “Challenges in humid land ecohydrology: Interactions of water table and unsaturated zone with climate, soil, and vegetation”. In: *Water Resour. Res.* 43.W09301. DOI: 10.1029/2007WR006073.
- World Water Assessment Programme (2009). *The United Nations World Water Development Report 3: Water in a Changing World*. Tech. rep. Paris: UNESCO, and London: Earthscan.

Zektser, Igor S. and Lorne G. Everett, eds. (2006). *Ground Water Resources of the World and Their Use*. National Ground Water Association, p. 346.

Chapter 2

Theoretical background I: subsurface water flow and well flows

2.1 Flow in porous media

This section deals with water flow in the subsurface and its derivation of first principles. Here, we regard the subsurface as a porous media. The theoretical part of flow in porous media was inspired by the lecture notes of Roth (2007) and is based on the books of Bear (1988) and Maidment (1993).

2.1.1 Porous media

Either consolidated or unconsolidated rock, both geological materials can be regarded as porous media. The most significant properties of a porous medium are defined as:

1. The solid matrix and the pore space (filled by water) together accumulate to the total volume of the medium.
2. Down to a minimal volumetric element of a characteristic size, both solid matrix and pore space are present.
3. Regarding water flow, we focus only on the hydraulically connected fraction of the pore space.

A porous medium owns different properties. It is characterized by its porosity and in terms of water flow by its ability to hold and release water and also by the ability of the material to transmit water. The latter two quantities are mainly related to the pore size of the media and its material composition.

2.1.2 Transition to continuum scale

Describing the water flow processes at the pore space in detail is not feasible for most domains of practical environmental interest. The pore geometry of the media and corresponding pore-scale phenomena own relevant lengths in the range of micrometers while environmental systems extend orders of

meters or higher. To bridge this gap in scales, the pore space and its processes are transferred to the continuum scale. The outcome of this transition are macroscopic field variables that still describe the observed phenomena.

REV Groundwater and soil water flow equations are defined on the basis of a representative elementary volume (REV). At a macroscopic level, a certain point $P(x, y, z)$ could be treated as a REV within the porous media. At the pore scale, this point would belong to one of the phases, either to the solid or to the fluid matrix.

To sum up the following conditions for the REV must be kept:

- small enough to be regarded as a point on the macroscopic scale
- large enough that the variables velocity and head concerning this volume remain stable/steady

In hydrogeology, the representative elementary volume (REV) is the smallest volume over which a measurement can be made that will yield a value representative of the whole. Below REV, the parameter is not defined and the material cannot be treated as a continuum.

In order to establish a given porous medium's property, samples of the porous medium are measured (as plotted in Figure 2.1). If the sample is too small, the measuring tend to oscillate. As we increase the sample size, the oscillations begin to dampen out. Eventually when the sample size becomes large enough the measuring become more consistent. This

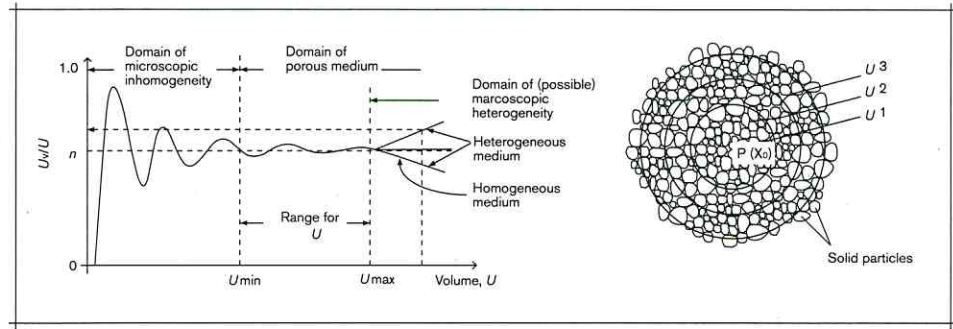


Figure 2.1: Definition of the representative elementary volume (REV) in accordance to Bear and Bachmat (1990) with n referring to the ratio between the volume of void space U_v within U .

sample size is referred to as the representative elementary volume. If we continue to increase our sample size, measurements will remain stable until the sample size becomes large enough that other hydrostratigraphic layers can be included. This is referred to as the maximum elementary volume (MEV).

2.1.3 Mass balance: continuity and diffusion equation

The continuity equation is derived from the principle of mass conservation of the fluid. The mass balance states that the mass variation over time for a representative volume (REV) in a certain medium is equal to the difference between the mass flowing across the boundaries of the REV and additional sinks/sources within the volume. Using the divergence theorem to turn the flux across the boundary into a flux over the entire volume, the final form

of the groundwater flow equation (in differential form) is:

$$C \frac{\partial h}{\partial t} = -\nabla \mathbf{v} + \varrho. \quad (2.1)$$

It states that the temporal change in hydraulic head h [m] (left hand side) equals the negative divergence of the fluid velocity (\mathbf{v} [ms^{-1}]) plus the sink/source terms (ϱ [s^{-1}]). The hydraulic variable representing the mediums ability to hold or release water is the water storativity/capacity C [m^{-1}].

Darcy's Law As Eq. (2.1) has both head and flux as unknowns, Darcy's Law relates the fluids velocity to the hydraulic heads. It describes the water flow as a relationship between the Darcy velocity of the fluid, the medium and fluid properties and the hydraulic gradient:

$$\mathbf{v}(\mathbf{x}, t) = -K \nabla h(\mathbf{x}, t), \quad (2.2)$$

where $h(\mathbf{x}, t)$ is the hydraulic head at position \mathbf{x} , K [ms^{-1}] the hydraulic conductivity of the medium, $\mathbf{v}(\mathbf{x}, t)$ [ms^{-1}] the Darcy velocity and \mathbf{x} the position vector (in a cartesian coordinate system):

$$\mathbf{x} = \begin{pmatrix} x \\ y \\ z \end{pmatrix}. \quad (2.3)$$

The hydraulic head of a fluid is composed of pressure and elevation head. The pressure head represents the internal energy of water due to the pressure exerted on its boundaries (usually defined with reference to atmospheric pressure) where elevation head is the relative potential energy of water raised above a particular reference point (usually defined with reference to sea level). Further, the hydraulic conductivity K relates the driving force (gradient in hydraulic head) with the movement of water within the media. Hence it quantifies the materials ability to conduct water flowing along the porous media.

In general the ∇ -operator is the mathematical operator gradient, divergence or rotation. For the head field, the ∇ -operator is used as a spatial differentiator (gradient of a scalar field) in the way of

$$\nabla h(\mathbf{x}) = \begin{pmatrix} \frac{\partial h}{\partial x} \\ \frac{\partial h}{\partial y} \\ \frac{\partial h}{\partial z} \end{pmatrix}. \quad (2.4)$$

The Darcy equation can be transformed without loss of generality to

$$\mathbf{v} = \begin{pmatrix} v_x \\ v_y \\ v_z \end{pmatrix} = - \begin{pmatrix} K_{xx} & 0 & 0 \\ 0 & K_{yy} & 0 \\ 0 & 0 & K_{zz} \end{pmatrix} \begin{pmatrix} \frac{\partial h}{\partial x} \\ \frac{\partial h}{\partial y} \\ \frac{\partial h}{\partial z} \end{pmatrix}, \quad (2.5)$$

hence the conductivity coefficients show up in a diagonal matrix.

The main assumption of Darcy's Law is a laminar flow (in contrast to turbulent flow) and a sufficient size of the pore volume (the REV). This assumption is fulfilled as long as the water flow velocities in the subsurface are small enough.

2.2 Subsurface

From a microscopic view the overall subsurface can be regarded as a porous media. However, we divide it into two main categories: the so-called unsaturated (or aerated) zone and the saturated zone as illustrated in Figure 2.2. In the zone of saturation all pores are completely water filled whereas in the unsaturated zone pores contain both gases (mainly air) and water. The upper part of subsurface is usually formed by the soil water zone. Its thickness varies greatly, from almost zero meters in swamps to hundreds of meters in arid regions. This zone is typically followed by the intermediate vadoze zone and the capillary zone. The unsaturated zone extends from the ground surface down to water table where the saturated zone starts with the topmost aquifer, the so-called phreatic aquifer. The lower boundary of the saturated zone is usually formed by an impervious bedrock.

Soils (and soil water) Soils are the skin of the solid earth. They can be categorized into three basic different soil types: a clayey soil, a loamy soil and a sandy soil. Most soils are a combination of the three. Hence,

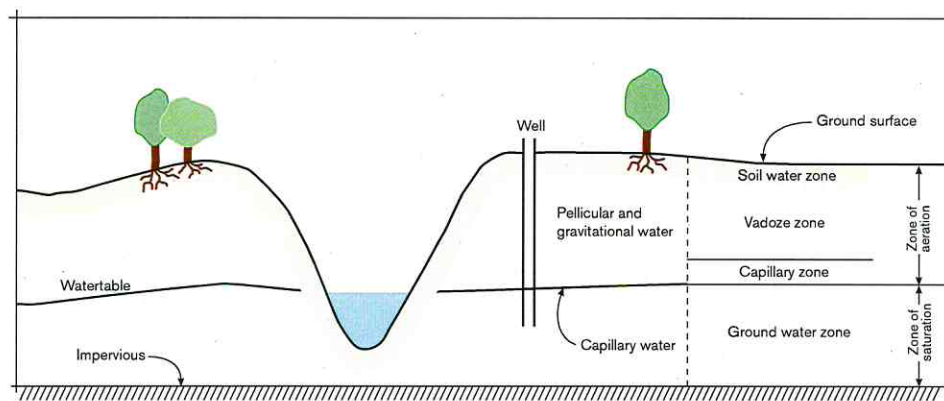


Figure 2.2: Distribution of subsurface water after Bear (1988). The zone of aeration in this notation will be renamed as the unsaturated zone in our notation and refers to soils and soil water flow. The zone of saturation corresponds to the saturated zone (aquifer) and the flow of groundwater.

the soil texture depends upon the amount of each soil type in a particular given soil sample.

Water flow in soils, the so-called unsaturated/vadoze zone, is characteristically different from flow in aquifers in that (i) the hydraulic properties are not only a function of space but also of soil water content, (ii) the flow encompasses variable fractions of the pore space, and (iii) it is strongly coupled with the atmosphere through rainfall and evapotranspiration which leads to stochastically induced fluctuations in the water content.

Aquifers (and groundwater) Formations carrying groundwater are separated into aquifers and aquicludes. The aquifer is an underground

layer of water-bearing permeable materials (consolidated like rock or unconsolidated like gravel, sand, silt or clay) and can be regarded as a hydraulic conductor of high permeability. On the other hand, aquicludes are hydraulically isolated formations of low permeability. In general, groundwater encompasses the part of the subsurface water that fills the pore space entirely.

Groundwater layers can be categorized into the class of unconfined and confined aquifers. For an unconfined aquifer the groundwater table is free to move. In contrast, a confined aquifer is bounded by two aquicludes. The thickness thus does not change and it has no free water table. Thus, for the confined case the water head is higher than the upper bounding aquiclude.

2.3 Groundwater flow

The head field $h(x, t)$ describing the groundwater flow is determined by combining the diffusion equation (2.1) and Darcy's Law (2.2)

$$C \frac{\partial h(\mathbf{x}, t)}{\partial t} - \nabla (K \nabla h(\mathbf{x}, t)) = \varrho(\mathbf{x}, t). \quad (2.6)$$

If the capacity term C and the conductivity term K are constant over the entire domain, analytical solutions can be derived by simplifying Eq. (2.6) as follows.

2.3.1 Well flows: radial groundwater flow

In order to describe well flows mathematical, the well extracting water from the aquifer is placed to the origin of the coordinate system. Under homogeneous subsurface conditions (hydraulic properties of the aquifer do not change over space), the arising flow configuration does not depend on the angle in horizontal direction. This setup is called a radially symmetric flow field. If the pumping well is fully penetrating and the well is completed across the entire thickness of the aquifer, the water flow does not depend on the vertical coordinates neither, hence the problem becomes one dimensional:

$$C \frac{\partial h}{\partial t} = \frac{1}{r} K \frac{\partial h}{\partial r} + K \frac{\partial^2 h}{\partial r^2}, \quad (2.7)$$

To solve this equation some supplementary conditions are required. The first boundary condition (BC I) states that at the well radius r_w with z_a being the aquifer thickness along the vertical axis, the pumping well is extracting water by the flow rate Q_w [$m^3 s^{-1}$]. (BC II) states that the hydraulic head is known at a certain reference point (for example a constant background head h_0 at the outer boundary $r = r_d$ of the flow domain).

$$\begin{aligned} \text{(BC I)} \quad & 2\pi r z_a K \frac{\partial h(r)}{\partial r} \Big|_{t, r=r_w} = Q_w, \\ \text{(BC II)} \quad & h(t, r = r_d) = h_0(t), \end{aligned}$$

and

$$(IC) \quad h(t = 0, r) = h_{init}(r).$$

Based on the aquifers supposed homogeneity and the boundary and initial conditions (IC) the below analytical solutions can be derived for steady and transient state.

Steady state Setting the time derivative of Eq. (2.7) to zero gives the ordinary differential equation (ODE)

$$\frac{1}{r}K \frac{\partial h}{\partial r} + K \frac{\partial^2 h}{\partial r^2} = 0, \quad (2.8)$$

with the analytical Thiem solution

$$h(r) = \tau_2 \ln(r) + \tau_1, \quad (2.9)$$

where τ_1 and τ_2 are integration constants set by the boundary conditions (the need for the initial condition vanishes under steady state).

Under steady state, the first boundary condition is adapted such that the radial flow rate across the cylindric surface $A_s [m^2]$ at any radius r multiplied by the Darcian flow velocity in radial direction v_r equals the pumping

rate Q_w at r_w resulting in

$$Q_w = A_s \times v_r = 2\pi r z_a \times K \frac{\partial h}{\partial r}. \quad (2.10)$$

Comparing Eq. (2.10) released to $\partial h / \partial r$ with the first derivative of Eq. (2.9), we find

$$\tau_2 = \frac{Q_w}{2\pi z_a K}. \quad (2.11)$$

Now, inserting τ_2 and the second boundary condition, namely that $h(r = r_d) = h_0$ is known, into Eq. (2.9) gives the other constant

$$\tau_1 = h_0 - \frac{Q_w}{2\pi z_a K} \ln(r_d). \quad (2.12)$$

Transient state In transient state, the radial groundwater flow equation for homogeneous K and C reads

$$\frac{1}{r} \frac{\partial h}{\partial r} + \frac{\partial^2 h}{\partial r^2} = \frac{1}{a} \frac{\partial h}{\partial t}, \quad (2.13)$$

with $a = \frac{K}{C} = \text{const.}$ Extracting water at a rate of $Q_w [m^3 s^{-1}]$ from a sink in the center of the aquifer with thickness z_a leads to the analytical solution

$$h(r, t) = \frac{Q_w}{4\pi z_a K} \Gamma(u), \quad (2.14)$$

where $\Gamma(u)$ is the Theis or well function of u given by

$$\Gamma(u) = \int_u^\infty \frac{\exp(-u)}{u} du, \quad (2.15)$$

with $u = (r^2 C)/(4tK)$. The imposed boundary and initial conditions for the Theis solution are

$$\text{(BC I)} \quad 2\pi r z_a K \left. \frac{\partial h}{\partial r} \right|_{t, r=r_w} = Q_w(t),$$

$$\text{(BC II)} \quad h(t, r \rightarrow \infty) = 0,$$

and

$$\text{(IC)} \quad h(t = 0, r) = 0.$$

2.3.2 Natural heterogeneity of hydraulic properties

All derivations and solutions shown in the previous section are based on the assumption that the hydraulic properties of the aquifer (like capacity or conductivity) do not change over space. However, aquifers typically exhibit spatial heterogeneities at multiple scales. This is illustrated in Figure 2.3 showing the varying structure of sediments at several levels.

To express the spatial behavior of these properties, the following terms are established:

- Homogeneity - the property under study is position independent.
- Heterogeneity - the property under study is position dependent.

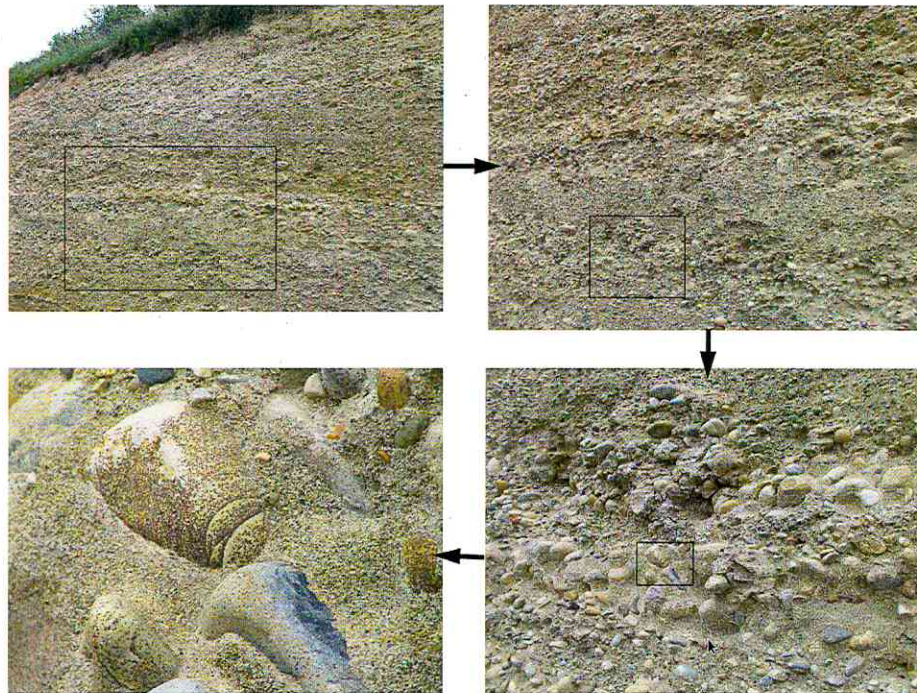


Figure 2.3: Natural heterogeneity of hydraulic properties at several scales. Arrows indicate path of increasing magnification and rectangles mark the clipping for the next step. Taken from Roth (2007) by courtesy of the author.

- Isotropy - the property under study is direction independent.
- Anisotropy - the property under study is direction dependent.

In terms of conductivity for example, the porous medium is homogeneous and isotropic if K is constant or heterogeneous and isotropic if $K(x, y, z)$ is a function of space. Otherwise the medium is anisotropic if K is a symmetric tensor of second degree (a matrix that is invariant against coordinate transformation).

From the analyses of a large number of field data in different geological formations, Freeze (1975) and Hoeksma and Kitanidis (1985) concluded that hydraulic conductivity can be considered to be log-normally distributed as one among other possibilities. Under such conditions, the hydraulic conductivity field $K(\mathbf{x})$ is given by

$$K(\mathbf{x}) = K_0 \exp(f(\mathbf{x})), \quad (2.16)$$

where K_0 is a conductivity of unit one that gives $K(\mathbf{x})$ the correct dimension.

By definition, $f(\mathbf{x})$ follows a normal distribution. The density function of a normal distribution is fully characterized by its mean and covariance function. Values close to the mean tend to build field-spanning structures where extreme values are less connected. Moreover, we assume $f(\mathbf{x})$ to follow a statistically homogeneous distribution. Hence the statistical

moments become translation invariant in space. The space invariance of $\overline{f(\mathbf{x})} = \bar{f} = \text{const.}$ allows to split $f(\mathbf{x})$ into its mean and the standard deviation

$$f(\mathbf{x}) = \bar{f} + \tilde{f}(\mathbf{x}), \quad (2.17)$$

where the bar denotes an ensemble average over $f(\mathbf{x})$.

The correlation (also named the covariance) function is in general defined as

$$w_f(f(\mathbf{x}), f(\mathbf{x}')) = \overline{(f(\mathbf{x}) - \bar{f}(\mathbf{x})) (f(\mathbf{x}') - \bar{f}(\mathbf{x}'))}. \quad (2.18)$$

For a statistically homogeneous field $f(\mathbf{x})$, it can be rewritten by making use of the splitting for $f(x)$ as

$$w_f(\mathbf{x} - \mathbf{x}') = \overline{\tilde{f}(\mathbf{x}) \tilde{f}(\mathbf{x}')}, \quad (2.19)$$

where w_f only depends on the distance $(\mathbf{x} - \mathbf{x}')$.

Under this condition, the second central moment variance σ_f^2 , indicating the strength of fluctuations, is space invariant and follows as

$$\sigma_f^2 = \overline{(f(\mathbf{x}) - \bar{f})^2} = \overline{\tilde{f}(\mathbf{x})^2} = w_f(\mathbf{x} = \mathbf{x}'). \quad (2.20)$$

For mathematical reasons, we choose a Gaussian shaped correlation function

$$w_f(\mathbf{x} - \mathbf{x}') = \sigma_f^2 \exp \left[- \sum_{i=1}^N \frac{(x_i - x'_i)^2}{\xi_i^2} \right], \quad (2.21)$$

where ξ_i is the correlation length of $f = \log K_f$ in the i -th direction of the domain (where N is the dimension of the aquifer).

2.3.3 Separation of scales

Well flows are prescribed by the application of either a certain hydraulic head or a fixed flow rate at the water extracting sink. No matter, which of them is prescribed, the discharge relates to the gradient of hydraulic head within the flow field. Restating Eq. (2.10), it is the hydraulic conductivity that relates this two entities. On larger scales, where the radial extent of pumping is much higher than the vertical thickness of the aquifer, the flow field becomes essentially horizontal. Then, hydraulic conductivity is often replaced by a variable called transmissivity T [$m^2 s^{-1}$]. It indicates the ability of the medium to transmit water through its entire thickness and is given by

$$T = \int_{z_a}^0 K(z) dz. \quad (2.22)$$

For constant K over z , the expression for T simplifies to the hydraulic conductivity K times the aquifers thickness z_a that is constant for a confined aquifer.

Both hydraulic properties, K and T , can be estimated using pumping tests. The setup for such well flows is shown in Figure 2.5. Since the water extraction by the well affects the hydraulic heads in the flow field, the

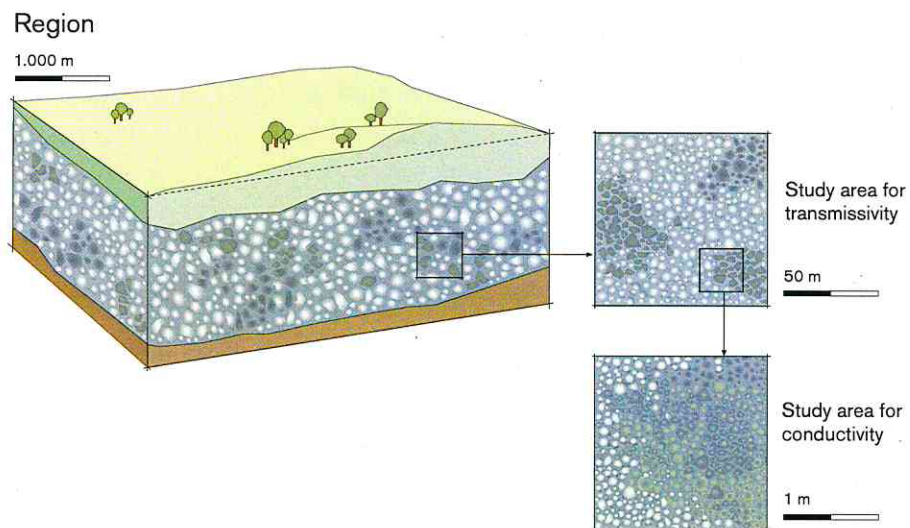


Figure 2.4: Hierarchy of hydraulic properties at multiple scales. Note that at every scale new heterogeneities occur.

drawdown that is the cone of depression in an area around the well is measured at several observation wells. The interpretation of these pumping tests is done however under the assumption that the aquifer under study is homogeneous. The state-of-the-art interpretation by the Theis or Thiem solution (Eq. (2.14) for transient or Eq. (2.9) for steady state) is precisely restricted to spatially uniform media.

For natural, heterogeneous aquifers the relationship between the discharge and drawdown is not as simple as the Thiem or Theis solution suggests for homogeneous aquifers. Using a single bulk property that relates extraction rate and hydraulic heads at various distances from the well will therefore

Scales	small $10^{-1} - 10^0 m$	intermediate $10^1 m$	large $10^2 m$	regional $> 10^3 m$
	heterogeneous	homogeneous	heterogeneous	homogeneous
parameter	$K(\mathbf{x})$	K_{eq}	$T(\mathbf{x})$	T_{eq}

Table 2.1: Hierarchy of different scales

fail. Especially steep gradients occurring in the vicinity of the well emphasize the importance to consider the local heterogeneity of the hydraulic properties at the process scale.

For heterogeneous media, a great deal of work has already been devoted to identify representative hydraulic conductivities or transmissivities for well flows (read the review of Sánchez-Vila et al. (2006)). In the beginning of Chapter 3 we will stress the differences between current approaches of introducing heterogeneity into radial groundwater flow and our approach presented in Chapter 3 as well.

In fact, the hydraulic properties are not only heterogeneous, they also vary on several length scales in space and hence, form the heterogeneous character of the aquifer at multiple scales. The hierarchy of different scales we assume in the present study is given in Table 2.1 and shown in Figure 2.4.

We adopt the view proposed by Dagan and Lessoff (2007) and distinguish between small scale and large scale well flows. Small scale well flows explore small scale heterogeneities in the order of decimeters to meters. Their drawdown exhibits only a few meters. Hence, the heterogeneity covered by

these small scale tests is in the range of the varying hydraulic conductivity field.

As explained in Section 2.3.2 and illustrated in Figure 2.4, in addition to those small scale heterogeneities, larger scale heterogeneities may appear on scales up to 100 meters or higher. Pumping the aquifer to such an extent, hydraulic heads and flow rates will be governed by the heterogeneous hydraulic transmissivity field.

In this scope, we will try to answer the following two main questions:

1. How does the heterogeneous hydraulic transmissivity field interfere with the large scale well flow? (Chapter 3)
2. How is the small scale well flow affected by the heterogeneity of the hydraulic conductivity field? (Chapter 4)

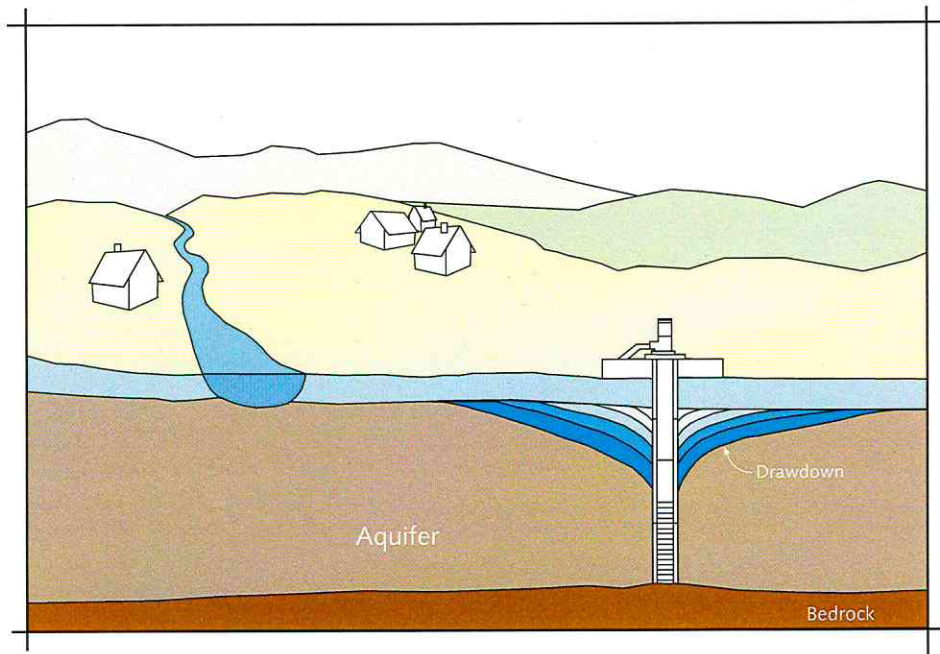


Figure 2.5: The setup of well flows.

Bibliography

- Bear, Jacob (1988). *Dynamics of Fluids in Porous Media*. New York: Dover Publications, Inc.
- Bear, Jacob and Yehuda Bachmat (1990). *Introduction to Modeling of Transport Phenomena in Porous Media*. Dordrecht: Kluwer Academic Publishers.
- Dagan, G. and S. C. Lessoff (2007). “Transmissivity upscaling in numerical aquifer models of steady well flow: Unconditional statistics”. In: *Water Resour. Res.* 43, W05431. DOI: 10.1029/2006WR005235.
- Freeze, R. A. (1975). “A Stochastic-Conceptual Analysis of One-Dimensional Groundwater Flow in Nonuniform Homogeneous Media”. In: *Water Res. Res.* 11.5, pp. 725–741.
- Hoeksma, R. and P. Kitanidis (1985). “Analysis of the spatial structure of properties of selected aquifers”. In: *Water Resour. Res.* 21, pp. 563–572.
- Maidment, David R., ed. (1993). *Handbook of Hydrology*. McGraw-Hill.

- Roth, K. (2007). *Soil Physics. Lecture Notes*. Institute of Environmental Physics, University of Heidelberg. URL: www.iup.uni-heidelberg.de/institut/forschung/groups/ts/students/sp.
- Sánchez-Vila, X. et al. (2006). "Representative hydraulic conductivities in saturated groundwater flow". In: *Rev. Geophys.* 44, RG3002. DOI: 10.1029/2005RG000168.

Chapter 3

Large scale well flows in the saturated zone ¹

3.1 Introduction

Hydraulic properties of an aquifer determine its ability to transmit water and thus control the groundwater flow through the aquifer. A general method for identifying these hydraulic properties is to perform pumping tests where the cone of depression is measured as system response to groundwater extraction. Well known in hydrogeology is the relationship between the steady-state drawdown and the pumping rate in a homogeneous

¹This chapter is a modified version of the paper: Schneider, C. L., and S. Attinger (2008), Beyond Thiem: A new method for interpreting large scale pumping tests in heterogeneous aquifers, *Water Resour. Res.*, 44, W04427, doi:10.1029/2007WR005898.

aquifer given by Thiem's equation (3.1).

$$T = \frac{Q_w}{2\pi\Delta h} \ln \left(\frac{r}{r_w} \right) \quad (3.1)$$

In homogeneous aquifers, the radially convergent flow toward a well is two dimensional and, thus, by performing an average over the vertical coordinate a three dimensional aquifer might be modeled as two dimensional. Doing so, the hydraulic conductivity K is replaced by the transmissivity defined as thickness of the aquifer z_a times hydraulic conductivity K .

In this expression, Δh [m] is the hydraulic head gradient at radial distance r [m] from the pumping well, r_w is the well radius, Q_w [m^3s^{-1}] is the discharge rate of the pumping well (located at $r = 0$) and T [m^2s^{-1}] the transmissivity.

These conditions (steady-state flow to a fully penetrating well with no nearby boundaries) are never fulfilled in nature, but often they can be used as a valid approximation of the actual conditions. More restricting however is the assumption of an homogeneous aquifer since aquifers typically exhibit by spatial heterogeneities. As a consequence, Thiem's equation and thus formula (3.1) is not valid for such aquifer systems. During the last 30 years an enormous amount of work has been devoted to identify representative hydraulic conductivities or transmissivities (see review article of Sánchez-Vila et al. (2006)). Representative hydraulic conductivities/transmissivities relate averages of flux and head gradient for different flow systems. Here we

adopt the notation of Sánchez-Vila et al. (2006) and distinguish between effective and equivalent hydraulic conductivities/transmissivities. Effective quantities relate ensemble averaged fluxes and head gradients whereas equivalent quantities relate spatial averages of fluxes and head gradients. Under ergodic conditions, both types of averaging result in the same representative hydraulic property. For steady state uniform flow under ergodic conditions for example, the geometric mean has been identified as the correct representative value for two dimensional isotropic flow fields whereas for one dimensional cases the harmonic mean provides the appropriate value (Indelman et al., 1996). A review of different methods for the calculation of effective hydraulic properties can be found in Renard and Marsily (1997). Representative transmissivity values in heterogeneous aquifers are more difficult to estimate from pumping tests. Flow fields around wells have a nonlocal structure and it is not possible to capture all aspects of nonuniform flow in a single representative quantity. To this end, effective and equivalent quantities do not only differ by the way they are derived (ensemble averaging or spatial averaging) but also for what they are used for because they address different features of radially convergent flows as we will show in this study. An excellent review on existing literature is presented by Sánchez-Vila et al. (2006) as well as Dagan and Lessoff (2007). Several field investigations share that hydraulic properties typically vary over a range of different scales. We adopt the view proposed by Dagan and Lessoff (2007) and distinguish between small scale and large scale pump-

ing tests. Small scale pumping tests explore small scale heterogeneities in the order of decimeters to meters. In addition to these small scale heterogeneities, larger scale heterogeneities may appear on scales larger than 100 meters. Large scale pumping tests are governed by these heterogeneities. On small scales, the aquifer is characterized by three dimensionally spatially distributed hydraulic conductivity values (Dagan and Lessoff, 2007, their section 2.1.1). Equivalent descriptions of the aquifer response after short term pumping may be used to scale-up the aquifer response to intermediate scales. On these intermediate scales the aquifer can be considered as homogeneous. Firmani et al. (2006) performed numerical simulations and confirmed previous theoretical investigations of Fiori et al. (1998): the equivalent conductivity is close to the arithmetic mean near the well and gradually approaches the equivalent conductivity in mean uniform flow fields, $K_{\text{efu}} [m s^{-1}]$. In highly anisotropic aquifers, K_{efu} is reached after a few tens of horizontal integral scales. On large scales, the aquifer thickness can be considered as much smaller than the horizontal range of the influence of the pumping test and such large aquifers can be treated as effectively two dimensional systems. Dagan and Lessoff (2007) (in paragraph [30]) conclude that K_{efu} times the aquifer thickness determines the large scale transmissivity to be used in large scale flow simulations. On this large scale, transmissivity is a point value and due to large scale heterogeneities again heterogeneously distributed in space ((Indelman and Dagan, 2006). Large scale pumping tests in heterogeneous aquifers have been stud-

ied first by Indelman et al. (1996), Sánchez-Vila (1997) and Sánchez-Vila et al. (1999), more recently by Dagan and Lessoff (2007). The hierarchy of different scales we assume in the present study was already given in Table 2.1 within Chapter 2.

We focus our analysis on large scale pumping tests in heterogeneous aquifers with the aim to determine representative transmissivity values for such pumping tests. Different strategies exist to define representative transmissivities.

One strategy to account for heterogeneity in large scale radially convergent flows is to determine an equivalent transmissivity, T_{eq} . The underlying idea is to determine a single transmissivity value that replaces the heterogeneous distribution in a given area. For well flow, usually an area with radius r_e around the well is selected, boundary conditions are imposed and the discharge is measured. The equivalent transmissivity is then defined as the single value that should be assigned to the entire area to obtain the same total outflow as observed for the heterogeneous area (Sánchez-Vila et al., 2006) using Thiem's equation. The equivalent transmissivity depends on the radius r_e and reproduces the same outflow and the correct mean draw-down at the distance r_e from the well. In this sense, the equivalent transmissivity is a block-averaged, single valued, upscaled transmissivity, which might be used for simulating regional well flows on numerical grids with grid sizes of several thousand meters (Dagan and Lessoff, 2007, their paragraph [79-80]). The approach is completely analogous to the approach used

by Firmani et al. (2006) for upscaling small scale pumping tests. Equivalent transmissivities for well flows have been investigated in several articles (Gómez-Hernández and Gorelick, 1989; Desbarats, 1992; Sánchez-Vila et al., 1999; Desbarats, 1994; Beckie and Harvey, 2002; Gómez-Hernández and Gorelick, 1989; Dagan and Lessoff, 2007). An excellent overview of the results presented in these articles is given by Sánchez-Vila et al. (2006). Wu et al. (2005) and Meier et al. (1998) obtained equivalent transmissivities deduced from local drawdowns at different locations, which are close but not equal to the geometric mean. Their results are supported by theoretical investigations of Dagan and Lessoff (2007). In their *Figure 3*, the harmonic mean represents the equivalent transmissivity that yields the correct mean drawdown and discharge close to the well. Its value slowly increases with increasing distance from the well. On the other hand, the variance of the equivalent transmissivity - normalized to the variance of the heterogeneous transmissivity - depends on the distance from the well, too. It is equal to one at the well and decreases to 0.6 after ten correlation lengths. These results demonstrate the fact that well flows show nonergodic behavior for two dimensions as recently elaborated out by Sánchez-Vila and Tartakovsky (2007).

The equivalent transmissivity depends on the radius r_e and one might be tempted to assume that evaluating T_{eq} at different distances $r_e = r$ from the well, and using it in a single forward simulation yields the correct depression cone for all distances r (see Figure 3.6 to compare the difference

for the whole aquifer response when using effective and equivalent transmissivities). This assumption turns out to be incorrect and will be illustrated in this study by numerical simulations. To reproduce the entire aquifer response to the pumping test which is the complete depression cone in a single forward simulation, another strategy is more successful. This strategy is to determine effective transmissivities. As Shvidler (1962) and Matheron (1967) pointed out already in the sixties, nonuniform flows show a nonlocal structure that are not possible to be captured by a single transmissivity value. An effective transmissivity T_{eff} that captures the entire depression cone correctly has to depend on the distance from the pumping well, $T_{\text{eff}} = T_{\text{eff}}(r)$. Effective transmissivities have been presented in several articles in the past. For a comprehensive presentation and discussion of these article we refer again to the review article by Sánchez-Vila et al. (2006)). Sánchez-Vila (1997), Neuman et al. (2004) and Coptý and Findikakis (2004) found effective transmissivity values that equal the harmonic mean in the near field of the well and the geometric mean in the far field. In principle, this outcome is consistent with results for equivalent transmissivities. However, comparing the dependence of T_{eff} and T_{eq} on r , the distance from the well, T_{eff} increases very rapidly with r and approaches the geometric mean after a few correlation lengths. T_{eq} increases only very slowly and does not reach the geometric mean before 20 correlation lengths. We conclude that equivalent and effective transmissivities, T_{eff} and T_{eq} , are different and serve different purposes. Equivalent trans-

missivities are used for aquifer parameterizations in regional pumping tests and numerical simulations of such tests with numerical grid sizes of several kilometers. Dagan and Lessoff (2007)) proposed to use the geometric mean in all regional grid blocks. On the other hand, effective transmissivities may serve best to reproduce the complete and nonlocal aquifer response to pumping on intermediate scales (ranging from hundred to thousands of meters). In other words, equivalent transmissivities are best for upscaling large scale pumping tests on regional grids and modeling the regional system response. Effective parameterizations are best for simplified interpretations of large scale pumping tests and modeling the subscale system response.

Our work focuses on evaluating coarse grained transmissivities to capture the entire depression cone similarly to effective transmissivities but using a combination of spatial filtering and ensemble averaging. In this sense, our work is complementary to the work of Dagan and Lessoff (2007) but compares with other work devoted to determine effective transmissivities (Sánchez-Vila et al., 2006). Effective transmissivities depend on the radial distance from the well and we hypothesize that the transition from near field behavior to far field behavior depends on the correlation length. Consequently, we plan to exploit this dependence to reliably infer correlation lengths from large scale pumping test data. Several closed formulas for an effective transmissivity have been proposed making use of perturbation theory approximations (Indelman et al., 1996; Sánchez-Vila, 1997) and/or

heuristic assumptions (Desbarats, 1992). To the best of our knowledge all existing formulas contain multi-dimensional integral expressions or infinite series expansions that have to be evaluated numerically. To this end, they have to be considered as semi-analytical formulas which complicates the inversion on correlation lengths. Having an explicit formula at hand would simplify the inversion considerably.

In summary, we wish to complete previous studies. Important questions we address are: (a) Is it possible to mathematically derive an explicit and closed formula for a radial distance dependent transmissivity value that captures the shape of the drawdown of large scale well flow at all locations? (b) What are the consequences of ergodicity breakdown close to the well for a single pumping test? (c) Is it possible to obtain reliable estimates for statistical properties like variance, geometric mean and correlation length from a single large scale pumping test by inverse modeling? In case this is possible, how many observation points do we need to make a robust and reliable estimate of these statistical properties?

This chapter is organized as follows. We introduce the flow model for simulating the cone of depression and the geostatistical properties of the heterogeneous transmissivity field. Afterwards we derive a scale or resolution dependent radially convergent flow model by making use of a method called Coarse Graining. In doing so, we end up with an explicit expression of a scale or radial distance dependent transmissivity. This formula is adjusted to the boundary condition (by harmonic averaging for the Neumann

boundary) and is used in a first step to reproduce the cone of depression of ensemble averaged pumping tests. In a next step, we extend the formula in order to account for statistical breakdown close to the well for a single well flow realization. Finally, we evaluate this new effective well flow model to derive geometric mean, correlation length and alike variance from pumping tests by inverse modeling.

3.2 Model

We consider a steady state groundwater flow toward a well in a confined aquifer of uniform thickness z_a . The steady-state head equation then reads

$$-\nabla (T(\mathbf{x}) \nabla h(\mathbf{x})) = 0, \quad (3.2)$$

where $T(\mathbf{x})$ is the transmissivity field and $h(\mathbf{x})$ the hydraulic head field. The well is located at the origin of the two-dimensional cartesian coordinate system $\mathbf{x}(x_1, x_2)$, where r is the radial coordinate defined in the horizontal plane. As boundary condition one may use a constant head $h(r = r_w) = h_w$ or a constant pumping rate Q_w . We choose a fixed pumping rate as in Dagan and Lessoff (2007); Sánchez-Vila (1997). In the far field of the well, irregular boundary effects are excluded by assuming a circular outer constant head boundary, $h(r = r_d) = h_0$.

The transmissivity is assumed as log-normally distributed in space (Mathéron, 1967). In this model, values close to the mean tend to build field-spanning structures where extreme values are less connected. The transmissivity $T(\mathbf{x})$ is then given by

$$T(\mathbf{x}) = T_0 \exp \left(\tilde{f}(\mathbf{x}) \right), \quad (3.3)$$

where $\tilde{f}(\mathbf{x})$ is a spatial normally distributed function (with zero mean and correlation function (3.4)). T_g is the geometric mean of the transmissivity. For mathematical reasons, we choose a Gaussian shaped correlation function

$$w_f(\mathbf{x} - \mathbf{x}') = \sigma_f^2 \exp \left[- \sum_{i=1}^N \frac{(x_i - x'_i)^2}{\xi^2} \right], \quad (3.4)$$

where σ_f^2 is the variance and ξ is the isotropic correlation length of $\log T(\mathbf{x})$. The correlation length ξ is much smaller than the range r_d of the pumping test. For general clarification of following notations and quantities, we refer to the nomenclature of this chapter listed in Table 3.1.

3.3 The concept of equivalent and coarse grained conductivity

As already discussed in the introduction of this chapter, we would like to state the differences between the concept of equivalent conductivity most

T_g	...	geometric mean of T
T_h	...	harmonic mean of T
\bar{T}	...	ensemble average over T
$\langle T \rangle$...	spatial average over T
T_{eq}	...	equivalent transmissivity relating ensemble averages of fluxes and head gradients
T_{eff}	...	effective transmissivity relating spatial averages of fluxes and head gradients
$T^{\text{CG}}(\langle \mathbf{x} \rangle_r)$...	spatial filtered transmissivity for nonuniform flow (exact solution)
$T_{\text{harm}}^{\text{CG}}(r)$...	harmonically average of $T^{\text{CG}}(\langle \mathbf{x} \rangle_r)$
$T_{\text{real}}^{\text{CG}}(r)$...	adapted transmissivity representation of $T_{\text{harm}}^{\text{CG}}(r)$ for a single (real) pumping test

Table 3.1: **Nomenclature:** Definition of notations and quantities

of the present studies are based on, and the here implemented concept of coarse grained conductivity.

An equivalent hydraulic conductivity is a parameter that relates the hydraulic pressure gradient at two given points to the corresponding flow velocity within a given pressure and flow field assuming that this relationship can be applied at all intermediate points. This concept of equivalent hydraulic conductivity was originally defined by Matheron (1967). The underlying idea is to determine a single conductivity value that replaces the heterogeneous distribution in a given area (e.g. the area between pumping well P and observation well A or B as can be seen in Figure 3.1). The equivalent conductivity is then defined as the single value that should be assigned to the entire area obtaining the same total outflow and head difference as observed for the heterogeneous area (Sánchez-Vila et al., 2006). To put it in another way, equivalent hydraulic conductivity can also be regarded as the conductivity value that is weighted uniformly over the given area of the flow field. However, the equivalent conductivity again assumes to treat the aquifer as homogeneous.

The coarse grained hydraulic conductivity is not a single parameter that relates the hydraulic pressure gradient at two given points to the corresponding flow velocity. In contrast to equivalent hydraulic conductivities, it is a space coordinate dependent parameter field taking the overall flow characteristics into account. Hence, coarse grained conductivity does not relate only the pressure heads and the flow between two points, but also

the flow process in between. It can be regarded as a parameter field emphasizing the local effects of the representative conductivity value (as can be seen in Figure 3.1).

3.4 Coarse Graining radially convergent flow toward a well

Several recent articles present effective as well as equivalent transmissivities for large scale well flows. We already discussed existing results and differences between them in the introduction. We propose another approach that is a filtering procedure called Coarse Graining combined with ensemble averaging for determining effective transmissivities. The strategy is the following: Optimizing a numerical simulator, radially convergent flows are numerically best resolved and discretized by volume elements aligned to a radial coordinate system. In particular, volume elements close to the well should be chosen smaller than volume elements in the far field of the well since steeper head gradients close to the well require a higher resolution. The question rises what are the correct transmissivity values that should be assigned to the smaller and coarse volume elements. We propose to use a nonuniform spatial filter. We wish to remind the reader that many other spatial averaging methods like volume averaging or homogenization techniques require averaging volumes that are much larger than the typical length scale of the heterogeneities. This is not prerequisite for nonuniform

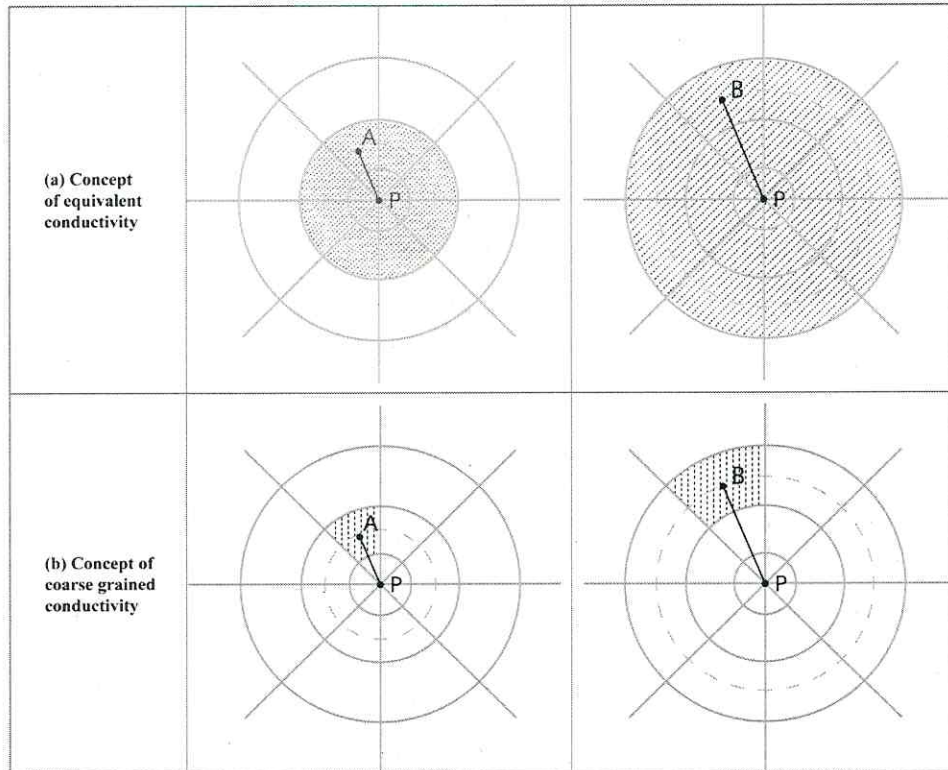


Figure 3.1: Comparison of (a) equivalent and (b) coarse grained conductivity for interpreting a radial flow problem where P refers to the well location and a respectively B refer to observation points in the flow field.

filter methods. Applying the nonuniform filter results in a filtered flow equation that shows almost none smoothing in the near field of the well and large smoothing in the far field. Consequently, the well flow equation is characterized by a nonlocal transmissivity field.

3.4.1 Uniform filtering

The filter method Coarse Graining was originally developed for Large Eddy Simulations (LES) in fluid mechanics and turbulence theories (McComb, 1990). In newer works of Rubin et al. (1999) and Attinger (2003) Coarse Graining was applied to uniform flow and transport in porous media.

Coarse Graining can be best explained as a spatial filter method that smooths or averages over volumes of variable size V . The smoothing volume V sets a filter length scale λ . The filtered head equation is defined on a coarser resolution: head fluctuations smaller than λ are smoothed out and their effect is covered by an effective transmissivity that is λ dependent. Head fluctuations larger than λ are still resolved by the filtered head equation. For comparison, in ensemble averaging all transmissivity fluctuations are averaged out and replaced by an asymptotic transmissivity tensor. If the averaging volume is very large compared to the correlation length ($\lambda \gg \xi$), ergodicity holds and filtering and ensemble averaging give the same results. For smaller averaging volumes $\lambda < \xi$ or $\lambda = \xi$, how-

ever, Coarse Graining and ensemble averaging yield different results due to ergodicity breakdown.

Coarse Graining offers two advantages. First, it is more flexible than ensemble averaging since λ is a free parameter, which accounts for preasymptotic effects. Secondly, it is free of any perturbation approximation. The filtered head equation is exact. Only if we need to compute effective transmissivities explicitly we calculate them in lowest order perturbation approximation and sum up higher order contributions by a renormalization scheme.

For spatial averaging, we use a Gaussian filter $u_\lambda(\mathbf{x})$ defined as a symmetric weight function

$$u_\lambda(\mathbf{x}) = \frac{1}{(2\pi\lambda^2/8)} \exp\left(-\frac{1}{2} \sum_{i=1}^2 \left(\frac{x_i}{\lambda/\sqrt{8}}\right)^2\right), \quad (3.5)$$

where x_i is the component of \mathbf{x} in direction i . The prefactor in front of the filter scale λ is a free parameter fixing the width of the Gaussian filter. In Attinger (2003) we determined its optimal value to $1/\sqrt{8}$. In literature, for large eddy simulations similar values have been identified to perform best (Layton, 2002).

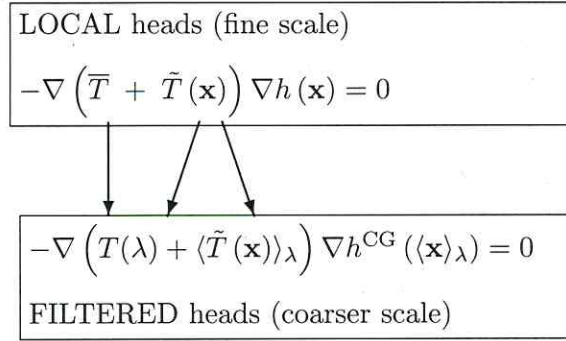
A filtered scalar field $f(\mathbf{x})$ is defined as

$$\langle f(\mathbf{x}) \rangle_\lambda \equiv \int_{-\infty}^{\infty} \int_{-\infty}^{\infty} f(\mathbf{x} - \mathbf{x}') u_\lambda(\mathbf{x}') dx'_1 dx'_2, \quad (3.6)$$

with

$$\mathbf{x}' = \begin{pmatrix} x'_1 \\ x'_2 \end{pmatrix}.$$

As $\lambda \rightarrow 0$, the points near \mathbf{x} tend to be more weighted, so $\langle f(\mathbf{x}) \rangle_\lambda \rightarrow f(\mathbf{x})$ as $\lambda \rightarrow 0$. In the following, we briefly recall the results of applying a uniform filter (Attinger, 2003): before applying Coarse Graining to the head equation, we split the transmissivity field $T(\mathbf{x})$ into its mean \bar{T} and the deviation $\tilde{T}(\mathbf{x})$. The resulting filtered head equation looks very similar to the original one with small but important changes. The filtered $T^{\text{CG}}(\langle \mathbf{x} \rangle_\lambda)$ depends on the filter volume λ . It is the sum of the new mean $T(\lambda)$ and a residual fluctuating part of the transmissivity given by $\langle \tilde{T}(\mathbf{x}) \rangle_\lambda$. Smoothing the local heads by coarse graining results in



By renormalization group analysis, Attinger (2003) found an explicit expression for $T(\lambda)$ for two dimensions

$$T(\lambda) = T_{\text{efu}} \exp \left(\frac{1}{2} \sigma_f^2 \frac{\xi^2}{\xi^2 + \lambda^2/4} \right). \quad (3.7)$$

A discussion about this scale dependent mean transmissivity $T(\lambda)$ incorporating subscale effects can be found in Attinger (2003).

The statistical properties of the smoothed transmissivity field $\langle \tilde{T}(\mathbf{x}) \rangle_\lambda$ are given by a vanishing mean, renormalized variance

$$\langle \sigma_f^2 \rangle_\lambda \equiv \sigma_f^2 \left(\frac{\xi^2}{\xi^2 + \lambda^2/4} \right), \quad (3.8)$$

and renormalized correlation length

$$\langle \xi \rangle_\lambda \equiv (\xi^2 + \lambda^2/4)^{1/2}. \quad (3.9)$$

If all transmissivity fluctuations are resolved explicitly and no Coarse Graining procedure has been applied, λ is zero and the variance reduces to the small scale variance as introduced in formula (3.4). On the other hand, if all transmissivity fluctuations are averaged out and replaced by an asymptotic transmissivity tensor, the ratio λ/ξ becomes very large and the variance very small. The variance approaches zero in the limit of $\lambda/\xi \rightarrow \infty$, which is equivalent to an asymptotic upscaling of the transmissivity. In contrast, the correlation length of the coarse grained logarithmic transmissivity fluctuations is increased compared with the small scale correlation length. By construction, the resolution scale of coarse grained processes is λ . Hence, all correlation lengths have to be at least of the order of magnitude of λ .

3.4.2 Nonuniform spatial filter for radially convergent flow toward a well

Optimal grid cells for solving well flows are volume segments aligned to radial coordinates. A volume segment is illustrated in Figure 3.2 and has the volume

$$\Delta V = \frac{\pi ((r + \Delta)^2 - (r - \Delta)^2)}{2\pi} \partial\Theta = 2(\partial\Theta)\Delta r. \quad (3.10)$$

Moreover, $\partial\Theta$ is the length of arc and Δ one half of the side length of the volume segment. Choosing almost quadratic volume elements, we set $\Delta = 1/2(\partial\Theta)r$, and finally end with a grid cell that has the volume of

$$\Delta V = (\partial\Theta)^2 r^2. \quad (3.11)$$

Close to the well, the grid cell is smaller and its volume increases with radial distance from the well. It implies an optimal filter volume that is proportional to r^2 .

Applying the nonuniform filter yields a non-uniformly filtered head equation with filtered transmissivities

$$T^{\text{CG}}(\langle \mathbf{x} \rangle_r) \equiv T_{\text{efu}} \exp \left(\frac{1}{2} \sigma_f^2 \frac{\xi^2}{\xi^2 + \zeta^2 r^2} \right) + \langle \tilde{T}(\mathbf{x}) \rangle_r, \quad (3.12)$$

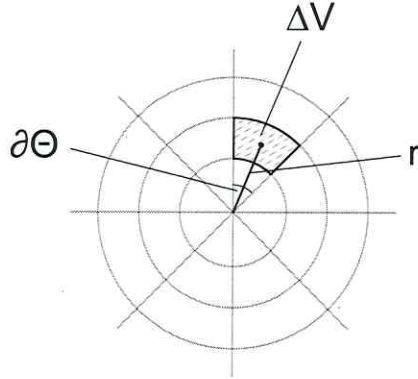


Figure 3.2: Radial volume filtering for radially convergent flow toward a well.

where T_{efu} is the upscaled effective transmissivity for uniform flow, which is the geometric mean T_g in two dimensions, and a free parameter ζ , fixed in the following, since so far we only set $\Delta V \propto r^2$. Equation (3.12) is the exact solution of filtering the pressure field for well flows. It still contains some heterogeneities namely all heterogeneities close to the well and smoothed heterogeneities in the far field.

3.4.3 Numerical simulations

We generated different realizations of heterogeneous, isotropic, two dimensional transmissivity fields making use of FGEN96 (for further reference see Robin et al. (1993)). The transmissivity values are defined on a uniform rectangular grid of 256x256 quadratic cells. The uniform grid spacing is $\Delta x = \Delta y = 0.2[L]$, hence the total spatial domain is 51.2x51.2[L]. Ensem-

Ens. Ind.	ξ in cells		\mathbf{T}_g [L^2/T]	σ_f^2	\mathbf{T}_h [L^2/T]
	x-dir.	y-dir.			
<i>A</i>	5.0	5.0	1×10^{-4}	1.0	0.61×10^{-4}
<i>B</i>	10.0	10.0	1×10^{-4}	1.0	0.61×10^{-4}
<i>C</i>	15.0	15.0	1×10^{-4}	1.0	0.61×10^{-4}
<i>D</i>	20.0	20.0	1×10^{-4}	1.0	0.61×10^{-4}
<i>E</i>	25.0	25.0	1×10^{-4}	1.0	0.61×10^{-4}
<i>F</i>	15.0	15.0	10×10^{-4}	1.0	6.07×10^{-4}
<i>G</i>	15.0	15.0	5.7×10^{-4}	1.0	3.45×10^{-4}
<i>H</i>	15.0	15.0	3.2×10^{-4}	1.0	1.94×10^{-4}
<i>I</i>	15.0	15.0	1.8×10^{-4}	1.0	1.09×10^{-4}
<i>J</i>	15.0	15.0	1×10^{-4}	1.0	0.61×10^{-4}
<i>K</i>	15.0	15.0	1×10^{-4}	0.100	0.95×10^{-4}
<i>L</i>	15.0	15.0	1×10^{-4}	0.325	0.85×10^{-4}
<i>M</i>	15.0	15.0	1×10^{-4}	0.550	0.76×10^{-4}
<i>N</i>	15.0	15.0	1×10^{-4}	0.775	0.68×10^{-4}
<i>O</i>	15.0	15.0	1×10^{-4}	1.0	0.61×10^{-4}
<i>P</i>	15.0	15.0	1×10^{-4}	2.0	0.37×10^{-4}

Table 3.2: Index table of log-normally distributed transmissivity fields; fields *C*, *J* and *O* are identical).

bles composed of n realizations each by the same statistical properties were created using the stochastic generator FGEN96 with different seeds. Moreover, a certain number of ensembles was generated with different statistical properties like variance, correlation length and geometric mean using identical seeds in between the ensembles to make the simulations of each realization comparable (see Table 3.2).

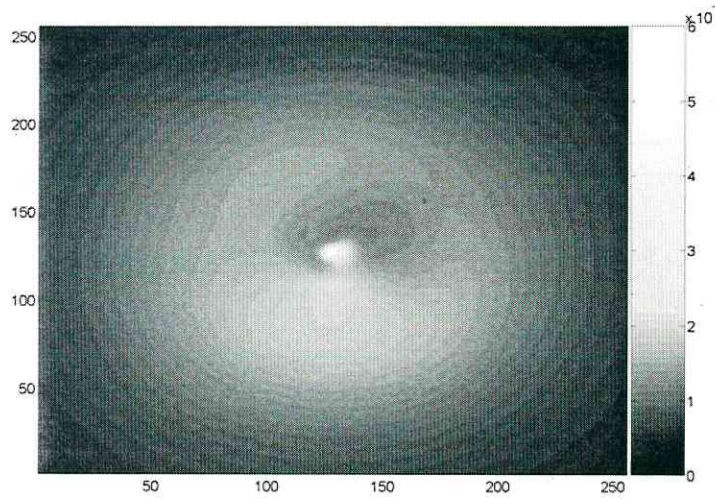


Figure 3.3: Coarse Grained transmissivity field by radial volume filter u_λ with $\lambda \propto r$.

The local drawdowns are numerically computed using the software MODFLOW (USGS, McDonald and Harbaugh (1988)) in the user shell PMWIN 5.1 (Chiang and Kinzelbach, 2001). The numerical solver uses a preconditioned Conjugate-Gradient package with a modified incomplete Cholesky preconditioner. For simulating the pumping tests, we choose the following parameters: The rectangular domain is bounded by a constant head boundary at an outer radius of $r_d = 128 \Delta x[L]$. The rectangular grid cell of the well is divided by 9 subgrids where the center subgrid cell is again divided in 5 subgrids resulting in a ratio of $r_w/\xi = 1/1500 \dots 1/8500$. This ratio is in the range suggested by Hoeksma and Kitanidis (1985), hence, the correlation length of the transmissivity compared to the well radius covers

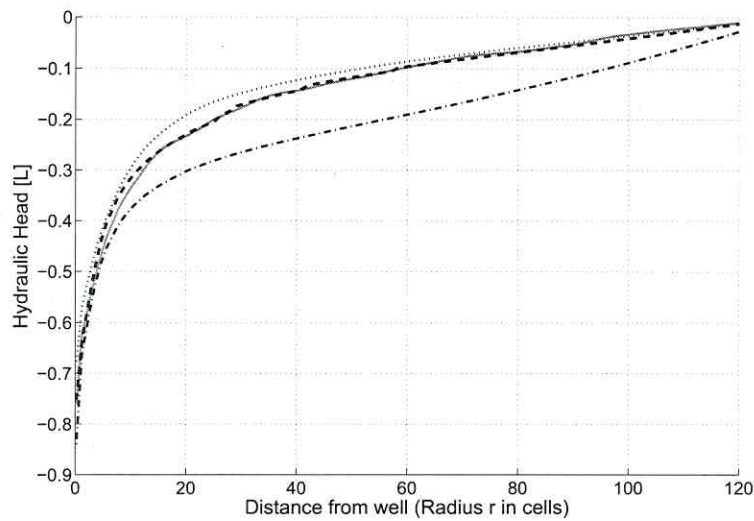


Figure 3.4: Drawdown of local T (solid line) and radial filtered transmissivity fields $\langle T \rangle_u^{CG}$ with $\varsigma = 2$ (dash-dotted line), $\varsigma = 1/2$ (dotted line) and $\varsigma = 1$ (dashed line) taken from ensemble A.

realistic values. All subgrid cells at the well are covered by a homogeneous transmissivity value called T_w . For the numeric simulations r_w is about $0.003\Delta x$. The latter is intrinsically set for simulating radially convergent flow toward a well in MODFLOW. At the pumping well, a pumping rate of $-10^{-4}[L^3/T]$ is fixed.

Forward simulations of pumping tests in aquifers parameterized by the non-uniformly filtered transmissivity field (3.12) are compared to forward simulations of pumping tests in aquifers parameterized by non-filtered transmissivities. Fixing ς to 1 yields excellent matches for all simulations. For illus-

tration of the filtering procedure, in Figure 3.3 we present a non-uniformly filtered transmissivity field by $\zeta = 1$. In Figure 3.4 drawdown the drawdown of this filtered field ($\zeta = 1$) is adjoined by the local drawdown and the drawdowns of the filtered transmissivity field by $\zeta = 2$ and $\zeta = 1/2$.

The non-uniformly filtered head flow equation is of limited hydrological applicability. We will simplify it more and define an effective transmissivity $T_{\text{harm}}^{\text{CG}}(r)$ by an ensemble average over the non-uniformly filtered well flow equation since for practical applications the spatial distribution of the filtered field $\langle \tilde{T}(\mathbf{x}) \rangle_r$ in (3.12) is not known in detail.

3.5 Interpreting an ensemble of pumping tests

The filtered transmissivity $T^{\text{CG}}(\langle \mathbf{x} \rangle_r)$ reproduces the depression cone exactly but it is difficult to make use of it in practical applications since usually the exact distribution of the heterogeneities is not known. To simplify $T^{\text{CG}}(\langle \mathbf{x} \rangle_r)$ we proceed as follows. Under the Neumann boundary condition, we propose the well is assumed to average harmonically over the transmissivity field $T^{\text{CG}}(\langle \mathbf{x} \rangle_r)$ in (3.12). The harmonic mean of the heterogeneous field $T^{\text{CG}}(\langle \mathbf{x} \rangle_r)$ given by a mean $T(r)$ and a fluctuating part $\langle \tilde{T}(\mathbf{x}) \rangle_r$ with variance $\sigma_f^2(r)$ can be easily calculated as

$$T_{\text{harm}}^{\text{CG}}(r) = T_g \exp \left(-\frac{1}{2} \frac{\sigma_f^2}{1 + r^2/l^2} \right). \quad (3.13)$$

Equation (3.13) for radially convergent flow states that the transmissivity is equal to the harmonic mean close to the well and equal to the geometric mean in the far field of the well. The transition between both zones is essentially determined by the correlation length. It occurs over large distances from the well as the correlation length ξ increases. The variance σ_f^2 influences the ensemble transmissivity close to the well ($T_h = T_g \exp(-\sigma_f^2/2)$) - a larger variance gives a lower transmissivity at the well and therefore a larger drawdown. The geometric mean is a multiplier in (3.13) and is influencing the harmonic mean (besides the variance) and solely the ensemble transmissivity in the far field. Recapitulating, the harmonically ensemble averaged, coarse grained transmissivity $T_{\text{harm}}^{\text{CG}}$ for radially convergent flow toward a well converges to T_h for $r = 0$ and T_g for $r \rightarrow \infty$. Our results give different ensemble transmissivity values depending on the radial distance r from the well and are in agreement with the work of Shvidler (1966), Dagan (1989), Neuman and Orr (1993), Indelman et al. (1996) and Sánchez-Vila et al. (1999).

To compare current approaches mentioned before, we like to point out the difference of equivalent and effective transmissivities. Figure 3.5 shows a plot, where transmissivities for all approaches, the one of Sánchez-Vila (1997), Desbarats (1992), Dagan and Lessoff (2007) and ours are illustrated. The effective/equivalent transmissivity at the well is the same in all approaches and equals the harmonic mean. Our approach gives similar results as the solution of Sánchez-Vila (1997) but they differ in the transition

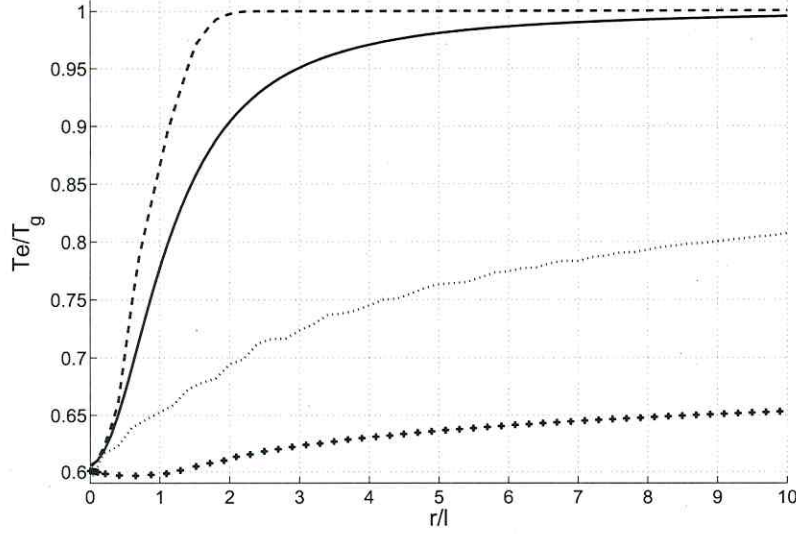


Figure 3.5: Effective, equivalent and coarse grained transmissivities as function of r/I (where $I = \xi$): our Eq. (3.13) ($T_{\text{harm}}^{\text{CG}}$) (solid line), *Figure 3* of Sánchez-Vila (1997) (dashed line), $\langle T_{eq} \rangle_h$ of Desbarats (1992) (dotted line) and Eq. (13) of Dagan and Lessoff (2007) (crosses).

regime from the harmonic to the geometric mean. The equivalent transmissivities of Desbarats (1992) and Dagan and Lessoff (2007) stay closer to the harmonic mean. This is due to the fact that the transmissivity at the well (which is the harmonic mean) is weighted stronger than it is the case for effective transmissivities.

Equivalent transmissivities are only assigned to relate the mean flux and mean head gradient between the well and distance r . Hence, a comparison

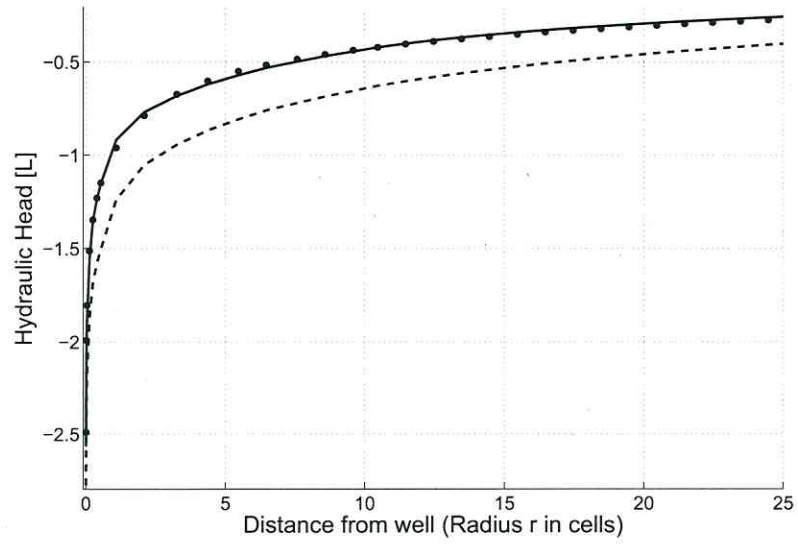


Figure 3.6: Drawdown of resulting transmissivities given by our Eq. 3.13 ($T_{\text{harm}}^{\text{CG}}(r)$) (solid line) and T_{eq} by Eq. (13) of Dagan and Lessoff (2007) (dashed line) compared to ensemble averaged ($n = 100$ realizations) heads \bar{h} (circles) of ensemble A.

of forward simulations of pumping an aquifer characterized by $T_{\text{eq}}(r)$ and $T_{\text{eff}}(r)$ as shown in Figure 3.6 demonstrates that the equivalent transmissivity is not capable to reproduce the complete drawdown.

Further, we test the validity of (3.13) for interpreting an ensemble of pumping tests and their resulting drawdowns \bar{h} by numerical simulations for different ensembles. Doing so, we compare the ensemble averaged drawdowns

with the drawdown of the coarse grained and harmonically averaged transmissivity $T_{\text{harm}}^{\text{CG}}$.

3.5.1 Results for coarse grained transmissivities

According to Eq. (3.13), $T_{\text{harm}}^{\text{CG}}$ and in turn the depression cone depend on the correlation length ξ , the variance σ_f^2 and the geometric mean T_g . To investigate this dependence, we generated ensembles of transmissivity fields which differ by the three parameters ξ , σ_f^2 and T_g as noted in Table 3.2, run the numerical pumping test on each of them and, at the end, performed the ensemble average over the resulting head fields of n realizations belonging to the same ensemble.

The ensemble results of varying ξ are displayed in Figure 3.7(a) and plotted versus the drawdown of the transmissivity given by (3.13). To compare the drawdowns in a homogeneous aquifer with a transmissivity equal to the geometric mean and the harmonic mean are respectively plotted as well. They form an upper and lower boundary for the ensemble drawdowns. Close to the well the ensemble drawdowns are near the drawdown resulting from the harmonic mean whereas in the far field of the well the ensemble drawdowns approach the drawdown resulting from the geometric mean. The transition between these two regimes depends on the correlation length. The larger the correlation length the larger the distance from the pumping

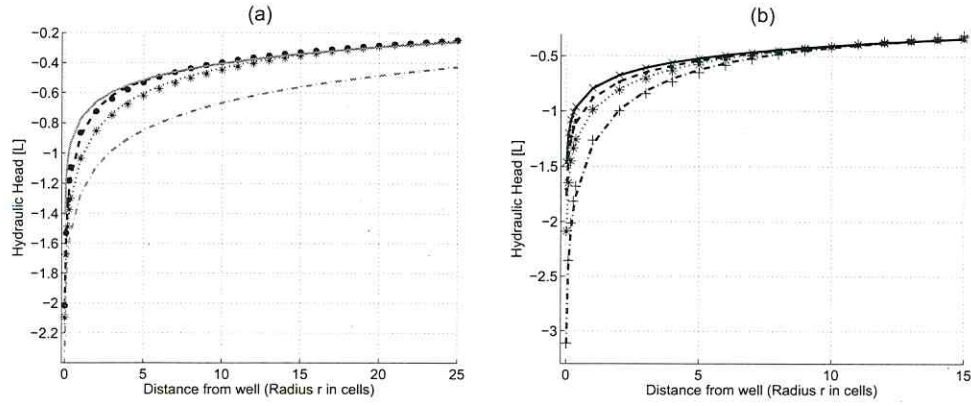


Figure 3.7: Ensemble of pumping tests and drawdown of transmissivities given by (3.13): **(a)** Impact of varying ξ for ensemble A ($n=150$) (dashed line) and E ($n=50$) (dotted line) compared to $T_{\text{harm}}^{\text{CG}}$ of A (dots) and E (asterisks), where the drawdown of T_g (graded solid line) and T_h (graded dash-dotted line) are the upper and lower boundary. **(b)** Impact of varying σ_f^2 for ensemble K ($n=50$) (solid line), M ($n=120$) (dashed line), O ($n=150$) (dotted line) and P ($n=300$) (dash-dotted line) compared to $T_{\text{harm}}^{\text{CG}}$ of K (crosses), M (dots), O (asterisks) and P (plus).

well when the ensemble drawdown matches the drawdown resulting from the geometric mean.

In Figure 3.7b the results of varying σ_f^2 are displayed. An impact of the variance is observed close to the well. The larger the variance, the larger is the ensemble drawdown at the well due to a lower effective transmissivity as expected by Eq. (3.13).

Figure 3.7 illustrates that the simulation of a pumping test in a medium with transmissivities given by (3.13) reproduces ensemble averaged draw-

downs. Only close to the well mismatches might occur if the number of realizations in the ensemble is too small. Whereas the geometric mean is affecting the overall drawdown of each realization, the impact of the correlation length on the drawdown decreases with increasing distance from the well.

In summary, the results of Coarse Graining and the nonuniform spatial filtering of radially convergent flow toward a well proved to be valid for interpreting an ensemble of pumping tests under the Neumann boundary condition. The drawdown of a coarse grained transmissivity given by (3.13) is able to capture the ensemble averaged drawdowns for all ensembles $A-O$, as it was shown only for ensembles A to E for varying ξ and K, M, O and P for varying σ_f^2 in Figure 3.8.

3.5.2 Convergence of ensemble averaging

As tested by numerical simulations, for a given n (size of the ensemble) the deviation of the ensemble averaged drawdown from the theoretical drawdown is larger with smaller correlation length or higher variance. For a correlation length of $\xi = 5$ grid cells the ensemble average over drawdowns in at least 150 aquifer realizations converges and yields the same drawdown as the simulation of the coarse grained aquifer given by (3.13). For $\xi = 10$ grid cells convergence is found already by 100 realizations, for $\xi = 15$ grid cells by 80 realizations and for $\xi = 25$ grid cells already by 50 realizations

while dealing with a variance of $\sigma_f^2 = 1$. Increasing variance σ_f^2 also effects the number of ensemble realizations needed when comparing ensemble averaged drawdowns to coarse grained results. For a variance of $\sigma_f^2 = 0.1$, 50 realizations yield the coarse grained drawdown where for $\sigma_f^2 = 2$ up to 300 realizations are necessary to cover the simulated drawdown of the transmissivity given by Eq. (3.13). This encourages us to increase the number of realizations for ensemble averaging when dealing with smaller correlation lengths or higher variances as done in Figure 3.7. These limitations have led to alternating realization numbers for the different ensembles presented in the previous section.

In their *figures 1 and 2*, Dagan and Lessoff (2007) have shown that single pumping tests have to be interpreted by the effect of heterogeneity manifested in the uncertainty of T_w . Due to the radial dependency of the filter volume size in our approach, ergodicity breaks down at the well and the results of ensemble theory are not comparable to the near field heads (determined by only small spatial averaging around the well) observed in single pumping tests. Therefore, we evaluate the deviation of the calculated transmissivity values by Thiem from the theoretical values to be expected. In principle, this can be done at every location r . Here, we restrict the analysis to $r = 0$ which is the borehole location since the variance will be largest there and thus can serve at worse case estimation. At the well we

define the error accordingly to

$$\mathcal{C}(n) = \frac{\sum_{i=1}^m \left(\frac{\overline{T_w(n)}_i - E(T)}{E(T)} \right)^2}{m}, \quad (3.14)$$

where $\overline{T_w(n)}_i$ is the transmissivity in the ensemble i of size n , where n is the number of realizations out of c (sample space) and m the number of averaging repetitions. $E(T)$ is the theoretically expected value of the effective transmissivity in the near field. It is given by T_h for the Neumann boundary condition. In equation (3.14), the ensemble transmissivity at the well, $\overline{T_w(n)}$, is calculated accordingly to

$$\overline{T_w(n)} = \frac{Q_w}{2\pi\Delta h(n)} \ln \left(\frac{r}{r_w} \right), \quad (3.15)$$

where the bar $-$ denotes for the ensemble average over n realizations in a given ensemble.

A varying correlation length shows no significant influence on the assumption of the coarse grained transmissivity in the vicinity of the well as shown only for case A and E in Figure 3.8(a). Thus, the coarse grained transmissivity at the well (defined in section 3.5 by the assumption of harmonical averaging) is independent on the correlation length. This result is important for interpreting single pumping tests. In contrast, the variance σ_f^2 shows an impact on estimating the transmissivity at the well: to ensure

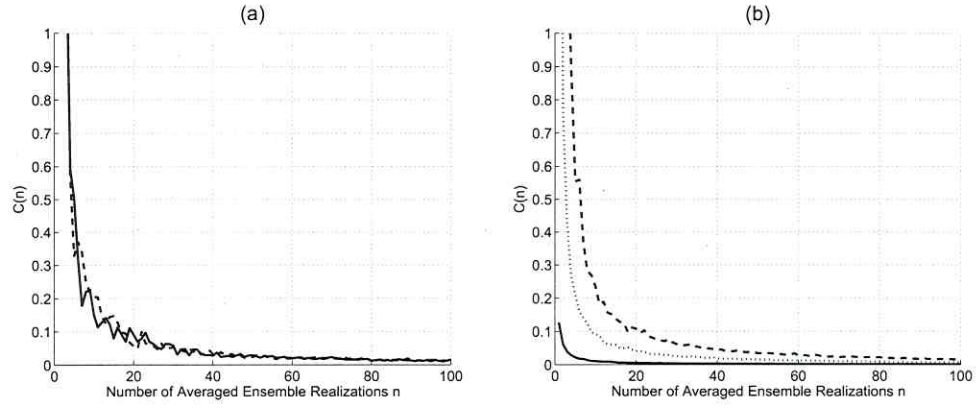


Figure 3.8: Convergence of ensemble averaged transmissivity in the pumping test near field $(\overline{T_w})_n$ to T_h (under Neumann boundary) for (a) varying ξ and (b) varying σ_f^2 ; $\mathcal{C}(n)$ given by (3.14); (a) solid and dashed lines correspond to ensemble A and E respectively; (b) solid, dotted and dashed lines correspond to ensemble K, M and O respectively.

the validity of the ergodicity hypothesis, a larger variance requires a higher realization number for ensemble averaging as shown in Figure 3.8(b).

3.6 Interpretation of single pumping tests

In single pumping tests, ergodicity breaks down close to the well and the local transmissivity value dominates the drawdown at and close to the well because the spatial filter volume at $r \ll \xi$ is small. The assumption of ergodicity might fail for well flows as has been pointed out by Sánchez-Vila and Tartakovsky (2007). We wish to illustrate this point by discussing again local and large scale pumping tests. Firmani et al. (2006) consid-

ered three dimensional short term pumping tests. In their approach, the assumption of ergodicity is crucial to make use of statistical averaging instead of spatial averaging. Doing so, the vertical depth of the aquifer has to comprise at least 50 correlation lengths in vertical direction to make sure that the ergodicity assumption is valid. The ensemble average which is mathematically better tractable equals a spatial average in z-direction. A spatial average over the vertical direction is physically reasonable since the hydraulic pressure differences in vertical direction almost instantaneously average out in the bore holes. Concerning a long time pumping test these hypotheses are rarely met. The aquifer is considered as effective two dimensional and thus the local transmissivity close to the well will influence the drawdown crucially and not a statistical average.

In our opinion this fact can be explained best by comparing local and large scale pumping tests. Local pumping tests are considered as the three dimensional aquifer response to short-term pumping. The vertical depth of the aquifer usually comprises many correlation lengths in vertical direction and hydraulic pressure variations in vertical direction almost instantaneously level or average out in the well. To this end, a spatial average over the vertical direction is also physically reasonable.

Equation (3.13) relies on ergodicity, hence, the spatial harmonic average equals the ensemble mean. An ensemble of drawdowns is simulated with isotropic transmissivity fields characterized by the correlation length $\xi = 15$ cells, $T_g = 10^{-4} L^2/T$ and variance $\sigma_f^2 = 1$ (index C). The influence of local

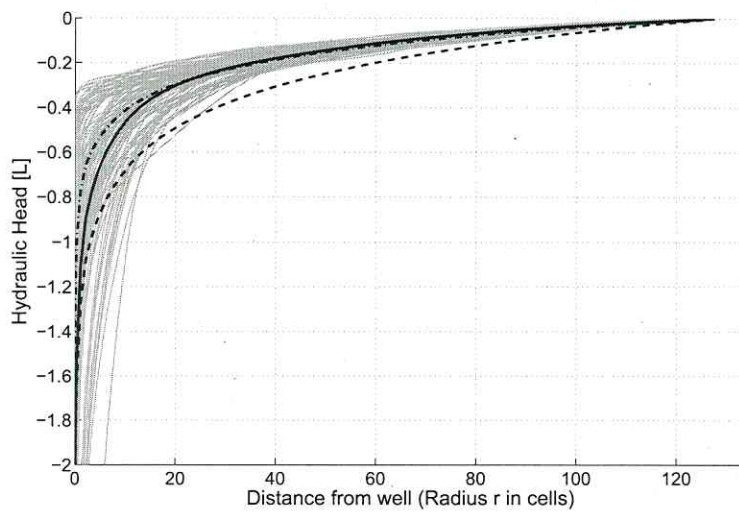


Figure 3.9: Ensemble averaged head field (solid line) over $n = 100$ realizations (graded solid lines) of Ensemble C; dash-dotted and dashed lines correspond to drawdowns of T_g and T_h respectively

transmissivity at the well to the drawdown development in steady state is illustrated in Figure 3.9 for $n = 100$ realizations.

The fact that the local transmissivity at the well determines the drawdown at the well in a single pumping test emphasizes the need for extending Eq. (3.13) when applying the proposed procedure to a single pumping test. The central question for interpreting a single pumping test in means of inferring statistical parameters of the transmissivity field is how an effective transmissivity field can reproduce the single drawdown of a heterogeneous field?

We propose a heuristic approach to account for ergodicity break down close to the well and justify it afterward by numerical simulations. The starting point is the observation that close to the well the drawdown is essentially determined by the local transmissivity T_w instead of the harmonic mean T_h (Neumann boundary). In the far field, the geometric mean determines the drawdown as expected,

$$\begin{aligned} (1) \quad T_{\text{real}}^{\text{CG}}(r=0) &= T_w, \\ (2) \quad T_{\text{real}}^{\text{CG}}(r \rightarrow \infty) &= T_g. \end{aligned} \tag{3.16}$$

Therefore, we propose to substitute the harmonic mean $T_h = T_g \exp(-1/2\sigma_f^2)$ in (3.13) as the effective ensemble transmissivity value at $r=0$ by the local transmissivity T_w . Hence, σ_f^2 in equation (3.13) has to be substituted by $\ln(T_g/T_w)^2$. The extended formula for the real transmissivity then reads

$$T_{\text{real}}^{\text{CG}}(r) = T_g \exp \left(-\frac{1}{2} \frac{\ln \left(\frac{T_g}{T_w} \right)^2}{1 + r^2/l^2} \right). \tag{3.17}$$

It implies that for a single drawdown it is not possible to identify the variance σ_f^2 while the correlation length ξ effects the drawdown in the transition phase and the geometric mean T_g in the far field. Moreover, the question arises how the local transmissivity value should be estimated since typically it is not known. We propose to assume the transmissivity as almost

homogeneous in a small area around the well supported by the results of Dagan and Lessoff (2007). Following this assumption, we can estimate the transmissivity by Thiem equation (3.1) using the heads measured at the well (r_w) and at a small distance to the well (\tilde{r})

$$T_w = \frac{Q_w}{2\pi\Delta h} \ln \left(\frac{\tilde{r}}{r_w} \right), \quad (3.18)$$

with $\Delta h = h(r_w) - h(\tilde{r})$ and \tilde{r}/r_w around 10 since for the numeric simulation in MODFLOW the resulting equivalent well radius $r_w = 0.003\Delta x$ and \tilde{r} is around $0.03\Delta x$ (two subgrid cells next to the well). We tested Eq. (3.17) in forward simulations for all ensembles and compared them to forward simulations in fully heterogeneous aquifers. We found a good agreement in all simulations. By chance, the well may be located in an area with a local transmissivity higher than the geometric mean. In this case, the drawdown is smaller than that resulting from a pumping test simulation in an aquifer with a transmissivity that equals the geometric mean. On the other hand, if the well is located in an area with a local transmissivity lower than the geometric mean, the drawdown lies under this curve. If, by chance, the local transmissivity lies close to the geometric mean ($T_w = T_g$), both curves - the local drawdown and the drawdown from the simulation in an aquifer with constant transmissivity that equals the geometric mean - coincide and it is impossible to infer the correlation length from the local drawdown of a steady state pumping test.

3.7 Inverse modeling

This section is concerned with the inverse estimation of the geometric mean T_g and correlation length ξ from the steady state drawdown of a pumping test. Under ergodic conditions also the variance σ_f may be estimated from an ensemble of long time pumping tests.

To achieve this goal, we perform a nonlinear regression to fit the simulated drawdown \hat{y} of the effective transmissivity field (3.17) to the local drawdown y (represented by reference points indicating measured heads) of a single realization. Besides, to estimate the variance under the Neumann boundary condition, we fit the drawdown of (3.13) to the ensemble averaged drawdown resulting from n simulated pumping tests (again represented by reference points).

The regression is based on the Gauss-Newton method, which solves nonlinear optimization problems through the least-squares method in nonlinear equilibrium problems. For the nonlinear problem the Newton method estimates a series of linear equilibrium problems that are then solved by the default Gauss method. The optimization function (for discrete measurement/observation points i)

$$\sum_{i=1}^k (\hat{y}_i - y_i)^2 \rightarrow \min! \quad (3.19)$$

will be minimized.

3.7.1 Estimating correlation length and geometric mean

In practice, the drawdown data are only available at few observation points. Hence, we do not use information of drawdowns in every detail as a test for inversion. The observables for the nonlinear regression of the parameters ξ (correlation length) and T_g (geometric mean) are selected reference points of single drawdowns simulated for transmissivity fields which had not been part of the forward modeling in the last section (new seeds). We select four reference points for the estimation where the first and second point are also necessary for the estimation of the local transmissivity T_w making use of equation (3.18), for example: (1) The drawdown value at the well. (2) The drawdown value 2 or 3 cells away from well (near field reference point). (3) The drawdown value between 5 and 25 cells away from the well (transition regime). (4) The drawdown in the far field (far field reference point).

The estimated regression parameters plotted in the histogram (Figure 3.10 and 3.11) rely on four selected reference points for $n = 900$ single realizations. The inversion is performed on ensembles A and E as well as for K , L , M and O (for parameter details see Table 3.2). The well may be located in an area of higher or lower transmissivity than the geometric mean which is expressed by the relation of T_w/T_g on the y-axis. As discussed in the previous section, the local transmissivity around the well T_w may be in the range of the geometric mean T_g coincidentally ($T_w/T_g \approx 1$).

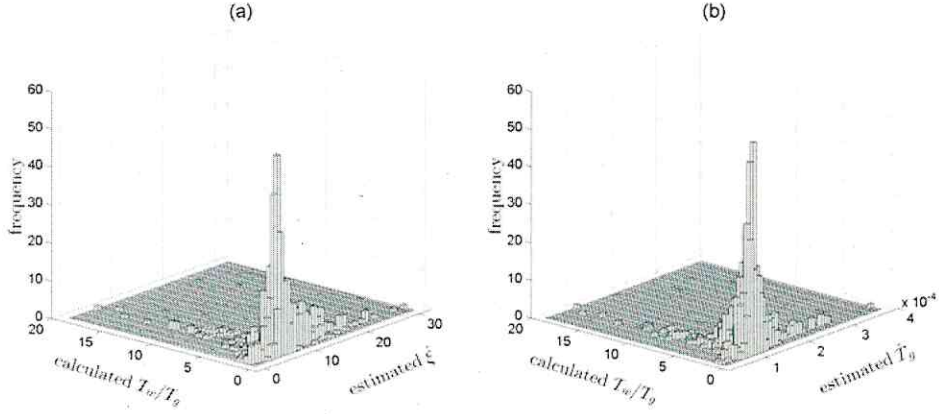


Figure 3.10: Regression results for $n=900$ single pumping tests of ensemble A ($\xi = 5$, $T_g = 10^{-4}$). (a) Histogram of estimated $\hat{\xi}$ vs. calculated T_w/T_g . (b) Histogram of estimated \hat{T}_g vs. calculated T_w/T_g .

Under this conditions, Eq. (3.17) reflects an almost homogeneous medium without the transition regime and the estimation of ξ gives higher confidence intervals results as can be seen in the histogram of Figures 3.10a and 3.11a.

These results show that the method is robust enough to identify the statistical parameters ξ and T_g of a transmissivity field by inverse modeling when the local transmissivity at the well is not in the range of the geometric mean. Beside this, using more reference points will increase the reliability of the nonlinear regression and hence limit the confidence interval.

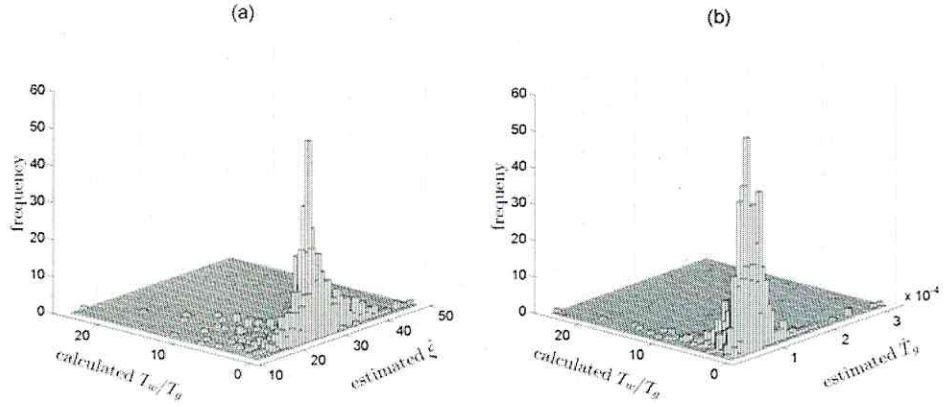


Figure 3.11: Regression results for $n=900$ single pumping tests of ensemble E ($\xi = 25$, $T_g = 10^{-4}$). (a) Histogram of estimated $\hat{\xi}$ vs. calculated T_w/T_g . (b) Histogram of estimated \hat{T}_g vs. calculated T_w/T_g .

3.7.2 Estimating the field Variance in ensemble averaged drawdowns

In a last step, we inversely estimate also the variance from an ensemble of pumping tests over $n = 50$ realizations. For the parameter estimation, we use a pumping test performed in an equivalent aquifer under Neumann boundary conditions. Based on (3.13), we estimate all three parameters, correlation length, variance and geometric mean from the ensemble averaged drawdown over n realizations through inverse modeling.

For the ensemble C with $\xi = 15$ cells, $T_g = 10^{-4} L^2/T$ and $\sigma_f^2 = 1$, the estimates differ for ξ by 12.2%, for T_g by 10.2% and for σ_f^2 by 12.9%. Ensemble A , characterized by a smaller correlation length $\xi = 5$ cells,

$T_g = 10^{-4} L^2/T$ and $\sigma_f^2 = 1$, yields also promising results: the estimation of ξ differs by 10.7%, of T_g by 8.3% and of σ_f^2 by 21.3% from the theoretical value. For an ensemble with higher correlation length, like E , with parameters $\xi = 25$ cells, $T_g = 10^{-4} L^2/T$ and $\sigma_f^2 = 1$, the estimates differ for ξ by 9.1%, for T_g by 3.1% and for σ_f^2 by 6.4%. These estimates are precise with a small confidence interval (high reliability) and a drawdown curve that fits the drawdown of the ensemble average quite well. Changing the variance, the inversion also works well for ensemble M , again with $n = 50$ realizations. The parameters of ensemble M are $\xi = 15$ cells, $T_g = 10^{-4} L^2/T$ and $\sigma_f^2 = 0.55$. Thus, the estimates differ for ξ by 8%, for T_g by 0.6% and for σ_f^2 by 4.4%.

3.8 Conclusion

By applying the filtering method Coarse Graining, we derived a closed formula for $T^{\text{CG}}(r)$, which describes an ensemble of pumping tests. The explicit result for $T_{\text{harm}}^{\text{CG}}(r)$ reads

$$T_{\text{harm}}^{\text{CG}}(r) = T_g \exp \left(-\frac{1}{2} \frac{\sigma_f^2}{1+r^2/l^2} \right).$$

For single pumping tests, ergodicity breaks down close to the well and the local transmissivity is dominating the drawdown at the well. Taking this ef-

fect into consideration, we derived a formula for $T_{\text{real}}^{\text{CG}}(r)$, which successfully reproduced the drawdowns in single pumping tests:

$$T_{\text{real}}^{\text{CG}}(r) = T_g \exp \left(-\frac{1}{2} \frac{\ln \left(\frac{T_g}{T_w} \right)^2}{1+r^2/l^2} \right).$$

We tested the theoretical results in numerical simulations and found the drawdowns in heterogeneous aquifers to be in good accordance with the corresponding values of the coarse grained aquifers. We showed in this chapter that $T_{\text{harm}}^{\text{CG}}(r)$ is appropriate to reproduce the depression cone of an ensemble of pumping tests but fails when being applied to evaluate single large scale pumping tests. Therefore, we adapted $T_{\text{harm}}^{\text{CG}}(r)$ to the conditions of a real single pumping test and called the modified transmissivity $T_{\text{real}}^{\text{CG}}$ (Eq. (3.16), section 3.5).

All results are beyond first order perturbation theory analysis and thus, through the performance of Renormalization Group analysis, valid for strongly heterogeneous media as well (Dean et al., 1996). This enabled us to develop a very efficient inverse method to reliably estimate statistical parameters like the variance or the correlation length of the transmissivity field from pumping tests. In particular, we demonstrated that only four observation points are necessary to reliably estimate the correlation length from a single pumping test. On the other hand, we demonstrated that the variance cannot be estimated from single pumping tests but only from an ensemble

of pumping tests. Nevertheless at least 50 pumping tests are necessary to obtain reliable estimates of the variance.

Bibliography

- Attinger, S. (2003). "Generalized Coarse Graining Procedures for Flow in Porous Media". In: *Comput. Geosci.* 7.4, pp. 253–273. DOI: 10.1023/B:COMG.00000005243.73381.e3.
- Beckie, R. and C. F. Harvey (2002). "What does a slug test measure: An investigation of instrument response and the effects of heterogeneity". In: *Water Resour. Res.* 38.12, 1290. DOI: 10.1029/2001WR001072.
- Chiang, W.-H. and W. Kinzelbach (2001). *3D-Groundwater Modeling with PMWIN. A Simulation System for Modeling Groundwater Flow and Pollution*. Berlin, Heidelberg, New York: Springer Verlag.
- Coppy, N. K. and A. N. Findikakis (2004). "Stochastic analysis of pumping test drawdown data in heterogeneous geologic formations". In: *J. Hydraul. Res.* 42, EXTRA ISSUE, pp. 59–67.
- Dagan, G. (1989). *Flow and Transport on Porous Formations*. New York: Springer Verlag.

- Dagan, G. and S. C. Lesoff (2007). "Transmissivity upscaling in numerical aquifer models of steady well flow: Unconditional statistics". In: *Water Resour. Res.* 43, W05431. DOI: 10.1029/2006WR005235.
- Dean, D.S. et al. (1996). "Renormalization of drift and diffusivity in random gradient flows". In: *J. Phys. A: Math. Gen.* 29.24, pp. 7867–7879. DOI: 10.1088/0305-4470/29/24/012.
- Desbarats, A.J. (1992). "Spatial Averaging of Transmissivity in Heterogeneous Fields With Flow Toward a Well". In: *Water Resour. Res.* 28.3.
- (1994). "Spatial Averaging of hydraulic conductivity under radial flow conditions". In: *Math. Geol.* 26.1, pp. 1–21.
- Fiori, A. et al. (1998). "Correlation structure of flow variables for steady flow toward a well with application to highly anisotropic heterogeneous formations". In: *Water Resour. Res.* 34, pp. 699–708.
- Firmani, G. et al. (2006). "Three-dimensional numerical analysis of steady state pumping tests in heterogeneous confined aquifers". In: *Water Resour. Res.* 42, W03422. DOI: 10.1029/2005WR004382.
- Gómez-Hernández, J. J. and S. M. Gorelick (1989). "Effective groundwater model parameter values: Influence of spatial variability of hydraulic conductivity, leakance and recharge". In: *Water Resour. Res.* 25.3, pp. 405–419.
- Hoeksma, R. and P. Kitanidis (1985). "Analysis of the spatial structure of properties of selected aquifers". In: *Water Resour. Res.* 21, pp. 563–572.

- Indelman, P. and G. Dagan (2006). "Modelling of regional-scale well-flow in heterogeneous aquifers: 2-D or not 2-D?" In: *Calibration and Reliability in Groundwater Modelling: From Uncertainty to Decision Making (Proc. of ModelCARE'2005)*, The Hague, The Netherlands: IAHS Publ. 304, pp. 215–219.
- Indelman, P. et al. (1996). "Steady flow toward wells in heterogeneous formations: Mean head and equivalent conductivity". In: *Water Resour. Res.* 32.7, pp. 1975–1984. DOI: 10.1029/96WR00990.
- Layton, William J. (2002). *A Mathematical Introduction to Large Eddy Simulation*. Research Note. Pittsburgh, PA 15260, U.S.A.: Department of Mathematics, University of Pittsburgh.
- Matheron, G. (1967). *Elements pour une theorie des milieux poreux*. Paris: Maisson et Cie.
- McComb, W. D. (1990). *Physics of Fluid Turbulence*. Oxford: Clarendon.
- McDonald, M. G. and A. W. Harbaugh (1988). "A modular three-dimensional finite-difference ground-water flow model". In: *U.S. Geol. Surv., Techniques of Water-Resources Investigations* 06-A1.
- Meier, P. M. et al. (1998). "An evaluation of Jacob's method for the interpretation of pumping tests in heterogeneous formations". In: *Water Resour. Res.* 34.5, pp. 1011–1025.
- Neuman, S. P. and S. Orr (1993). "Prediction of Steady state flow in Nonuniform Geologic Media by Conditional Moments: Extract Non-

- local Formalism, Effective Conductivities and Weak Approximation". In: *Water Resour. Res.* 29.2, pp. 341–364.
- Neuman, S. P. et al. (2004). "Type-curve estimation of statistical heterogeneity". In: *Water Resour. Res.* 40, W04201. DOI: 10.1029/2003WR002405.
- Renard, Ph. and G. de Marsily (1997). "Calculating equivalent permeability: a review". In: *Adv. Water Resour.* 20.5-6, pp. 253–278.
- Robin, M. J. L. et al. (1993). "Cross-Correlated Random Field Generation With the Direct Fourier Transform Method". In: *Water Resour. Res.* 29.7, pp. 2385–2397.
- Rubin, Y. et al. (1999). "The concept of block-effective macrodispersivity and a unified approach for grid-scale and plume-scale dependent transport". In: *J. Fluid Mech.* 395, pp. 161–180.
- Sánchez-Vila, X. (1997). "Radially convergent flow in heterogeneous porous media". In: *Water Resour. Res.* 33.7, pp. 1633–1641.
- Sánchez-Vila, X. and D. M. Tartakovsky (2007). "Ergodicity of pumping tests". In: *Water Resour. Res.* 43, W03414. DOI: 10.1029/2006WR005241.
- Sánchez-Vila, X. et al. (1999). "Upscaling transmissivity under radially convergent flow in heterogeneous media". In: *Water Resour. Res.* 35.3, pp. 613–621.

- (2006). “Representative hydraulic conductivities in saturated ground-water flow”. In: *Rev. Geophys.* 44, RG3002. DOI: 10 . 1029 / 2005RG000168.
- Shvidler, M. I. (1962). “Filtration flows in heterogeneous media”. In: *Akad. Nauk USSR Mekh. I Mas.* 3, pp. 185–190.
- (1966). “The source-type solution of the problem of unsteady flow in random porous media”. In: *Akad. Nauk USSR Mekh. Zhidk. Gaza* 4, pp. 137–141.
- Wu, C. M. et al. (2005). “Traditional analysis of aquifer tests: Comparing apples to oranges?” In: *Water Resour. Res.* 41, W09402. DOI: 10.1029/2004WR003717.

Chapter 4

Interpreting small scale pumping tests ²

4.1 Introduction

Small scale or short term pumping tests stimulate the aquifer response on small scales. Modeling this aquifer response, the aquifer is characterized by three dimensionally spatially distributed hydraulic conductivity values (Dagan and Lessoff, 2007, their section 2.1.1). An area with a radius r_e around the well is selected, a constant head condition is imposed and the total out-

²This chapter is a modified version of the technical note manuscript: Schneider, C. L., and S. Attinger. An alternative to equivalent parameters for interpreting small scale pumping tests in heterogeneous three dimensional aquifers. to be subm. to Water Resources Research.

flow is measured. Recently, several publications addressed the question if and how the aquifer response to pumping tests can be described by models with effective or equivalent parameters (Sánchez-Vila et al., 2006).

It is important to be aware that effective and equivalent descriptions may serve different purposes. Equivalent descriptions of the aquifer response after short term pumping may be used to scale-up the aquifer response to intermediate scales on which the aquifer can be considered as homogeneous. Consequently, the equivalent conductivity is defined as the single value that should be assigned to the whole area obtaining the same total outflow observed in the heterogeneous domain (Sánchez-Vila et al., 2006). The equivalent conductivity depends on the radius r_e and reproduces the same outflow and the correct mean drawdown at the distance r_e from the well. Equivalent conductivities have been evaluated by Firmani et al. (2006) and Indelman et al. (1996). We summarize the main aspects which are relevant for the work presented in this article. Firmani et al. (2006) carried out numerical simulations and confirmed the previous theoretical investigation of Fiori et al. (1998). The equivalent conductivity is close to the arithmetic respectively harmonic mean near the well and tends slowly to the equivalent conductivity of mean uniform flows, $K_{\text{efu}} [m s^{-1}]$. In strongly anisotropic aquifers, for example, K_{efu} is reached after a few tens of horizontal integral scales. By using the distance dependent behavior of the equivalent conductivity, Firmani et al. (2006) tried to inversely estimate the variance σ_f^2 , the horizontal integral scale I and the anisotropy ratio e as well as K_{efu} from

drawdown data. While σ_f^2 and K_{efu} were reproduced very well by their inference procedure, ξ and e were much more difficult to estimate.

We wish to complete previous studies for three dimensional short range pumping tests. In particular, we aim at the derivation of an explicit and closed formula for an pseudo-effective and radial distance dependent conductivity value that captures the shape of the drawdown of small scale pumping tests at all locations as we demonstrated already in the case of large scale pumping tests in the previous Chapter 3. With this alternative approach, we wish to study the possibility to infer reliable estimates for the horizontal correlation length ξ_h and the anisotropy ratio e from a single small scale pumping test by inversion.

This chapter is organized as follows. First, we specify a virtual pumping test for simulating the cone of depression in a virtual heterogeneous aquifer. Secondly, we derive a scale or resolution dependent pumping test model by making use of a method called Coarse Graining in the line of Schneider and Attinger (2008). In doing so, we end up with an explicit expression of an effective, scale or radial distance dependent conductivity. This formula is used in a first step to reproduce the cone of depression of a short range pumping test as simulated in Firmani et al. (2006). We evaluate this new effective virtual pumping test to infer geostatistical parameters and K_{efu} from short range pumping tests by inverse modeling.

4.2 Model

We consider a steady state groundwater flow towards a well in a confined aquifer of uniform thickness z_a . The steady-state head equation then reads

$$-\nabla (K(\mathbf{x}) \nabla h(\mathbf{x})) = -\nabla \left(\bar{K} + \tilde{K}(\mathbf{x}) \right) \nabla h(\mathbf{x}) = 0. \quad (4.1)$$

The well is located at the origin of the three-dimensional coordinate system and r is the radial distance from the well. As boundary condition at the well one may use a constant head $h(r = r_w) = h_w$ [m] or a constant pumping rate Q_w [$m^3 s^{-1}$]. In the far field of the well, irregular boundary effects are excluded by assuming a circular outer constant head boundary, $h(r = r_d) = h_0$.

The conductivity is assumed to be log-normally distributed in three spatial dimensions (Matheron, 1967). In this model, values close to the mean tend to build field-spanning structures where extreme values are less connected. The conductivity $K(\mathbf{x})$ is then given by

$$K(\mathbf{x}) = K_0 \exp \left(\tilde{f}(\mathbf{x}) \right), \quad (4.2)$$

where $\tilde{f}(\mathbf{x})$ is a spatial normally distributed function (with zero mean and correlation function given by Eq. (4.3)). For mathematical reasons, we choose a Gaussian shaped correlation function

$$w_f(\mathbf{x} - \mathbf{x}') = \sigma_f^2 \exp \left[- \sum_{i=1}^N \frac{(x_i - x'_i)^2}{\xi_i^2} \right] \quad (4.3)$$

where σ_f^2 is the variance and ξ_i is the correlation length of $\log K(\mathbf{x})$ in i -th direction. In this study, the domain has the dimension $N = 3$ and the correlation lengths are identical in the horizontal plane, $\xi_1 = \xi_2 = \xi_h$ and smaller in vertical direction, $\xi_3 = \xi_v \ll \xi_h$. In addition, the correlation lengths in all directions ξ_i are smaller than the range r_d of the pumping test.

4.3 Coarse Graining for 3-dimensional short range well flows

In the previous Chapter 3, we introduced a non-uniform filter method and applied it to large scale well flows in two spatial dimensions. Here we extend this method to three dimensional pumping tests. The most appropriate coordinate system for a three dimensional pumping test is the cylindrical. To this end, we propose to apply the radial filter according to Schneider and Attinger (2008) in the horizontal plane and no filter in vertical direction. This filter is suited best to reproduce the whole drawdown as response to the pumping test as we have explained in detail in Schneider and Attinger (2008). The filtered pressure $\langle h(\mathbf{x}) \rangle_r$ then is defined as

$$\langle h \rangle_r \equiv \int d^3 x' h(\mathbf{x} - \mathbf{x}') u_r(\mathbf{x}') \quad (4.4)$$

with the filter

$$u_r(\mathbf{x}') = \frac{1}{\pi r^2} \exp\left(-\frac{x_1'^2 + x_2'^2}{r^2}\right) \delta(x_3') \quad (4.5)$$

where x_i is the component of \mathbf{x} in direction i . As $r \rightarrow 0$, the points near \mathbf{x} tend to be more weighted, so $\langle h(\mathbf{x}) \rangle_r \rightarrow h(\mathbf{x})$ as $r \rightarrow 0$.

The resulting filtered head equation looks very similar to the original one with small but important changes,

$$-\nabla \left(K^{\text{CG}}(r) + \left\langle \tilde{K}(\mathbf{x}) \right\rangle_r \right) \nabla \langle h(\mathbf{x}) \rangle_r = 0 \quad (4.6)$$

The effective conductivity depends on the radial filter r and is the sum of the new mean $K^{\text{CG}}(r)$ and the residual fluctuating part of the conductivity $\left\langle \tilde{K}(\mathbf{x}) \right\rangle_r$.

Making use of lowest order perturbation theory, we find length expressions as derived and stated in appendix A. For isotropic media, the result can be approximated very well by

$$K^{\text{CG}}(r) = K_g \left(1 + \frac{1}{6} \sigma_f^2 + \frac{1}{3} \sigma_f^2 \left(\frac{1}{1 + r^2/\xi_h^2} \right)^{3/2} \right). \quad (4.7)$$

and exponentiation then gives

$$K^{\text{CG}}(r) = K_{\text{efu}} \exp \left(\frac{1}{3} \sigma_f^2 \left(\frac{1}{1 + r^2/\xi_h^2} \right)^{3/2} \right). \quad (4.8)$$

According to Dean et al. (1996) and Attinger (2003), the renormalization is exact for isotropic media and isotropic filters. In particular, it equals the exponentiation of the lowest order perturbation theory result.

Isotropy is a special case of the given correlation function Eq. (4.3), where the effective conductivity for uniform flow K_{efu} generally reads

$$K_{\text{efu}} = K_g \exp \left(\sigma_f^2 \left(\frac{1}{2} - \gamma(e) \right) \right) \quad (4.9)$$

with $\gamma(e)$ given in Appendix 4.6 (under isotropic conditions $\gamma(e = 1) = 1/3$).

For anisotropic media, we find a very similar result

$$K^{\text{CG}}(r) = K_g \left[1 + \sigma_f^2 \left(\frac{1}{2} - \gamma(e) \right) + \frac{1}{3} \sigma_f^2 \left(\frac{1}{1 + \beta(e)r^2/\xi_h^2} \right)^{3/2} \right].$$

Exponentiation then gives

$$K^{\text{CG}}(r) = K_{\text{efu}} \exp \left(\frac{1}{3} \sigma_f^2 \left(\frac{1}{1 + \beta(e)r^2/\xi_h^2} \right)^{3/2} \right). \quad (4.10)$$

In case of anisotropic media or anisotropic filters, renormalization is not exact anymore but still yields reliable results for anisotropy ratios up to 0.1 (Dean et al., 1996).

Further, simplifying the smoothed but still heterogeneously distributed conductivity field, we proposed in Schneider and Attinger (2008) to approximate the transmissivity field by its harmonic mean in case of constant flux (Neumann) boundary conditions and by its arithmetic mean in case of constant head (Dirichlet) boundary conditions. For small scale pumping tests, the dominating hydraulic property is conductivity instead of transmissivity. The effective notation of the steady state flow equation then is

$$-\nabla K^{\text{eff}}(r) \nabla h^{\text{eff}}(r) = 0, \quad (4.11)$$

with the Dirichlet boundary condition

$$h^{\text{eff}}(r = 0) = h_w \quad (4.12)$$

resulting in

$$K_D^{\text{eff}}(r) \equiv K_{\text{efu}} \exp \left(\frac{1}{3} \frac{\sigma_f^2}{\left(1 + \beta(e) \frac{r^2}{\xi_h^2}\right)^{3/2}} \right) \quad (4.13)$$

as the effective conductivity equation for the constant head boundary condition. For Neumann boundary conditions

$$-K^{\text{eff}}(r=0)\nabla h^{\text{eff}}(r=0) = Q_w, \quad (4.14)$$

we find

$$K_N^{\text{eff}}(r) \equiv K_{\text{eff}} \exp \left(-\frac{1}{3} \frac{\sigma_f^2}{\left(1 + \beta(e) \frac{r^2}{\xi_h^2}\right)^{3/2}} \right). \quad (4.15)$$

4.4 Inversion of 3-D pumping test data by Firmani et al. (2006)

Within this section, we are going to reinterpret data from Firmani et al. (2006) as displayed in their *Figures 5 and 11*. These data are separated into three sets: set A are data from their *Figure 5* for constant flux (Neumann boundary condition) where set B are data from their *Figure 5* for constant head (Dirichlet boundary condition). Data set C are recalculated data from their *Figure 11* for flux proportional to local K (comparable to Dirichlet boundary condition).

Our aim is to reproduce the drawdown and pumping rates of all three sets by a virtual pumping test with K_N^{eff} respectively K_D^{eff} as conductivity fields. K_N^{eff} and K_D^{eff} explicitly depend on the four parameters: σ_f^2 , ξ , e and

K_{efu} . They are estimated inversely by finding the best fit of virtual forward simulations with the drawdown data by Firmani et al. (2006).

The factor $\beta(e)$ in Eq. (4.13) and (4.15) counts for the influence of the anisotropy ratio e . Evaluating Eq. (4.13) and (4.15), we find that the effective conductivity only depends very weakly on the anisotropy factor. It explains the findings of Firmani et al. (2006) that e is difficult to inversely estimate.

To quantify this effect within our inversion procedure, we make the distinction between two inversion steps. For step I, we assume that e is known a priori, thus the parameter estimation includes beside the variance σ_f^2 and the geometric mean K_g only the horizontal correlation lengths ξ_h . Regarding inversion step II, we assume the anisotropy ratio to be unknown like all other parameters unknown and, thus, re-include e into the estimation procedure.

4.4.1 Numerical setup

The conductivity values are defined on an uniform rectangular grid of 256x256 quadratic cells with a refined well cell. The uniform grid spacing is $\Delta x = \Delta y = 0.2I_h$, hence the total spatial domain is $51.2I_h \times 51.2I_h$, where the well grid cell spacing is $\Delta x_w = \Delta y_w = 0.04I_h$. This is done to accomplish the comparison of our model results with the data simulations

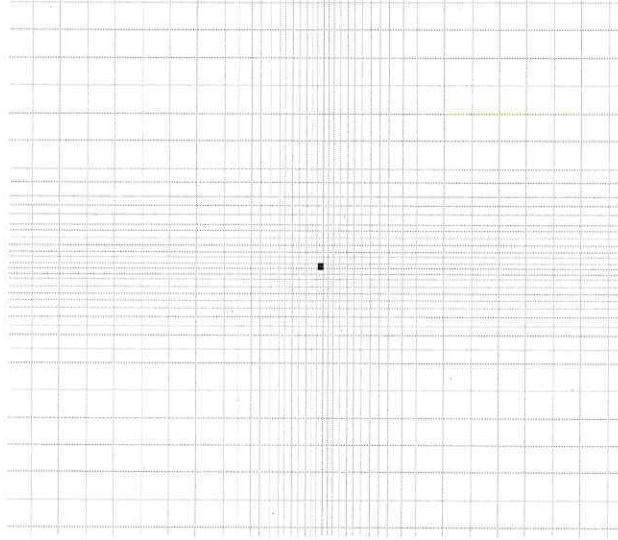


Figure 4.1: Grid refinement near the well.

of Firmani et al. (2006) as their grid at the well is also refined up to a factor of 5 (for details see Figure 4.1).

For the inner boundary of data set A we apply a constant flux of $Q_w = -0.0001[m^3/s]$ and at the outer boundary $h(r_d = 128\Delta x) = 0[m]$. For data set B and C we assume a constant head of $h(r_w) = -1.5[m]$ at the well and at the outer boundary $h(r_d = 128\Delta x) = 0[m]$. The aquifer thickness is set to $z_a = 1$. For the numerical grid, all simulations are performed under the assumption of a theoretical horizontal integral scale of $I_h = 3[m]$, the equivalent well radius was tested to be $r_w = 0.0237[m]$. Since we are using

a Gaussian correlation function Eq. (4.3), comparing the correlation length ξ with the integral scale I used by the exponential correlation function of Firmani et al. (2006); ξ has to be scaled according to $I = \sqrt{\pi}/2 \ \xi$. The characteristic relation plotted on the y-axis in *Figure 5* of Firmani et al. (2006) (divided by K_g) as well as recalculations of K_{eq} shown in their *Figure 11* are the basis for inversely estimating the statistical parameters of the conductivity field.

4.4.2 Step I: estimation of horizontal integral scale, geometric mean and variance

In a first attempt, we assume e to be known a priori and set $\beta(e = 1) = 1$ for data sets A and B, where $\beta(e = 0.1) = 1.18$ for data set C (see Appendix 4.6 for derivation or Figure 4.3). Doing so, we infer in the following only the horizontal integral scale, the geometric mean and the variance of the heterogeneous conductivity field. This procedure lacks in estimating e and hence the vertical integral scale $I_v = e \times I_h$, which will be overcome later by step II. For the isotropic data sets A and B ($e = 1$), K_{efu} can be replaced in equation Eq. (4.13) respectively (4.15) by $K_g \exp\left(\frac{1}{6}\sigma_f^2\right)$ where for data set C (anisotropic case, $e = 0.1$), we substitute K_{efu} by $K_g \exp\left(0.43\sigma_f^2\right)$.

In Table 4.1 we present the results of our inversion for the Neumann boundary (data A) and Dirichlet boundary (data B and C), where for A and B

	$I_h = \sqrt{\pi}/2 \xi_h$ [m]	e (fixed)	K_g $10^{-4}[m/s]$	σ_f^2
expect. param. estim. param.	3	1	1	0.2
Data Set A, Eq. (4.15)	2.8924 (± 0.5605)	-	0.9892 (± 0.0115)	0.2193 (± 0.0126)
Data Set B, Eq. (4.13)	3.5478 (± 0.6474)	-	0.9882 (± 0.016)	0.2314 (± 0.0238)
expect. param. estim. param.	3	0.1	1	0.5
Data Set C, Eq. (4.13)	2.9346 (± 0.4274)	-	0.8945 (± 0.0175)	0.5163 (± 0.0329)

Table 4.1: Inverse evaluation for step I; Values within parenthesis indicate the 95% confid. interval.

the x-axis (r/I_h) in *Figure 5* of Firmani et al. (2006) is scaled for numerical reasons to $I_h = 3[m]$.

We find an excellent agreement with the theoretical values. Only for Data Set C, the geometrical mean K_g is underestimated by about 10%, where it fits well for Data Set A and B. Nevertheless, the horizontal integral scale and the variance match quite well for all three data sets. These inverse values show also acceptable confidence intervals. Due to fixing the anisotropy rate e , we reduced the degree of freedom for our estimation procedure step I. Therefore the data are fitted to Eq. (4.15) respectively (4.13) which include only three instead of four free parameters giving smaller confidence bands. This will be contrasted by the results of inversion procedure step II.

	I_h [m]	e ($= I_v/I_h$)	K_g $10^{-4}[m/s]$	σ_f^2
expect. param. estim. param.	3	1	1	0.2
Data Set A, Eq. (4.15)	3.6348 (± 1.9300)	0.9212 (± 0.5222)	0.998 (± 0.0195)	0.1980 (± 0.0785)
Data Set B, Eq. (4.13)	3.0792 (± 0.7919)	1.2386 (± 0.6066)	0.9983 (± 0.0199)	0.2156 (± 0.0967)
expect. param. estim. param.	3	0.1	1	0.5
Firmani et al. (2006) (for $N_w = 7$)	<i>4.059</i> (± 0.855)	<i>1.000</i> (± 1.860)	<i>1.032</i> (± 0.156)	<i>0.473</i> (± 0.307)
Data Set C, Eq. (4.13)	3.3102 (± 0.6439)	0.1478 (± 0.0700)	0.9020 (± 0.0236)	0.5211 (± 0.0853)

Table 4.2: Inverse evaluation for step II; Values within parenthesis indicate the 95% confid. interval.

4.4.3 Step II: additional estimation of anisotropy ratio

For step II, we estimate all four parameters of Eq. (4.15) respectively (4.13). In comparison to step I, we will now additionally include estimating the anisotropy ratio of the hydraulic conductivity field. Since our inversion procedure does not give the anisotropy factor directly, we will calculate e and thus the integral scale $I_v = e \times I_h$ by estimating the corresponding factor $\beta(e)$. The functional relationship between β and e is interpolated and shown in Figure 4.3.

For data set C (see Table 4.2), we find that all parameter estimates for the horizontal integral scale, the anisotropy ratio and the variance are closer to their theoretical values than in Firmani et al. (2006). Although e introduces a new degree of freedom in our inverse estimation for step II, we still find a good agreement of our values and the expected parameters for all three data sets except the estimated K_g for data set C that shows again some underestimation (like in step I). In general, the confidence bands in step II show more spread than for step I, which is the result of including a fourth parameter in the estimation procedure but still relying on the same data. This is especially the case for the correlation lengths and the variance, where the confidence intervals of the estimated geometric mean show approximately the same variability for step II than for step I. However, the confidence band of the anisotropy ratio - with a variation of about $\pm 50\%$ - is much better than the interval of e given by Firmani et al. (2006).

Figure 4.2 includes the drawdown data of our simulations (with the estimated, mean parameters shown in Table 4.2) and the data extracted from Firmani et al. (2006) for sets A, B and C. The good agreement between the depth averaged hydraulic head \bar{h} of their simulated, single 3D pumping test and our simulated drawdowns of the coarse grained conductivity fields shows that the proposed method can be used for the interpretation of the given data. This holds both, for a flux and a head boundary condition, as long as ergodicity does not break at the well (i.e. the aquifer thickness is much larger than the vertical correlation length).

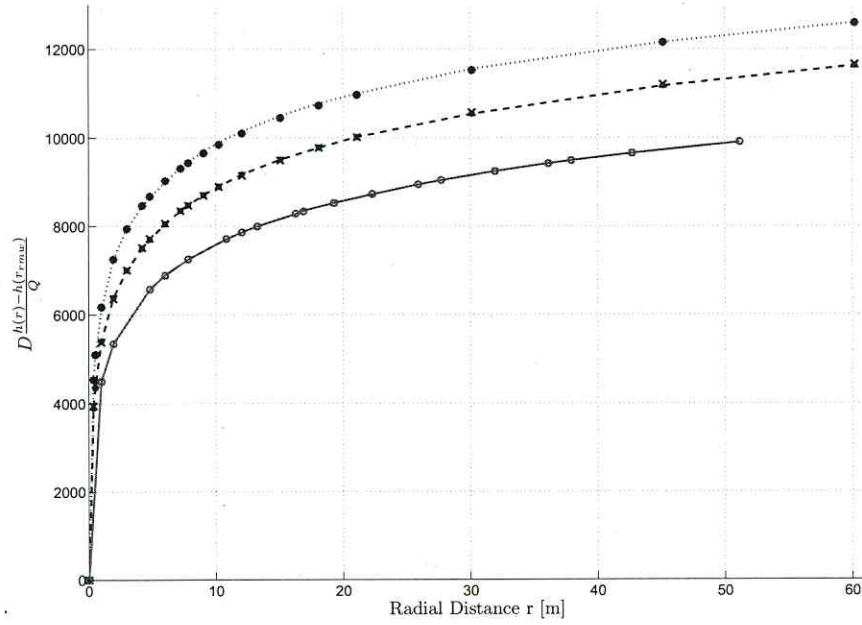


Figure 4.2: Data (lines) and our simulations (markers) for set A, B and C; dotted line respectively asterisks are for set A, dashed line respectively crosses are for set B and solid line respectively circles are for set C. The parameters used for our simulations stem from the inversion procedure (the estimated mean values) and are listed in Table 4.2.

4.4.4 Limitations of the proposed procedure

We wish to emphasize two general limitations. Firstly, for low variances ($\sigma_f^2 < 0.2$), the effective conductivity field becomes more and more homogeneous and the estimation of the horizontal integral scale shows an increasing confidence interval. This holds also for the anisotropy ratio. Secondly, application of Dirichlet boundaries implies an effective conductivity equal to the arithmetic mean close to the well (Eq. (4.13)). On the other hand, the effective conductivity in the far field of the well, K_{eff} , is close to the arithmetic mean for highly anisotropic media. Hence, in this cases the finding that the integral scale determines the transition behavior of the effective conductivity between the vicinity and the far field of the well becomes inappropriate because the effective conductivity is close to the arithmetic mean for all distances of r . Therefore, for highly anisotropic media the integral scales are difficult to estimate by our procedure.

4.5 Summary and conclusion

For groundwater modeling, a hydraulic characterization and parameterization of heterogeneous aquifers is a prerequisite (Rubin, 2003). A detailed characterization of aquifers is very often neither feasible nor affordable. Alternatively, a statistical description of the aquifer is a valuable option. Heterogeneous conductivity fields are often characterized by a log normal distribution in space defined by three parameters: the geometric mean K_g

that impacts the effective groundwater velocity, the integral scales I_i respectively correlation lengths ξ_i and the variance σ_f^2 . Within this chapter, the main objective was to develop a new method to infer these geostatistic parameters and to improve in particular the estimates for the integral scale/correlation length from local pumping test data as simulated in virtual pumping tests by Firmani et al. (2006).

Applying the filtering method Coarse Graining, we derived a closed formula for $K^{\text{eff}}(r)$, which describes a short range pumping test performed in an aquifer of a thickness much larger than the vertical correlation length (according to Firmani et al. (2006) at least $60 \xi_v$). The explicit result for the effective pumping test model and $K^{\text{eff}}(r)$ reads

$$K_{D,N}^{\text{eff}}(r) \equiv K_{\text{efu}} \exp \left(\pm \frac{1}{3} \frac{\sigma_f^2}{\left(1 + \beta(e) \frac{r^2}{\xi_h^2}\right)^{3/2}} \right), \quad (4.16)$$

where the algebraic sign depends on the imposed boundary condition at the well (+ for Dirichlet and – for Neumann condition). We used this formula to infer the integral scales, the anisotropy ratio, the variance and the geometric mean within the virtual pumping tests of Firmani et al. (2006). Our estimates were in very good agreement to the theoretical (virtual) values. Therefore, we propose to test the derived method under field conditions in order to estimate the statistical properties of natural heterogeneous aquifers.

4.6 Appendix

Following Schneider and Attinger (2008) and applying the proposed filter Eq. 4.5, the formula for $K^{\text{CG}}(r)$, making use of Fourier integrals, reads

$$K^{\text{CG}}(r) = K_g(1 + \sigma_f^2 - \sigma_f^2 \int d^3\nu \left[\exp(-\frac{\nu_1^2 + \nu_2^2}{\xi^2}) - \frac{\nu_3^2}{\xi_3^2} \frac{\nu_1^2}{q^2} (1 - \exp(-\frac{\nu_1^2 + \nu_2^2}{r^2})) \right]).$$

Evaluation of the three dimensional integral gives

$$K^{\text{CG}}(r) = K_g(1 + \sigma_f^2 - \sigma_f^2 \gamma(e) + \delta K^{\text{CG}}(r)). \quad (\text{A-4.1})$$

The function $\delta K^{\text{CG}}(r)$ is given by

$$\delta K^{\text{CG}}(r) = \frac{1}{4} \frac{e \xi_h^3 \left(\pi l_1 l_2 - 2 l_2^2 \frac{e \xi_h}{l_1} - 2 l_1 l_2 \arcsin\left(\frac{e \xi_h}{l_1}\right) \right)}{l_2^4 l_1}, \quad (\text{A-4.2})$$

with $l_1 = \sqrt{\xi_h^2 + r^2}$ and $l_2 = \sqrt{\xi_h^2(1 - e^2) + r^2}$. The latter solution can be approximated very well by the expression given in Eq. (4.13) respectively (4.15) with the $\beta(e)$ -function as plotted in Figure 4.3.

The $\gamma(e)$ -function in Eq. (4.9) is given for a Gaussian shaped correlation function Eq. (4.3) by

$$\gamma(e) = \frac{1}{4} \frac{e \left(\pi \sqrt{1 - e^2} + 2e^3 - 2e - 2\sqrt{1 - e^2} \arcsin(e) \right)}{(e^2 - 1)^2}, \quad (\text{A-4.3})$$

and bounded between $\gamma(e \rightarrow 0) = 0$ and $\gamma(e = 1) = 1/3$.

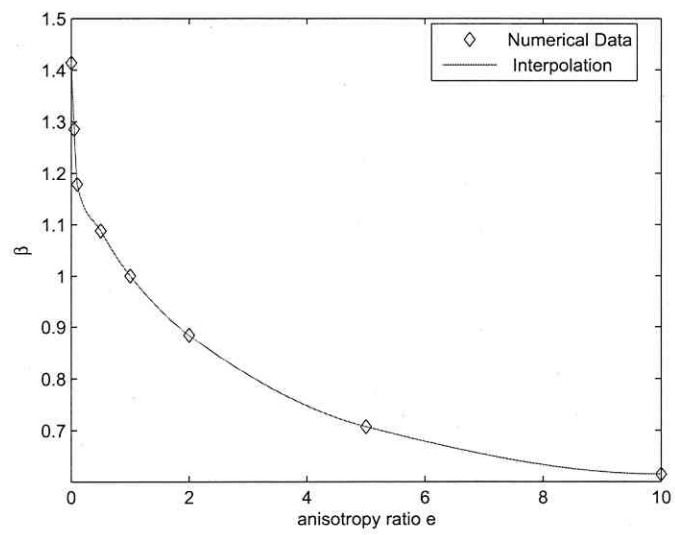


Figure 4.3: $\beta(e)$ plotted versus the anisotropy ratio e .

Bibliography

- Attinger, S. (2003). "Generalized Coarse Graining Procedures for Flow in Porous Media". In: *Comput. Geosci.* 7.4, pp. 253–273. DOI: 10.1023/B:COMG.0000005243.73381.e3.
- Dagan, G. and S. C. Lessoff (2007). "Transmissivity upscaling in numerical aquifer models of steady well flow: Unconditional statistics". In: *Water Resour. Res.* 43, W05431. DOI: 10.1029/2006WR005235.
- Dean, D.S. et al. (1996). "Renormalization of drift and diffusivity in random gradient flows". In: *J. Phys. A: Math. Gen.* 29.24, pp. 7867–7879. DOI: 10.1088/0305-4470/29/24/012.
- Fiori, A. et al. (1998). "Correlation structure of flow variables for steady flow toward a well with application to highly anisotropic heterogeneous formations". In: *Water Resour. Res.* 34, pp. 699–708.
- Firmani, G. et al. (2006). "Three-dimensional numerical analysis of steady state pumping tests in heterogeneous confined aquifers". In: *Water Resour. Res.* 42, W03422. DOI: 10.1029/2005WR004382.

- Indelman, P. et al. (1996). "Steady flow toward wells in heterogeneous formations: Mean head and equivalent conductivity". In: *Water Resour. Res.* 32.7, pp. 1975–1984. DOI: 10.1029/96WR00990.
- Matheron, G. (1967). *Elements pour une theorie des milieux poreux*. Paris: Maisson et Cie.
- Rubin, Y. (2003). *Applied Stochastic Hydrogeology*. New York: Oxford Univ. Press.
- Sánchez-Vila, X. et al. (2006). "Representative hydraulic conductivities in saturated groundwater flow". In: *Rev. Geophys.* 44, RG3002. DOI: 10.1029/2005RG000168.
- Schneider, C. L. and S. Attinger (2008). "Beyond Thiem: A new method for interpreting large scale pumping tests in heterogeneous aquifers". In: *Water Resour. Res.* 44.W04427. DOI: 10.1029/2007WR005898.

Chapter 5

Theoretical background II: unsaturated water flow and root water uptake

In Chapter 2 we introduced the main principles of water flow through porous media and in the saturated zone. Here, we extend these derivations to water flow in the unsaturated zone with a special interest on root water uptake.

5.1 Soil water flow

Like in saturated media, water in the unsaturated soil moves from points of higher potential to points of lower potential. In unsaturated media, this total water potential can be written as the sum of all possible component potentials (Hopmans and Bristow, 2002). The main components are the matric and the gravitational potentials. The gravitational component counts for the elevation of water in the soil profile relative to a given reference level. Since water is flowing through a solid matrix (for example clay or sand particles) within the soil, adhesive forces between the water and the solid will appear. The matric potential is caused by a combination of such capillary and surface forces. It is negative if not all water pores are filled. The hydraulic head at a given point in the soil is equal to the sum of the gravitational and matric potential at that point and is commonly used as an approximation of total water potential. Other potentials like osmotic potential due to salinity are usually neglected because of their low contribution to the potential gradients.

Assuming the validity of the Darcy equation for the given potential concept in unsaturated media, water flow is described by

$$q = -K_s k(\psi) \nabla (\psi + z), \quad (5.1)$$

where q [$m s^{-1}$] is the volumetric flux, $K_s k(\psi)$ [$m s^{-1}$] the unsaturated soil hydraulic conductivity, ψ [m] the matric potential (expressed in pressure head) and z [m] the vertical coordinate (upwards). An important difference to water flow in the saturated zone is, that hydraulic conductivity is a function of matric potential.

Combining the flow equation with mass conservation (similar to section 2.1.3) yields the Richards' equation, which describes the water movement in the unsaturated soil

$$\frac{\partial \theta}{\partial t} = \nabla [K_s k(\psi) \nabla (\psi + z)], \quad (5.2)$$

where θ [$m^3 m^{-3}$] is the volumetric soil water content and t [s] is the time.

The volumetric water content can also be expressed as a function of water potential by

$$\theta = \theta(\psi) = \theta(\psi^{ref}) + \int_{\psi^{ref}}^{\psi} C(\psi') d\psi', \quad (5.3)$$

with ψ^{ref} a reference matric potential and $C(\psi)$ [m^{-1}] the water capacity defined as $\partial \theta / \partial \psi$. This gives the Richards' equation in matric potential notation

$$C(\psi) \frac{\partial \psi}{\partial t} = \nabla [K_s k(\psi) \nabla (\psi + z)]. \quad (5.4)$$

At the moment no analytical solution of Equation 5.4 is known since it is highly nonlinear in its parameters k and C . Also solving this equation

numerically, can be demanding due to the large nonlinear dependencies of both water content and unsaturated hydraulic conductivity on the soil water matric potential.

There are several ways to parameterize the functions $k(\psi)$ and $\theta(\psi)$. For example, one of the most common functional relationships, beside the approaches of Campbell or Brooks-Corey, is the Mualem-van-Genuchten parameterization (van Genuchten, 1980). The latter is the one, which is used in this thesis.

Water retention curve Following the Mualem-van-Genuchten model, the relation between the volumetric soil water content $\theta[m^3m^{-3}]$ and the matric potential ψ given in Eq. (5.3) can be expressed as

$$\frac{\theta - \theta_r}{\phi - \theta_r} = \Theta = \left[\frac{1}{1 + |\alpha\psi|^n} \right]^m. \quad (5.5)$$

Hydraulic conductivity Accordingly, hydraulic conductivity $K [m s^{-1}]$ in dependency on relative water content is given by Mualem-van-Genuchten as

$$K(\Theta) = K_s k(\Theta) = K_s \Theta^\lambda \left(1 - \left(1 - \Theta^{\frac{1}{m}} \right)^m \right)^2, \quad (5.6)$$

where Θ can also be replaced by θ making use of Eq. (5.5).

Hydraulic diffusivity Another important variable in the soil-water relationship is hydraulic diffusivity $D [m^2 s^{-1}]$ (also named soil water diffu-

sivity) defined by Θ as

$$D(\Theta) = K(\Theta) \frac{d\psi}{d\Theta}. \quad (5.7)$$

For the Mualem-van-Genuchten parameterizations, ψ is given by the inverse function of Eq. (5.5), namely,

$$\psi = -\frac{(\Theta^{-1/m} - 1)^{1-m}}{\alpha}. \quad (5.8)$$

Thus, $D(\Theta)$ becomes

$$D(\Theta) = -K(\Theta) \frac{(m-1)\Theta^{(1-m)/m} (\Theta^{-1/m} - 1)^{-m}}{m\alpha}, \quad (5.9)$$

which can be transformed by inserting Eq. (5.6) after various manipulations to

$$D(\Theta) = D_s \tilde{\partial}(\Theta) = D_s \Theta^{\lambda-1/m} \left[(1 - \Theta^{1/m})^{-m} - 2 + (1 - \Theta^{1/m})^m \right], \quad (5.10)$$

with $D_s = K_s(1-m)/(\alpha m)$ is the saturated hydraulic diffusivity.

In terms of relative water content Θ , the Richards' equation can be formulated as

$$\phi \frac{\partial \Theta}{\partial t} = \nabla [D_s \tilde{\partial}(\Theta) \nabla \Theta + K e_z], \quad (5.11)$$

where e_z is the unit vector upwards.

Linearization by matric flux potential As already discussed in the previous paragraphs, no general analytical solution of the Richards' Equation (Eq. 5.4) exists because of the nonlinearities in its parameters. To circumvent this problem, the second order term in the Richards' equation can be linearized by making use of an integral transformation. Using a term called matric flux potential Φ [$m^2 s^{-1}$] given at the current soil water potential ψ respectively water content θ by

$$\Phi(\psi, \theta) - \Phi^{ref} = \int_{\psi^{ref}}^{\psi} K(\psi') d\psi' = \int_{\theta^{ref}}^{\theta} D(\theta) d\theta, \quad (5.12)$$

where Φ^{ref} , ψ^{ref} and θ^{ref} are reference states of the system (for $\psi^{ref}, \theta^{ref} \rightarrow -\infty$ the reference matric flux potential tends toward zero $\Phi^{ref} \rightarrow 0$), hence resulting in

$$\Phi(\psi, \theta) = \int_{-\infty}^{\psi} K(\psi') d\psi' = \int_{-\infty}^{\theta} D(\theta) d\theta. \quad (5.13)$$

5.2 Root water uptake

The process of water transport within the soil-plant-atmosphere continuum can be best described by a simple electric analogue (Van den Honert, 1948). The water flow is driven by a gradient of total water potential between the soil and the atmosphere. The atmospheric water deficit and the soil

water status determine the flow across several components, that are the soil matrix, the root system, the plant's stem and the plant's leaf.

Plant transpiration is regarded as the reason for the water uptake by roots. Considering the constituent pathways of this water flow, most of the plant resistance is concentrated in the roots (Feddes and Raats, 2004). The soil resistance is inversely related to the soil hydraulic conductance that appears along the flow path from the soil matrix towards the root. Regarding the overall flow resistance, soil resistance might become important when soil gets dry (Cowan, 1965).

Water uptake by plants can be studied at two different scales: the plot scale or the microscale. A review on approaches of modeling root water uptake at several scales has been published by Hopmans and Bristow (2002), Feddes and Raats (2004) and most recently Raats (2007). At the plot scale, root water uptake is commonly treated as a bulk water extractor and introduced as a sink term to the water flow Eq. (5.4). Unlike, at the microscopic scale, the water movement is explicitly modeled along the uptake path from the soil to the atmosphere. This approach resolves the soil water flow in the vicinity of the roots and within the plant's water transmitting components. The two approaches are presented in the following sections.

Root water uptake at the plot scale At the plot scale, the soil water flow is usually assumed to appear only in the vertical direction, which makes the Richards' equation (see Eq. 5.4) one dimensional. The root

water uptake is then inserted as a vertical sink term ϱ into the Richards' equation resulting in

$$C(\psi) \frac{\partial \psi}{\partial t} = \frac{\partial}{\partial z} \left[K_s k(\psi) \left(\frac{\partial \psi}{\partial z} + 1 \right) \right] - \varrho(z, t). \quad (5.14)$$

The sink term function $\varrho(z, t)$ [s^{-1}] is usually assumed to follow a vertical profile of root abundance. Hence, the potential root water uptake rate at a certain root depth is often related to the vertical root length density $L_V^a(z)$ [$m\ m^{-3}$] like

$$\varrho_{Pot}(z, t) = \frac{L_V^a(z)}{\int_{z_d}^0 L_V^a(z) dz} q_{Pot}(t), \quad (5.15)$$

with $q_{Pot}[ms^{-1}]$ the potential transpiration flux and rooting depth z_d .

Under optimal soil moisture conditions the potential extraction rate $\varrho_{Pot}(z)$ integrated over rooting depth z_d is assumed to equal the potential transpiration rate that is governed by the atmospheric water deficit. Stress due to dry or wet conditions (and/or high salinity concentrations) may reduce the potential uptake rate. Then, $\varrho_{Pot}(z)$ is multiplied by a reduction coefficient counting for water stress (β_{rw}). This will give the current uptake rate $\varrho(z, t)$ as

$$\varrho(z, t) = \beta_{rw} \times \varrho_{Pot}(z, t). \quad (5.16)$$

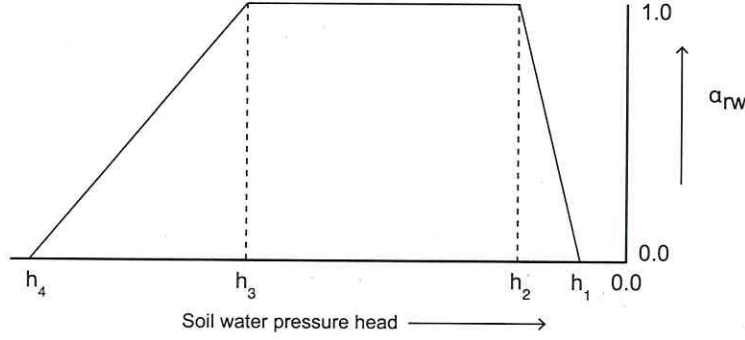


Figure 5.1: Water stress function used in the Feddes model: Water uptake above ψ_1 and below ψ_4 is set to zero due to oxygen deficit and wilting point. Between ψ_2 and ψ_3 water uptake is maximal ($\beta_{rw} = 1$). Above ψ_2 and below ψ_3 , the so-called critical point, water uptake gets limited where the precise value of ψ_3 is assumed to vary with potential transpiration rate T_{Pot} .

The most common implemented water stress function β_{rw} has the form shown in Figure 5.1 (similar to Feddes et al. (1976)).

In summary, the macroscopic approach reflects the water uptake from the root zone as a whole, without considering explicitly the effects of single roots, the radial flow towards them or the radial and axial flow within the root system. Root water uptake modeled at the plot scale follows, due to reasons of simplicity, the common root length density approach (see Eq. 5.15). Then root abundance is used to distribute plant transpiration over

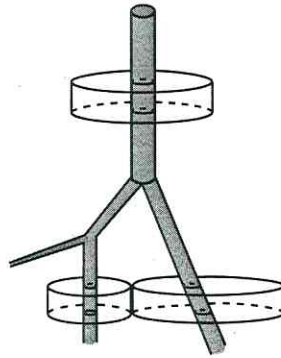


Figure 5.2: Scheme of soil cylinders around root nodes

the soil layers affected by the rooting density profile. This methodology is commonly applied in many soil-vegetation-atmosphere-transfer (SVAT) schemes (see Chapter 6 for further details).

Root water uptake at the microscale The microscopic approach considers explicitly the water flow along the uptake path from the soil via vegetation to the atmosphere. Here, we first explore the radial pathway of water flowing from the (bulk) soil to the root surface. The flow within the root up to the root collar will then be explained in the next section.

Radial soil water flow At the microscopic scale, plant water uptake consists of a flow from the soil towards the root surface. The soil water flow is then modeled as the radial movement of water from the outer boundary of a soil disc with radius r_{disc} towards a single root segment of radius r_0 as

illustrated in Figure 5.2. The uptake rate is given by a boundary flux at the soil-root-interface.

The most sophisticated method for calculating water flow towards a single root is the Richards' equation in radial coordinates that covers the full nonlinearity of the flow process. In transient state, the radial (1D) Richards' equation reads in matric potential notation

$$C(\psi) \frac{\partial \psi}{\partial t} = \frac{1}{r} \frac{\partial}{\partial r} \left[K_s k(\psi) r \frac{\partial \psi}{\partial r} \right] \quad (5.17)$$

Approximations of radial soil water flow One of the first descriptions for microscale radial water flow from the soil towards the root is the one of Gardner (1960). The Gardner model is still used today in some applications (Personne et al., 2003; Segal et al., 2006) as it proved to be very insightful (Vrugt et al., 2001). It considers the radial flow of soil water towards the root assuming a radially constant hydraulic conductivity. The root system is substituted by a vertical cylinder of uniform root radius r_0 , uniform hydraulic properties and a constant soil layer radius r_{disc} . For solving Eq. (5.17), Gardner assumed a steady state behavior for the water uptake along a cylinder of infinite length where the extraction rate is defined per unit root length ($\mathcal{Q} [m^3 s^{-1} m^{-1}]$). Under the described conditions (similar to the Thiem solution for saturated flow), he proposed the following expression

$$\mathcal{Q} = 2\pi K \ln \left(\frac{r_{disc}}{r_0} \right) (\psi_0 - \psi_{disc}), \quad (5.18)$$

where ψ_0 and ψ_{disc} are the matric potential at the soil root interface r_0 and the outer soil layer radius r_{disc} . Thus, the depletion resulting from uptake by a single root is treated as a series of steady state flows in a cylindrical soil disc with a homogeneous hydraulic conductivity along the radial distance. The assumption of constant hydraulic conductivity can be avoided, as shown in Cowan (1965), by replacing K with a radial averaged hydraulic conductivity along r that serves as an effective parameter updated at each time step. However, this approach still neglects the radial dependency between K and the matric potential $\psi(r)$. This results in a permanent overestimation of the averaged conductivity, particularly near the root surface (at the inner boundary).

Another approximative implementation of the Richards' equation in current root water uptake models is the steady rate approach (Jacobsen, 1974). Firstly, applying the concept of matric flux potential (Eq. 5.12) and introducing $D(\theta) = d\Phi/d\theta$, the Richards' equation becomes

$$\frac{1}{D(\theta)} \frac{\partial \Phi}{\partial t} = \frac{1}{r} \frac{\partial \Phi}{\partial r} + \frac{\partial^2 \Phi}{\partial r^2}. \quad (5.19)$$

Setting $1/D \partial \Phi / \partial t = \varrho = \text{const.}$ in Eq. (5.19), the steady rate equation then reads

$$\frac{1}{r} \frac{\partial \Phi}{\partial r} + \frac{\partial^2 \Phi}{\partial r^2} = \varrho \quad (5.20)$$

with the analytical solution

$$\Phi(r) = \frac{\iota_3}{4}r^2 + \iota_2 \ln(r) + \iota_1 \quad (5.21)$$

where ι_1 , ι_2 and ι_3 are integration constants set by the boundary conditions. Assuming the following boundary conditions for such a steady rate, radial flow

$$\begin{aligned} \left. \frac{\partial \Phi(r)}{\partial r} \right|_{r=r_0} &= q_{rad} = \frac{Q_{rad}}{2\pi r_0 l} && \text{inner boundary,} \\ \left. \frac{\partial \Phi(r)}{\partial r} \right|_{r=r_{disc}} &= 0 && \text{outer boundary (no flow),} \\ \Phi(r=r_b) &= \Phi_b && \text{bulk matrix flux potential at } r_b, \end{aligned} \quad (5.22)$$

we end up in the steady rate analytical solution

$$\Phi(r) = \Phi_b(r) + \frac{Q_{rad}}{2\pi l} \left[\frac{r^2/r_0^2}{2(1 - r_{disc}^2/r_0^2)} + \frac{r_{disc}^2/r_0^2}{1 - r_{disc}^2/r_0^2} \left(\ln\left(\frac{r_b}{r}\right) - \frac{r_b^2/r_{disc}^2}{2} \right) \right], \quad (5.23)$$

that is, depending on the imposed boundary conditions, similar to the work of De Willigen and Noordwijk (1987); Lier et al. (2006); Schröder et al. (2009). Here, we assume that the bulk soil water potential transformed to bulk matrix flux potential appears at a certain distance r_b , which was shown by Lier et al. (2006) to be a valid approximation. At the outer boundary a zero flux is imposed, whereas at the inner boundary, the flux is given by the coupling to the root water inflow. Eq. (5.23) is a good approximation

of the radial flow towards the root under transient conditions as shown in De Willigen and Noordwijk (1987).

Water flow within the plant roots Within the plant roots, water moves (1) from the root surface to the inner root xylem and (2) within the xylem vessels up to the root collar. The first pathway is called the radial flow path whereas the latter is referred to the axial flow. The water potential will decrease along the different components of the path. These potential gradients drive the radial and axial water flow (J^{rad} ; J^{ax} [$m^3 s^{-1}$]) and are described in analogy to Ohm's Law for each root segment as

$$J^{rad} = \frac{1}{R^{rad}} \left(\psi^{xylem} - \psi(r_0) \right), \quad (5.24)$$

and

$$J^{ax} = \frac{1}{R^{ax}} \left(\Delta\psi^{xylem} + \Delta z \right), \quad (5.25)$$

where Δ refers to the potential gradient along the root xylem axis between two root segments. Within this formulation, roots are modeled as a series of axial and radial resistances (R^{ax} ; R^{rad} [$s m^{-2}$]) as in Van den Honert (1948); Landsberg and Fowkes (1978). The introduced root resistances operate as an effective value for the underlying processes described below. They are plant- and age-specific and relate to the prescribed root order.

There is an ongoing debate on the range of the hydraulic properties of the root components appearing along the water flow path. The axial resistance

can be defined like in West et al. (1999)) by the number, radius and length of the evolved xylem vessels in correspondence to Poiseuille's Law (Greacen et al., 1976; Tyree and Ewers, 1991). Where the axial pathway seems to be well described, the range of hydraulic properties along the radial pathway shows a great uncertainty (Passioura, 1988; Rincon et al., 2003). This is partly due to the differences in functionality between the three possible pathways (apoplastic, symplastic and transcellular) to pass the radial flow path (Steudle and Peterson, 1998). Regarding the transmission of water, their findings suggest a relatively low conductivity of the radial pathway compared to the axial. On the other hand, Zwieniecki et al. (2003) find larger radial conductivities which is in contrast to the previous findings. Moreover, their results suggest that the capacity of a root to absorb water depends upon the combined axial and radial resistances. For this reason, both scenarios will be applied in parallel and compared within Chapter 7. Within our plant modeling framework, the root system forms a network of resistances including the axial and radial resistances of each individual root segment. When the root system branches, the network shows parallel flow paths. At the root collar, the up most part of the root system, either a transpirational flux or a transpirational water potential is assumed. Both entities are fixed by the atmospheric conditions together with the plant's remaining resistances in the stem and in the leaves.

In summary, the microscopic approach, used within this thesis, reproduces the small scale effects of root water uptake. On the one hand, this is the

local radial water flow from the soil towards the root that will be represented by Eq. (5.23). On the other hand, this is the water flow within the plant's root system along its several pathways.

In Chapter 6, we will focus on the local characteristics of the radial soil water flow within a split root modeling study. We are aiming to show the relevance of this local effects for the overall water uptake and compare them to current water uptake models. Chapter 7 will further elaborate on these outcomes by combining the microscopic soil water flow approach with the water flow within the plant's root system.

In this scope, we will try to answer the following two main questions:

1. How local hydraulic gradients in soil water potential influences overall root water uptake? (Chapter 6)
2. What role does root architecture plays in the water uptake process? (Chapter 7)

Bibliography

- Cowan, I.R. (1965). "Transport of water in the soil-plant-atmosphere system". In: *Journal of Applied Ecology* 2, pp. 221–239.
- De Willigen, P. and M. van Noordwijk (1987). "Root, Plant. Production and Nutrient Use Efficiency". PhD thesis. Agricultural University, Wageningen, Netherlands.
- Feddes, R. A. and P.C. Raats (2004). "Parameterizing the soil - water - plant root system". In: *Unsaturated-zone modeling; Progress, challenges and applications*. Ed. by R.A. Feddes et al. Wageningen UR Frontis Series 6. Dordrecht: Kluwer Academic Publishers, pp. 95 –141.
- Feddes, R.A. et al. (1976). "Simulation of field water uptake by plants using a soil water dependent root extraction function". In: *Journal of Hydrology* 31, pp. 13–26.
- Gardner, W. R. (1960). "Dynamics aspects of water availability to plants". In: *Soil Science* 89.2, pp. 63–73.

- Greacen, E. L. et al. (1976). *Resistance to water flow in the roots of cereals*. Ed. by E.-D. Schulze O. L. Lange L. Kappen. Berlin: SpringerVerlag, pp. 86–100.
- Hopmans, J.W. and K.L. Bristow (2002). “Current capabilities and future needs of root water and nutrient uptake modeling”. In: *Advances in Agronomy* 77, 104–175.
- Jacobsen, B. (1974). “Water and phosphate transport to plant roots”. In: *Acta Agriculturae Scandinavica* 24, pp. 55–60.
- Landsberg, J.J. and N.D. Fowkes (1978). “Water movement through plants”. In: *Annals of Botany* 42, pp. 493–508.
- Lier, Quirijn de Jong van et al. (2006). “Root water extraction and limiting soil hydraulic conditions estimated by numerical simulation”. In: *Vadose Zone Journal* 5, pp. 1264–1277. DOI: 10.2136/vzj2006.0056.
- Passioura, J. B. (1988). “Water transport in and to roots”. In: *Annual Review of Plant Physiology and Plant Molecular Biology* 39, pp. 245–65.
- Personne, Erwan et al. (2003). “Simulating water uptake in the root zone with a microscopic-scale model of root extraction”. In: *Agronomy for Sustainable Development* 23, pp. 153–168. DOI: 10.1051/agro:2002081.
- Raats, P. A. C. (2007). “Uptake of water from soils by plant roots”. In: *Transport in Porous Media* 68, pp. 5–28. DOI: 10.1007/s11242-006-9055-6.

- Rincon, C. Amalia et al. (2003). "Genotypic Differences in Root Anatomy Affecting Water Movement through Roots of Soybean". In: *International Journal Of Plant Sciences* 164.4, 543–551. DOI: 10.1086/375377.
- Schröder, T. et al. (2009). "Implementation of a microscopic soil-root hydraulic conductivity drop function in a 3D soil-root architecture water transfer model". In: *subm. to Vadose Zone Journal*.
- Segal, Eran et al. (2006). "Root Water Uptake Efficiency Under Ultra-High Irrigation Frequency". In: *Plant And Soil* 282, 333–341. DOI: 10.1007/s11104-006-0003-6.
- Steudle, Ernst and Carol A. Peterson (1998). "How does water get through roots?" In: *Journal of Experimental Botany* 49 (322), pp. 775–788. URL: <http://jxb.oxfordjournals.org/cgi/content/abstract/49/322/775>.
- Tyree, M. T. and F. W. Ewers (1991). "The hydraulic architecture of trees and other woody plants". In: *New Phytologist* 119.3, pp. 345–360.
- Van den Honert, T. H. (1948). "Wate transport in plants as a catenary process". In: *Discussions of the Farraday Society* 3, pp. 146–153.
- van Genuchten, M.Th. (1980). "A closed-form equation for predicting the hydraulic conductivity of unsaturated soils". In: *Soil Science Society of America Journal* 44, pp. 892–898.
- Vrugt, J. A. et al. (2001). "One-, two-, and three-dimensional root water uptake functions for transient modeling". In: *Water Resources Research*

37 (10), pp. 2457–2470. URL: <http://www.agu.org/journals/wr/v037/i010/2000WR000027/>.

West, Geoffrey B. et al. (1999). “A general model for the structure and allometry of plant vascular systems”. In: *Nature* 400, pp. 664–667. DOI: 10.1038/23251.

Zwieniecki, Maciej A. et al. (2003). “Understanding the Hydraulics of Porous Pipes: Tradeoffs Between Water Uptake and Root Length Utilization”. In: *Journal of Plant Growth Regulation* 21, pp. 315–323. DOI: 10.1007/s00344-003-0008-9.

Chapter 6

The split root modeling study in the unsaturated zone ³

6.1 Introduction

Plant water uptake is one of the major processes influencing soil moisture and soil water fluxes. Limiting soil moisture on the other hand, influences the shape of ecosystems as well as water and energy fluxes to the atmo-

³This chapter is a modified version of the manuscript: Hildebrandt, A., Schneider, C. L., and S. Attinger. A critique on combining the water stress function with root density distribution to find vertical water uptake profiles in SVAT models. subm. to Earth Interactions.

sphere. A number of models deal with the estimation of water uptake for given environmental conditions, of which SVAT (surface vegetation atmosphere transfer) models are the ones, which are applied at a scale that is relevant for atmospheric scientists, hydrologists and ecologists.

SVAT models were first developed to improve the surface characterization at the lower boundary of Atmospheric General Circulation Models (AGCMs). In the early 80's the role of vegetation in partitioning of energy fluxes into latent and sensible heat was recognized leading to the earliest generation of SVAT schemes. The representation of vegetation and soil was basic, with for example the soil only consisting of one layer, a "bucket". SVAT schemes sequentially introduced more detailed models of soil and vegetation Sellers et al. (1997). Among others, in many SVAT schemes the bucket soil storage was replaced by a layered soil Sellers et al. (1997), and vertical soil water movement between layers calculated using the 1-dimensional Richards' equation:

$$\frac{\partial \theta}{\partial t} = \frac{\partial}{\partial z} \left(K(\psi) \frac{\partial}{\partial z} (\psi + z) \right) - \varrho(z), \quad (6.1)$$

where θ [—] is the soil water content, t [s] is the time, ψ [m] is the water potential in the soil and $K(\psi)$ [m s⁻¹] is the unsaturated conductivity, which is a function of water potential, and $\varrho(z)$ [s⁻¹] is the depth dependent sink term rate, which corresponds to plant water uptake at a given depth (z [m]). Thus, by introducing a more realistic representation of soil water movement assigning a vertical water uptake profile $\varrho(z)$ became challenging.

It is a sophisticated task since the processes shaping root water uptake are not well understood, partly because measurement of root water uptake profiles is inherently difficult (Hupet et al., 2002; Hupet et al., 2003)

In the meantime, researchers who were forced to implement some model of $\rho(z)$ relied on the intuition that vertical root water uptake is proportional both to soil water content and root abundance. The applied parameterizations differ in detail, but not in the general idea. Table 6.3 lists a collection of popular SVAT schemes, including all those used in AGCMs that contributed to the 2007 report of the Intergovernmental Panel on Climate Change (Randall et al., 2007). It gives the model equations used to derive vertical water uptake profiles. Most models combine a water stress function (Feddes et al., 1976; Tiktak and Bouten, 1992) with a function describing the vertical root profile (Gale and Grigal, 1987; Schenk and Jackson, 2002) by normalizing the latter and multiplying it with the former. Both can be derived from measurements on plants or plant communities, which is theoretically an advantage. The parameter of the stress functions are usually assessed by measuring transpiration and water content of potted plants (Denmead and Shaw, 1962; Gollan et al., 1985; Sinclair et al., 2005). Rooting distributions have been derived for different biomes from extensive databases of root observation (Jackson et al., 1996).

SVAT models have also become popular with affiliated disciplines, like hydrology. This lead to further distribution of the described parameterizations for root water uptake. It is no overstatement that the combination of root

distribution with a stress function has become the standard method for estimating uptake profiles. What is more, rooting density profiles strongly influence modeled transpiration in SVAT models (Mahfouf et al., 1996; Feddes et al., 2001), and influence the results of climate models (Kleidon and Heimann, 1998; Barlage and Zeng, 2004). When the upper, densely rooted layers dry out, transpiration is decreased, even when water is available at depth. This is in contrast to observation, which suggests that root water uptake shifts towards deeper layers when the upper layers dry out and transpiration is maintained (Green and Clothier, 1995; Lai and Katul, 2000; Li et al., 2002).

This discrepancy has already been addressed by some macro scale modelers, for example by including compensation mechanisms to maintain transpiration (Li et al., 2005), others returned to bucket uptake models and optimized the rooting depth to maximize plant performance (Kleidon and Heimann, 1999; Hildebrandt and Eltahir, 2007).

How important is root abundance than for uptake? This question can partly be answered by microscale models of root water uptake. Since the 1960s, soil scientists have developed approaches that calculate water uptake from a microscopic perspective (Gardner, 1960; Cowan, 1965; Jacobsen, 1974). These can be upscaled to the plot scale by taking into account absolute root length (Levin et al., 2007; Schymanski et al., 2008; Siqueira et al., 2008). Application of these upscaled models indicate that water uptake is

not always congruent with the root profile, but shifts to moister layers when densely rooted layers dry out (Levin et al., 2007).

Microscale models give the opportunity to look at uptake at the process scale. Measurements of root distribution indicate consistently that a great majority of roots is located in surface layers (Jackson et al., 1996). This is in contrast to the observations cited above, which show that uptake shifts to deep layers at times scales that are too short for root growth.

In this chapter, we use a microscale approaches to show that rooting density has a smaller influences on macroscopic water uptake than currently applied SVAT parameterizations suggest. For an exemplary case we setup a numerical split root experiment, and calculate water uptake based on the microscopic Richards' equation, which is the best currently available model for microscopic water flow towards roots. We compare the results with the ones obtained using parameterizations we found implemented in SVAT models. We also plot some microscopic approximations of the Richards' equation, which have been recently applied in models of SVAT scheme scale (Schymanski et al., 2008; Lier et al., 2008).

6.2 Background

The uptake parameterizations shown in Table 6.3 use macro scale parameterization for water uptake. However, they can be motivated from the perspective of water flow towards a single root. Root water uptake

only scales with rooting distribution if we make the important assumption, that the water flow towards each individual root segment of unit length ($Q_{rad} [m^3 s^{-1}] m^{-1}$) is the same for all modeled soil layers, i.e.

$$Q_{rad,i} = Q_{rad} \forall i. \quad (6.2)$$

With the above assumption and at first with soil moisture not limiting (for matter of simplicity), the total plant transpiration $T_0 [m^3 s^{-1}]$ is given by

$$T_0 = Q_{rad} l_r^{tot} = \sum_{i=1}^N T_i = Q_{rad} \sum_{i=1}^N l_{r,i}^a, \quad (6.3)$$

where $T_i [m^3 s^{-1}]$ is the transpiration from a layer between depth z_i and z_{i+1} , $l_r^{tot} [m]$ is the total root length and $l_{r,i}^a [m]$ is the accumulated root length in soil layer i with

$$l_{r,i}^a = \int_{z_i}^{z_{i+1}} l_r^a(z) dz = l_r^{tot} \int_{z_i}^{z_{i+1}} P_{l_r}(z) dz, \quad (6.4)$$

Here, $l_r^a(z)$ refers the accumulated root length at depth z and $P_{l_r}(z) [m m^{-1}]$ is the corresponding fraction that ranges between 0 and 1. Under the assumption stated above, Q_{rad} depends on total transpiration demand, and is only a function of depth through the fraction of total root length P_{l_r} at z . Thus, the vertical distribution of the transpiration sink can be written

layerwise as

$$T_i = Q_{rad} l_{r,i}^a = Q_{rad} l_r^{tot} \times \frac{l_{r,i}^a}{l_r^{tot}} = P_{l_{r,i}} T_0, \quad (6.5)$$

where $P_{l_{r,i}}$ is the fraction of total root length that is located in layer i .

In the case where soil water becomes limiting, another variable accounting for soil water stress β_i , (see Table 6.3) can be introduced to a combined stress term (F_i), such that:

$$T_i = F_i T_0. \quad (6.6)$$

All parameterizations given in Table 6.3) rely on this general form, but differ in the representation of F and W .

Remember that the derivation of Eq. (6.5) and (6.6) rely on the assumption that Q_{rad} is exactly the same along the entire root network. In practice, Q_{rad} depends on a number of factors that do vary along the root system, such as the size of the root distance and soil moisture.

In this chapter we show, using different types of microscale models introduced below, that Q_{rad} changes in spite of a constant root length distribution considerably, even in the non-limiting case, and hence, the main assumption stated above cannot hold. The latter implies that the parameterizations in Table 6.3 do not correctly reflect the behavior of root water uptake.

6.3 Methods

For this study, we use a numerical split root experiment described in this section. The experiment is simple, and allows us to look at the uptake process in an isolated fashion. In the following paragraphs we give descriptions of the applied macroscale and microscale models. We limit our investigation to water uptake from two soil compartments since we wish to demonstrate that the combination of a stress function with root distribution may fail to correctly describe the distribution of water uptake already in this very simple case. Our approach can be easily extended to more complex models with more compartments.

The setup of the experiment is depicted in Figure 6.3. The root system of one individual plant is separated into two unequal parts (A and B), which are planted into two separate, sealed pots. Part A has a larger total root length than B. The corresponding model consists of two independent soil compartments of the same volume ($V_i = 0.5m^3$), but different root length density. Since the pots are sealed and not in contact, there is no water flow between them or in and out of them. The only extraction is from root water uptake. The total water extraction from each pot is calculated similarly as in Eq. (6.5), except that Q_{rad} may differ between compartments and takes a new variable name $Q_{rad,i}$. Thus Eq. (6.5) becomes:

$$T_i = Q_{rad,i} L_{r,i}. \quad (6.7)$$

The distribution of $\mathcal{Q}_{rad,i}$ between compartments A and B is not prescribed. We only prescribe total (potential) transpiration from both compartments, which is T_0 and we find the inner boundary condition (i.e. the water potential at the root surface ψ_0 for Models Type I and II or the xylem water potential ψ_x for Type III, see below) for which the criterion $\sum T_i = T_0$ is fulfilled. In order to solve this problem, we have to make the important assumption that the inner boundary condition in both compartments is the same. This corresponds closely to the assumption that the xylem water potential within the root system is almost constant in space (Steudle and Peterson, 1998). We apply the model mainly to conditions where the soil is not limiting the uptake, unless indicated differently. We somewhat arbitrarily assume that soil becomes limiting, when the water demand cannot be satisfied at a soil-root-interface potential ψ_0 that is somewhat below the permanent wilting point (-160 m). When this point is reached, we fix $\psi_0 = -160\text{ m}$ in both compartments.

6.3.1 Microscale Models Type I, Richards' equation for flow towards a single root

The most comprehensive method for calculating water flow towards a single root is a small scale, radial symmetric application of the Richards' equation

$$\frac{\partial \theta}{\partial t} - \frac{1}{r} \frac{\partial}{\partial r} \left(r K(\psi) \frac{\partial \psi}{\partial r} \right) = 0, \quad (6.8)$$

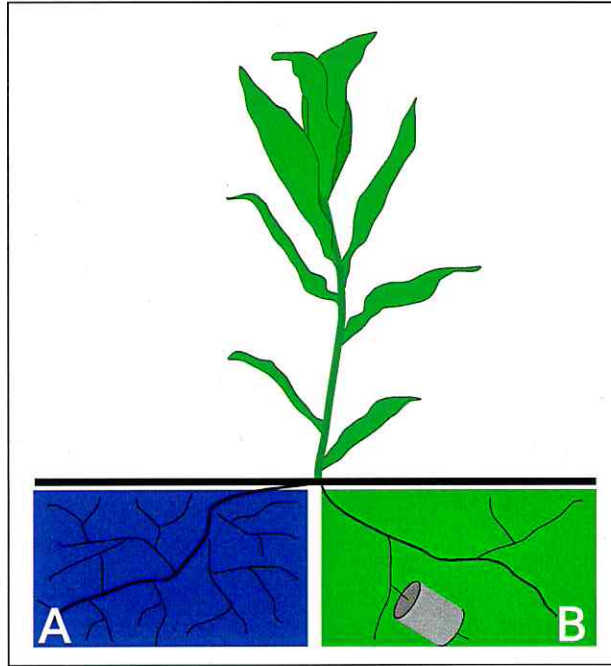


Figure 6.1: Scheme of the numerical split root experiment. We model two independent soil layers, where the water extraction is modeled with an embedded microscale model for flow towards a single root. For this, the soil volume of each layer is explored with one soil cylinder (example in gray) of radius r_d and length $l_{r,i}^a$. Assuming ideal packing, the radii of the cylinders belonging to compartment A and B are related like $r_{d_1}:r_{d_2} = 1:2$, and the cylinder length $l_{r_1}^a:l_{r_2}^a = 4:1$.

with initial and boundary conditions, where r [m] is the radial coordinate (the radial distance from the root center). Its range is $r_0 \leq r \leq r_d$, where r_0 is the root radius and r_d the soil disc radius that is equal to half of the average root distance of all roots within a soil compartment.

Assuming ideal packing in layer i , $r_{d,i}$ relates to $l_{r,i}^a$ and the total volume of the soil compartment (V_i) as

$$r_{d,i} = \sqrt{\frac{V_i}{\pi \cdot l_{r,i}^a}}. \quad (6.9)$$

Root water uptake per root segment of unit length ($Q_{rad,i}$, m^2/s) is given as the flow across the inner boundary (r_0)

$$Q_{rad} = 2\pi r \left(K(\psi) \frac{\partial \psi}{\partial r} \right) \Big|_{r=r_0}, \quad (6.10)$$

imposed by a Dirichlet boundary condition, with $\psi(r_0) = \psi_0$, where $\psi(r_0)$ is the potential at the soil-root-interface. The outer boundary condition is $\varrho|_{r=r_d} = 0$.

Currently, no analytical solution for this nonlinear equation is available, and it therefore has to be solved numerically. Thus, although Richards' equation is the most adequate formulation for modeling flow towards a single root, it is not applicable on the scale of SVAT models, because of the computational burden. We used the software COMSOL (COMSOL AB)

to solve Eq. (6.8) numerically for the water flow towards the root segment per length Q_{rad} .

6.3.2 Microscale Model Type II: Simplifications for flow towards a single root

Microscopic models have recently been applied to model water uptake at the plot scale (Levin et al., 2007; Siqueira et al., 2008; Schymanski et al., 2008; Lier et al., 2008). All these models are approximations of the Richards' equation. A recent review of microscopic approaches to modeling root water uptake has been published by Feddes and Raats (2004) and Raats (2007). We restated the two most relevant equations (the Gardner model and the Steady Rate Approximation) in Table 6.4 and refer the reader for more background to Feddes and Raats (2004), Raats (2007) and the related literature. The Gardner model solves for the water flow per unit length $Q_{rad,i}$ to a root segment, while the Steady Rate Approximation solves for the uptake T_i from a given soil volume.

6.3.3 Microscale Model Type III: Inclusion of root radial resistance

In the approaches above, the inner boundary condition is given at the root surface. In reality however, it is the pressure inside the root (inside the xylem vessels, ψ_x), which drives the water flow towards the root. The

impedance to water flow within the root (from root surface to xylem) is called root radial resistance and can, under certain circumstances, have substantial influence on the distribution of water uptake (Levin et al., 2007). The radial flow through the root can be described in analogy to Ohm's Law, using the root radial conductivity (K_{pr} [$m s^{-1}$]), thus

$$q_{rad,i} = K_{pr} \frac{(\psi_{0,i} - \psi_x)}{r_c}, \quad (6.11)$$

with r_c the radial thickness of the root cortex for all segments of layer i and $\psi_{0,i}$ is the water potential at the soil-root-interface. Using the inverse of root radial hydraulic conductivity $1/K_{pr} = \chi_{pr}$, we multiply this radial root hydraulic resistivity χ_{pr} [sm^{-1}] with the roots radial thickness resulting in ζ_p , an empirically obtained specific root resistance.

The radial uptake per root segment perimeter $Q_{rad,i}$ [$m^2 s^{-1}$] is then given by

$$Q_{rad,i} = \frac{2\pi r_0}{\zeta_r} \cdot (\psi_{0,i} - \psi_x). \quad (6.12)$$

Note that, while in the previous section ψ_0 was the same for all modeled layers, now it can differ between compartments, since it depends on $Q_{rad,i}$. Instead, ψ_x is the same for both layers. Measured specific root resistances range from $1.5 - 35 \times 10^6$ MPa sm^{-1} (Zwieniecki et al., 2003) to 1×10^7 MPa sm^{-1} (Steudle and Peterson, 1998). We chose small specific root resistances

($\zeta_p = 3 \times 10^6 \text{ MPa } sm^{-1}$, which corresponds to a radial conductivity of $K_{pr} = 2 \times 10^{-11} m s^{-1}$).

6.3.4 Special case: root-water uptake for a split root experiment in linear soil

In order to understand the influence of the nonlinear behavior it might be useful to have a model where nonlinearity is removed. Such a model is presented in the following. The solution for this model serves also as a useful benchmark for the numerical simulations. We rely on a simpler, and analytically tangible approximation of the Richards' equation, which is based on the so called matrix flux potential $\Phi [m^2 s^{-1}]$ given in Eq. (5.12), which for the Richards' equation results in

$$\frac{d\theta}{d\Phi} \frac{\partial \Phi}{\partial t} - \nabla^2 \Phi = 0, \quad (6.13)$$

where $\frac{d\Phi}{d\theta}$ is called diffusion coefficient D. If D is a constant, Equation 6.13 reduces to a linear equation and can be solved (see Appendix 6.7 A) in Laplace space, which leads to the following solution for water uptake T_i of layer i

$$T_i = \frac{1}{2\pi j} \int_{c-i\infty}^{c+i\infty} \hat{T}_i e^{st} ds, \quad (6.14)$$

where \hat{T}_i is the Laplace transformed of T_i (given by Eq. (A-6.8) in Appendix 6.7).

6.3.5 Macroscale Model

Table 6.3 gives an overview over common approaches for distributing root water uptake between different soil layers in SVAT models. To give an example, we adopt the approach of MOSES 2.2 (see Table 6.3). We somewhat arbitrarily fix the soil moisture level at which transpiration is first limited to about 30% of fraction of transpirable soil water. This is a level, which has been observed on potted perennial woody species (Sinclair et al., 2005). We assume that θ_w is the water content at wilting point. For the soil type sandy loam, applied in all simulations here, this corresponds to $\theta_c = 0.13$ and $\theta_w = 0.09$. The root length distribution in all scenarios is $l_{r1}^a : l_{r2}^a = 4 : 1$, thus the fraction of total root length for the two compartments is $L_{r,1} = 0.8$ and $L_{r,2} = 0.2$.

6.3.6 Model Scenarios and Input

The soil in all microscopic models is parameterized according to van Genuchten (1980):

$$\Theta = \frac{\theta - \theta_r}{\phi - \theta_r} = \left[\frac{1}{1 + (\alpha\psi)^n} \right]^2, \quad (6.15)$$

$$K(\Theta) = K_s \Theta^{0.5} \left[1 - (1 - \Theta^{1/m})^m \right]^2, \quad (6.16)$$

where Θ is the relative water content ranging from 0 to 1. θ_r is the residual water content, ϕ is the soil porosity, $K(\Theta)$ is the unsaturated and K_s the saturated hydraulic conductivity, α , m and n are parameters listed in Table

Half Root Distance		
	$r_{d,1}$	$r_{d,2}$
small	0.50 cm	1.00 cm
medium	0.75 cm	1.50 cm
large	1.00 cm	2.00 cm
Soil Parameters		
K_s	$1.4 \times 10^{-5} m s^{-1}$	
λ	0.378	
m	$\lambda/(\lambda + 1)$	
n	$\lambda + 1$	
θ_r	0.041	
ϕ	0.453	
α	7.1 m	

Table 6.1: Model input, plant and soil properties

6.1. We chose parameters that correspond to a sandy loam according to the values listed in Maidment (1993).

The initial condition for soil moisture within the two compartments is field capacity (in this soil $\theta_{init} = 0.21$). The total transpiration (T_0) imposed was held constant in the initial phase of the simulation. The resulting distribution of water uptake between layers is calculated as laid out in section 6.3. When the water potential at the root surface or xylem (depending on the model) drops below the permanent wilting point (i.e. $-160 m$), we switch from imposing total transpiration T_0 to imposing constant pressure at the soil-root-interface (ψ_0) or xylem pressure (ψ_x), which is set to $-160m$. We always applied the same ratio of root length for all scenarios

with $l_{r_1}^a : l_{r_2}^a = 4 : 1$, but varied the root distance r_d and thus total root length (see Table 6.1).

6.4 Results

6.4.1 Modeled macroscopic uptake considering only soil resistance with a nonlinear Richards' equation

Figure 6.2 shows the modeled water content (Figure 6.2a), the matric potential (Figure 6.2b) and unsaturated hydraulic conductivity (Figure 6.2c) profiles, for the less densely rooted compartment B. We plotted one profile every 48 hours. At the beginning, the profiles of all variables are flat. After some time, gradients develop first in water potential, later in water content and also unsaturated hydraulic conductivity. As the result of the nonlinear water flow towards the root, hydraulic conductivity (6.2b) is much decreased near the root surface ($r = 0 \text{ mm}$) as compared to further away ($r > 10 \text{ mm}$). Hence, strong potential gradients are necessary to maintain the water flow towards the root (6.2a). The gradients become stronger with time and also depend on the total water demand of the plant and absolute root length density. Figure 6.3 shows how both of these factors influence the total uptake modeled from the two layers compared to total water content (sum of both compartments). For higher total transpirational demand, plants get water limited (i.e. reach $\psi_0 = -160 \text{ m}$) earlier as for low transpi-

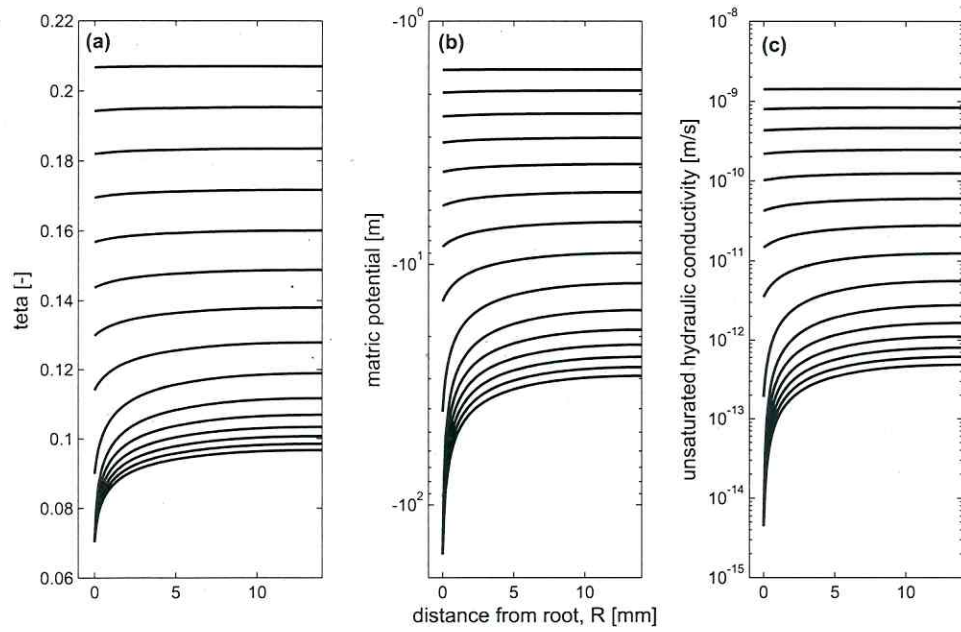


Figure 6.2: Model results for compartment B using the Richards' equation, total transpirational demand is $7 \times 10^{-8} m^3 s^{-1}$. Each line corresponds to the profile of the plotted property at a given time t . The time distance between lines is 2 days, the first (topmost) line is at $t = 0$, the last (bottommost) one at $t = 28$ days. Profiles are (a) water content, (b) matric potential, (c) unsaturated hydraulic conductivity.

rational demand (Figure 6.3a). Also small absolute rooting density (larger root distance, smaller root length) leads to earlier onset of water limitation (Figure 6.3b). In both cases, this is because larger fluxes per root segment require steeper potential gradients around the root, which in turn decrease unsaturated conductivity.

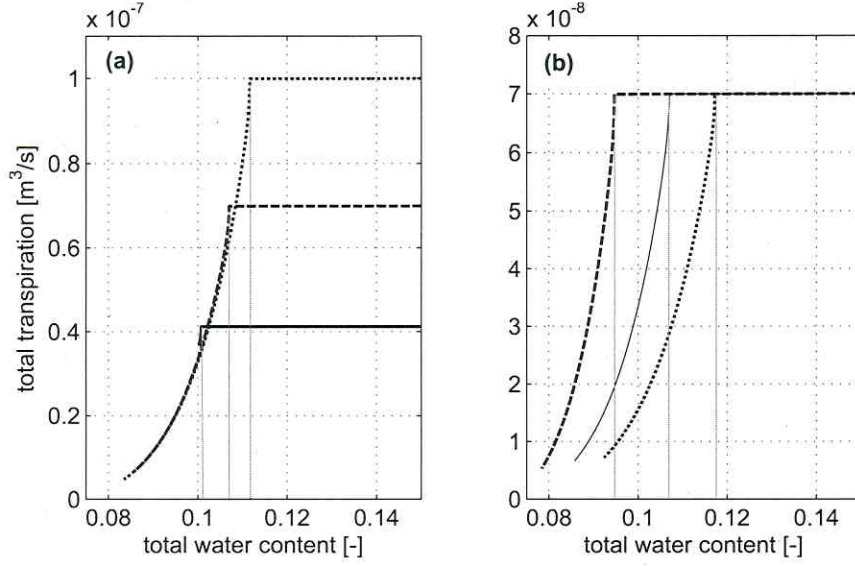


Figure 6.3: Total water uptake from compartments A and B as a function of average water content for different levels of (a) transpirational demand: $1 \times 10^{-7} \text{m}^3 \text{s}^{-1}$ (dotted), $0.7 \times 10^{-7} \text{m}^3 \text{s}^{-1}$ (dashed), and $0.4 \times 10^{-7} \text{m}^3 \text{s}^{-1}$ (solid) and constant half root distance ($r_{d,1} = 0.0075 \text{m}$, $r_{d,2} = 0.015 \text{m}$); (b) varying half root distance $r_{d,1} = 0.005 \text{m}$, $r_{d,2} = 0.01 \text{m}$ (dashed), $r_{d,1} = 0.0075 \text{m}$, $r_{d,2} = 0.015 \text{m}$ (solid), $r_{d,1} = 0.01 \text{m}$, $r_{d,2} = 0.02 \text{m}$ (dotted) and constant transpirational demand ($0.7 \times 10^{-7} \text{m}^3 \text{s}^{-1}$).

Figure 6.4 shows the expected evolution of water uptake separately for compartments A and B, based on the numerical results of the complete nonlinear Richards' equation. For this, we first neglect root radial resistance and return to it later. Imposed critical soil water contents are shown in Table 6.2. Figure 6.4b covers the first hours of the simulation, much before the limiting water potential is reached. During this time, when soil moisture is not yet limiting uptake, current models, based on the bulk water stress formulation, predict water uptake proportional to the root distribution (compared to Eq. (6.5)). This is much in contrast to the results plotted here, where the contribution of uptake from each compartment changes considerably with time. Initially, the ratio of uptake is equal to the ratio of root abundance, but approaches rapidly a ratio of one, that is both compartments deliver the same amount of water, regardless of root length. The equal uptake phase is reached faster for scenarios with larger total root length, but in all considered cases it is fast (less than a day). Figure 6.4 shows that the ratio of uptake between the two compartments changes again after some time: back towards the ratio of root distribution. Also in this case, the timing depends on the actual root length, as stated above. The observed phases are a result of two intertwined processes: (1) the nonlinear nature of soil water flow in the unsaturated zone, and (2) the resulting formation of a depression cone around the root (Figure 6.2).

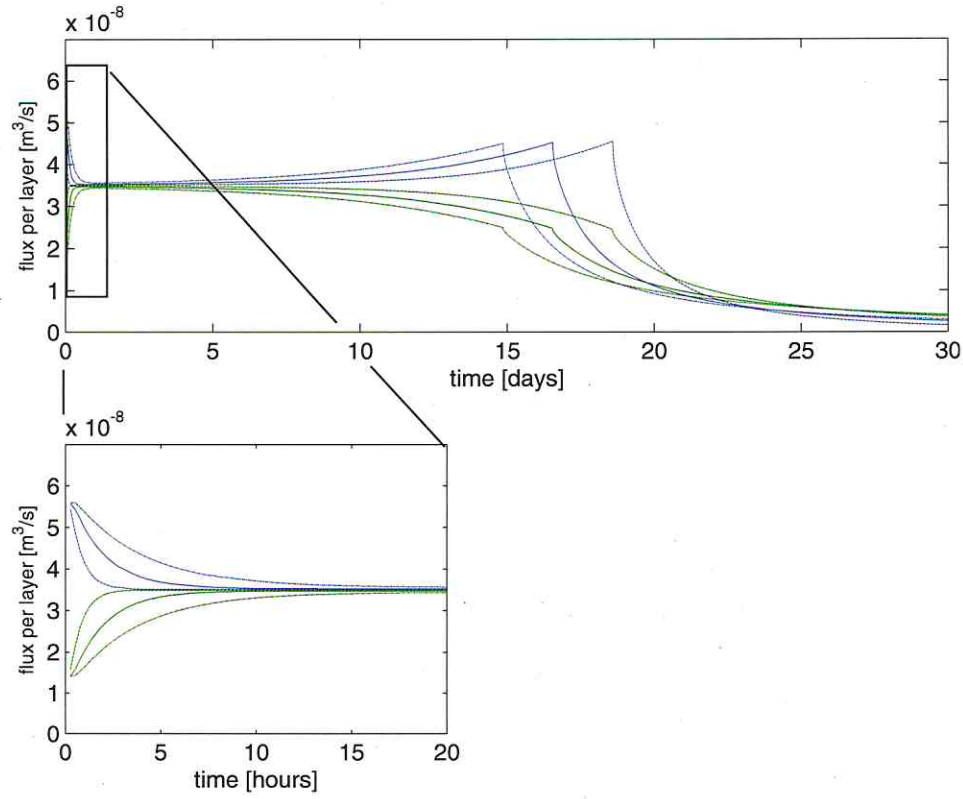


Figure 6.4: Water uptake from densely rooted compartments A (blue) and less rooted compartment B (green) separately for **(a)** the entire modeling period and **(b)** for the first 20 hours and varying half root distance: low ($r_{d,1} = 0.005 \text{ m}$, $r_{d,2} = 0.01 \text{ m}$, dashed dotted), medium ($r_{d,1} = 0.0075 \text{ m}$, $r_{d,2} = 0.015 \text{ m}$, solid), and high ($r_{d,1} = 0.01 \text{ m}$, $r_{d,2} = 0.02 \text{ m}$, dashed).

	low	medium	large
$\theta_{c,1}$	0.09	0.10	0.11
$\theta_{c,2}$	0.10	0.12	0.13

Table 6.2: Soil water content, at limiting soil water content for compartments A and B separately, for the model simulations plotted in Figure 6.4.

6.4.2 Comparison with simplified approaches

Figure 6.5 shows how the simplified microscopic approaches predict the total transpiration and partitioning of transpiration between compartments A and B (described as T_1/T_2), and also gives comparison to the nonlinear Richards' equation and the macroscopic parameterization from MOSIS 2.2. All microscopic models agree with the results for the nonlinear Richards' equation in that they predict that the contribution of the two soil compartments changes with time, and hence, is independent of root length distribution. All models predict that uptake from the compartments is initially proportional to root distribution, but after a short period the uptake from both compartments is the same. In some models (all excluding the linear Richards' equation) the third phase follows, where the curves for water uptake separates again. The degree of separation depends on the model. The nonlinear Richards' equation and the Steady Rate Approach predict the strongest separation: the proportion of water uptake approaches the proportion of roots in each compartment. This separation is a result of the increase of soil resistance from build up of gradients around the roots,

pointed out above. The Gardner model does not account for these gradients and underestimates the soil resistance.

It is noteworthy that the Steady Rate Approach agrees very well with the Richards' solution and is hence an excellent approximation.

The simplicity of the Gardner model offers some insight into the processes leading to the observed dynamics. For the specific case modeled here, the contribution from two different layers can be separated into different factors by dividing the Gardner equation for compartment A by the same equation for compartment B as in

$$\frac{T_1}{T_2} = \frac{\mathcal{B}_1 l_{r,1}^a}{\mathcal{B}_2 l_{r,2}^a} \cdot \frac{K(\psi_1)}{K(\psi_2)} \cdot \frac{(\psi_0 - \psi_1)}{(\psi_0 - \psi_2)} = \mathcal{F}_1 \cdot \mathcal{F}_2 \cdot \mathcal{F}_3, \quad (6.17)$$

where ψ_1 and ψ_2 are the bulk water potentials in compartments 1 (A) and 2 (B). The time evolution of these factors is plotted in Figure 6.6. We see that after a short initial period $T_1/T_2 = 1$, which can only be achieved if the product of \mathcal{F}_2 and \mathcal{F}_3 offsets the constant $\mathcal{F}_1 = 5.4$.

Figure 6.6 shows that this offset is achieved by both factors at different times. During the initial phase, \mathcal{F}_3 decreases abruptly, but increases later again, while \mathcal{F}_2 decreases slowly, and later becomes the dominating factor for offsetting \mathcal{F}_1 . In other words, the nonlinearity of the functions $\psi(\theta)$ and $K(\psi)$ are responsible for the modeled behavior. Again, during the period where the soil conductivity limits uptake, the Gardner model substantially underestimates the soil resistance to water flow, since it only considers

bulk variables and does not account for the gradients around the root. Root length would have a much stronger influence, if K was calculated as function, for example, of the water potential at the root surface (ψ_0), instead of bulk water potential (ψ_i).

The solution obtained with the linear Richards' equation resembles those for the other models qualitatively during the initial phase (Figure 6.5c). After a short time, both compartments contribute equally to total uptake. The reason is the same as shown above for the Gardner model. There are two noteworthy differences. First, the point of equal uptake is reached later for smaller D . Second, there is no separation of uptake from both compartments, as is observed for the nonlinear Richards' equation. These points portray the importance of D in the nonlinear Richards' equation. In the linear Richards' equation $D = \text{const.}$ while in the nonlinear case, $D = D(\theta)$. In the latter case $D(\theta)$ decreases nonlinearly during the uptake, and along the depletion cone around the root (see Figure 6.2). As shown in Figure 6.2 the profile of θ is almost even in the first phase of uptake, hence, D is almost constant over the cross section, and uptake closely resembles the linear Richards' equation ("linear phase"). This corresponds to the time, when uptake from both compartments is almost equal. Later, gradients around the roots develop, also D along uptake cone changes, thus leading to the observed separation of uptake profiles. Thus the crosssectional profile $D(\theta)$, related to the steepness of the local gradients of water content around

the root, plays the key role for unequal contribution from the compartments during the later phase of uptake ("nonlinear phase").

6.4.3 Modulation of macroscopic water uptake by plant factors: plant resistance

In the previous section, we only considered the macroscopic dynamics of water uptake resulting from different formulations of soil resistance, and omitted the influence of plant resistance from the relevant equations. In this section, we include plant resistance, in order to show that the results obtained above still hold, when root radial resistance is included in the model.

Plant resistance introduces more complexity to the uptake model. In particular, the water potential at the root surface depends on the water flow per segment. For example, for water uptake from the densely rooted layer to be equal to the one from the less densely rooted layer, the uptake per root segment in the latter has to be four times as high as in the former. When taking into account root resistance, this disproportion would lead to a larger pressure decrease between xylem and root surface in the less densely rooted layer, and, hence, dampens the pressure gradient within the soil. This again would lead to a comparatively larger influence of root length distribution to the uptake, as already pointed out by Levin et al. (2007).

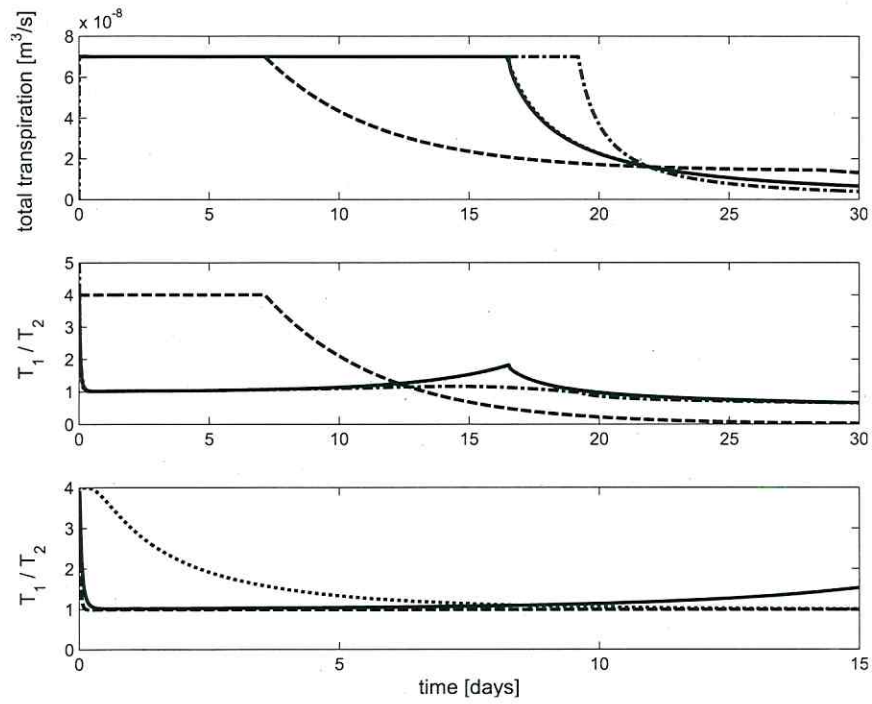


Figure 6.5: Comparison of the water uptake calculated with different microscale models and the macroscale model of CLM (a) Modeled total transpiration over time, (b) Uptake from compartment A divided by uptake from compartment B (T_1/T_2) for default, nonlinear Richards' equation (solid), steady rate (dotted, hidden by the solid line of nonlinear Richards'), Gardner (dashed dotted), MOSIS (dashed), (c) The nonlinear Richards' equation (solid) and the corresponding solution of the linear Model for $D = D(\theta_{FK} = 0.21)$ (dashed) and $D = D(\theta_w = 0.09)$ (solid), which are only plotted for phase where water is not yet limiting uptake. Results are for total transpirational demand $T_0 = 0.7 \times 10^{-7} m^3 s^{-1}$, and medium root distance.

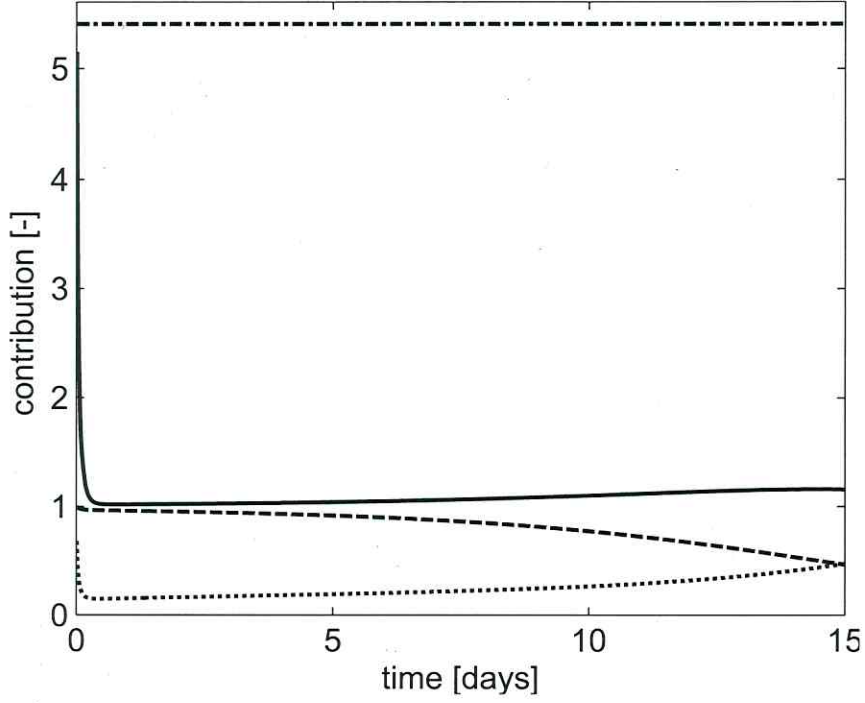


Figure 6.6: Factors contributing to shaping the distribution of uptake between compartments A and B in the Gardner model, for the factors defined in Eq. (6.17), T_1/T_2 (solid), \mathcal{F}_1 (dashed dotted), \mathcal{F}_2 (dashed), \mathcal{F}_3 (dotted). Results are for medium root distance and total transpirational demand $T_0 = 0.7 \times 10^{-7} m^3 s^{-1}$.

We only consider the Gardner equation and nonlinear Richards' equation. The available solution for the linear Richards' equation does not yet allow for taking into account plant resistance, and the Steady Rate Approximation gives the same result as the nonlinear Richards' equation. Figure 6.7 shows the evolution of uptake from both layers with taking into account radial resistance as indicated. The macroscopic uptake changes with time, qualitatively similar to the cases above, with two main differences: (1) the initial phase lasts much longer (the root length density distribution has stronger influence), and (2) during some of the time, the uptake from the less densely rooted layer is more elevated than the one from the more densely rooted one. The latter is a result of the simple model setup and should not be overemphasized. The first is a result of the strongly increasing total resistance to water flow (which is similar to increasing D in the linear Richards' equation as discussed above).

6.5 Discussion

The results of the modeling exercises not including root radial resistance suggest that in moist soil rooting distribution plays only a minor role for determining uptake partitioning between soil compartments. Rather it is the distribution of the soil water potential that determines these profiles. All of the simplified microscopic models agree on this, at least for the case where root radial resistance is neglected. This general behavior agrees with

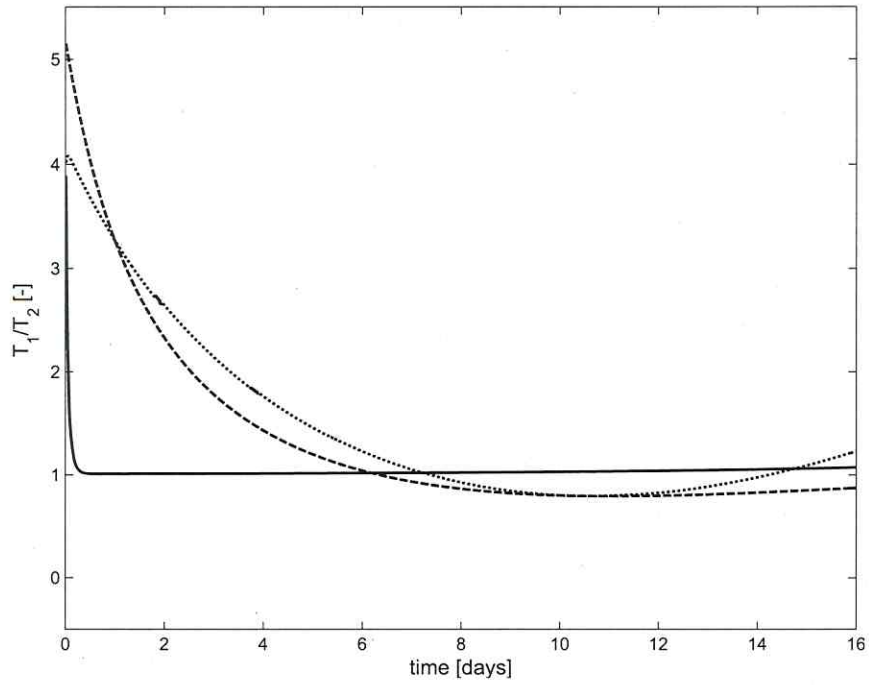


Figure 6.7: Influence of including radial root conductivity to the model result for the ratio of uptake between compartments A and B (T_1/T_2), results of the Nonlinear Richards' equation with radial conductivity (dashed), Gardner model with radial conductivity (dotted) and the original nonlinear Richards' equation without considering radial conductivity (solid).

observations suggesting that the region of active water uptake moves over time (Lai and Katul, 2000; Li et al., 2002; Garrigues et al., 2006). However, nonlinearity in the soil water flow leads to development of strong potential gradients around the root, leading to higher resistance and, hence, the importance of root length increases. This takes place before the water content limits total uptake. The development of these gradients depends also on the total water demand, with higher water demand leading to stronger gradients. The higher water demand leads to an earlier onset of the water-limited uptake phase, in this model due to the stronger decrease in hydraulic conductivity around the roots. This behavior has also been observed in potted plants by Denmead and Shaw (1962).

Some of the SVAT approaches for root water uptake already allow for taking into account experimental results like the ones by Denmead and Shaw (1962). They do this by assuming two critical points for limiting soil moisture (θ_c , see Table 6.3), one for high and one for low transpirational demand. However, our results suggest that θ_c not only changes with transpirational demand, but also with absolute root length (but note: same rooting density profile) and most importantly, θ_c was different in the two soil compartments. In other words, θ_c is not a unique species or soil specific parameter. This implies, that values of θ_c obtained with potted plants cannot be “down-scaled” and applied in discretized soil profiles.

When root resistance is included to the microscale model, the rooting distribution becomes more important, and approaches the uptake modeled by

the MOSIS parameterization. The debate about the magnitude of the root radial conductivity is ongoing. Physiological measurements on root segments indicate that the values could be as low as $4 \times 10^{-11} - 2 \times 10^{-12} \text{ms}^{-1}$ (Zwieniecki et al., 2003) for maize roots. The conductivities applied here ($K_{pr} = 2 \times 10^{-11} \text{ms}^{-1}$) are close to the upper margin of that range. We assume that for lower conductivities the role of root length would increase. Nevertheless, our results show that with inclusion of radial conductivities, the uptake ratios are still not proportional to the rooting distribution and time variant. From this perspective, we would expect that the rooting system adapts to drier soil conditions by increasing root length (not necessarily root biomass). Observation suggests that this might indeed be the case at the ecosystem level (Metcalf et al., 2008).

Most importantly, the behavior of all small scale model predictions differs greatly from those of parameterizations currently applied in SVAT models and summarized in Table 6.3, which predict water uptake during the non-limiting phase to be proportional to the root length distribution. In contrast, the microscopic approaches suggest that the uptake profile is not only different from the rooting density distribution, but that it continually changes in time. Rather than defining the root water uptake profile, the root length distribution acts like an envelope in which the root uptake distribution evolves. The microscopic models show that not only total transpirational demand (6.3a), but more importantly also absolute root length (6.3b) determines the critical point of bulk water content (θ_c), where ac-

tual transpiration deviates from the potential one. This should be taken into consideration when interpreting experimental results in potted plants. However, other factors may play an equal or more important role, such as axial resistance, root growth, and soil-root connection.

With the model exercises above, we aim to show that microscopic root water uptake models deliver important information about the macroscale root uptake behavior. In particular, we want to illustrate from the point of view of unsaturated flow that the root density distribution has a comparatively smaller influence on uptake profiles than the approaches used in SVAT schemes suggest. In this study we intentionally neglected other processes that are important for shaping uptake profiles, like soil water flow within the soil matrix, adaptation of the root length distribution and rooting depth through root growth (Metcalf et al., 2008), soil-root connection (Carminati et al., 2009), and, most importantly, root to shoot signaling (Schachtman and Goodger, 2008). We appreciate the importance of these factors, but we believe that leaving out complexity helps to gain a better understanding of the single process.

In this model we do not consider water flow between soil compartments, which is an approach that researchers have taken earlier to investigate the role of water uptake strategies (Teuling et al., 2006). In moist soil, redistribution of water in the soil matrix interacts with uptake and would likely modify the time evolution of the uptake pattern. However, this was not the focus of this research. We tried to show that the distribution of uptake

between two regions in the soil with a given soil moisture pattern can substantially change in time, even if root length is constant. This result holds, regardless of the origin of the soil moisture pattern.

6.6 Conclusion

Based on applying a microscopic application of the Richards' equation for flow towards a single root, and further simplifications of this model, we strive to show that current parameterizations in SVAT schemes overestimate the water uptake in densely rooted regions versus less densely rooted ones. This even happens for a larger part of non-water-limited uptake. Our analysis is based on investigating the physical environment of the root from a hydrological view point. From that perspective, there is no physical basis for the commonly used parameterizations in SVAT schemes, which distributes uptake according to root length distribution. Other processes, particularly biological ones like root growth, may cause root water uptake to differ even more from observed biome root length distributions.

Climate Model	SVAT	Transpiration	Water Stress	Moisture Availability	Reference
BCC-CM1	BATS	$T_i = T_0 \cdot F_i$	$F_i = \sum_{r=1}^n P_{r,i} (1 - \beta_i)$ only one layer active for transpiration	$\beta_i = \frac{(S_w - p_i)}{(S_w - 1)}$	Min, 2001
BCCR-BCM2.0	ISBA				Mahfouf et al., 1995
CNRM3.1-CM3					
CGCM3.1(T47)	CLASS	$T_i = T_0 \cdot F_i$	$F_i = \frac{P_{r,i} \beta_i}{\sum_{r=1}^n (P_{r,i} \beta_i)}$	$\beta_i = \frac{\psi_w - \psi_i}{\Delta z_i}$	Verseghy et al., 1993
CGCM3.1(T63)					
CSIRO-Mk3.0					
ECHAM5/MP1-OM	MOI-HD				Gordon et al., 2002
ECHO-G					Hagemann and Gates, 2001
CCSM3	CLM3	$T_i = T_a \cdot F_i$	only one layer active for transpiration		Roegner et al., 2007
FGOALS-g1.0	CLM2	$T_i = T_a \cdot F_i$	only one layer active for transpiration		
ODGFDL-CM2.1	LaD	$T_i = T_a \cdot F_i$	$F_i = \frac{P_{r,i} \beta_i}{\sum_{r=1}^n (P_{r,i} \beta_i)}$	$\beta_i = \frac{\psi_w - \psi_i}{\psi_w + \psi_{sat}}$	
GFDL-CM2.0			only one layer active for transpiration		Bonan et al., 2002
GISS-AOM	GISS	$T_i = T_0 \cdot F_i$	$F_i = P_{r,i} \cdot \beta_i$	$\beta_i = \max \left(\frac{\psi_w - \psi_i}{\psi_w}, 0 \right)$	Milly and Shmakin, 2002
GISS-EH	GISS	$T_i = T_a \cdot F_i$	$F_i = P_{r,i} \cdot \beta_i$	$\beta_i = \max \left(\frac{\psi_w - \psi_i}{\psi_w}, 0 \right)$	Abramopoulos et al., 1988
GISS-ER					Rosenzweig and Abramopoulos, 1997
INM-CM3.0		$T_i = T_a \cdot F_i$	$F_i = \frac{P_{r,i} \beta_i}{\sum_{r=1}^n (P_{r,i} \beta_i)}$	$\beta_i = \min(\theta_i - \theta_w, \theta_c - \theta_w)$	Alexeev, 1998
IPSL-CM4	ORCHIDEE		only one layer active for transpiration		Krinner et al., 2005
MICRO3.2	MATSIRO	$T_i = T_a \cdot F_i$	$F_i = P_{r,i}$		Takata et al., 2003
MRI-CGCM2.3.2	SiB		only one layer active for transpiration		Sellers et al., 1986
PCM	LSM1.0	$T_i = T_a \cdot F_i$	$F_i = P_{r,i}$		Bonan, 1996
UKMO-HadGEM1	MOSES	$T_i = T_0 \cdot F_i$	$F_i = \beta_i$	$\beta_i = \frac{\Delta z_i (\theta_i - \theta_w)}{\sum_{r=1}^n \Delta z_i (\theta_i - \theta_w)}$	Cox1999
UKMO-HadCM3	MOSES2.2	$T_i = T_0 \cdot F_i$	$F_i = \frac{P_{r,i} \beta_i}{\sum_{r=1}^n (P_{r,i} \beta_i)}$	$\beta_i = \begin{cases} 0 & \theta_i > \theta_c \\ \frac{(\theta_i - \theta_w)}{(\theta_c - \theta_w)} & \theta_w < \theta_i < \theta_c \\ 0 & \theta_i < \theta_w \end{cases}$	Essery et al., 2001

Table 6.3: Overview of the root water uptake parameterizations used in SVAT models for climate model studies of the IPCC report 2007 (Randall et al., 2007), for matters of simplicity we give the equations only for one plant species, assuming temperatures above freezing. Note: the functional relationship between state variables (like matric potential and water content) varies between models, and is not repeated here. The variable names are: T_i is the transpiration from soil layer i , T_a is the actual transpiration (calculated based on stomatal conductance, which already accounted for water stress), T_0 is the potential transpiration, F_i is a stress term that consists of (either or both) the root fraction $P_{r,i}$ and water stress β_i in layer i , θ_i is the water content and ψ_i the matric potential in layer i , ψ_w corresponds to water potential at the permanent wilting point, θ_c is the water content at which soil moisture starts limiting transpiration, Δz_i is the thickness of layer i .

Name	Equations	Assumptions	Reference
Gardner	Eq. (6.7)	for each time step	Gardner, 1960
	$Q_{rad,i} = B \cdot K(\psi_i) \cdot (\psi_0 - \psi_i)$	$\frac{\partial \theta}{\partial t} = 0$	
	$B = \frac{2\pi}{\ln(r_d/r_0)}$		
Steady Rate	$q_i = \rho_i(\Phi_i - \Phi_0) \cdot \Delta z_i$	for each time step	Jacobsen, 1974
	$\rho_i = \frac{4}{r_0^2 - a_i r_d^2 + 2(r_d^2 + r_0^2) \ln(a_i r_d / r_0)}$	$\frac{\partial \theta}{\partial t} = const$	De Willigen and Noordwijk, 1987
	$a_i = \frac{\bar{r}}{r_d} = 0.62$		Lier et al., 2008
Nonlinear Richards'	Eq. (6.7), (6.10)		
Linear Richards	Eq. (6.14)		

Table 6.4: Overview over the microscopic models applied, equations and relevant references

6.7 Appendix: Derivation of the Linear Split Root Experiment

Together with specified boundary conditions and in radial coordinates, the split root experiment can be written as a systems of equations based on Eq. (6.13) as

$$\frac{\partial \Phi_i}{\partial t} - \frac{D_i}{r} \frac{\partial}{\partial r} \left(r \frac{\partial \Phi_i}{\partial r} \right) = 0, \quad (\text{A-6.1})$$

for each volume V_i , with the following boundary conditions

$$2\pi \sum_i \Delta z_i n_i r \frac{\partial \Phi_r}{\partial r} \Big|_{r=r_0} = - \sum_i T_i = -Q, \quad (\text{A-6.2})$$

$$\Phi_{r=r_0} = \Phi_R, \quad (\text{A-6.3})$$

if $\Phi_i(r = r_0) = \Phi_R \geq \Phi_{crit}$, and

$$r \frac{\partial \Phi_i}{\partial r} \Big|_{r=r_d} = 0, \quad (\text{A-6.4})$$

where $\Delta z_i = 0.5m$ denotes the thickness of the compartment i , and n_i the number of roots in the i th compartment. The system of coupled linear advection-diffusion Eq. (A-6.1) and (A-6.4) can be solved making use of Laplace transforms (Häfner et al., 1992). The fundamental solution for $\hat{\Phi}_i$ reads

$$\hat{\Phi}(s, r) = B_{1k} I_0(p_i r) + B_{2k} \mathcal{K}_0(p_i r) \quad (\text{A-6.5})$$

with $p_i \equiv \sqrt{\frac{s}{D_i}}$ and the parameter s . For a soil comprising two soil layers the four coefficients $B_{11}, B_{12}, B_{21}, B_{22}$ have to be determined making use of the boundary conditions given by Eq. (A-6.2) and (A-6.3) as well as by the no flow boundary condition of each separate layer given by Eq. (A-6.4). It results for the Laplace transformed matrix potential and the root-uptake per layer

$$\hat{\Phi}_i(r_0, s) = \frac{Q}{\pi r_0^2 s} \left[\sum_{i=1}^n (D \Delta z_i p_i) \frac{\mathcal{G}_i(r, s)}{\mathcal{F}_i(r, s)} \right]^{-1}, \quad (\text{A-6.6})$$

$$\hat{\Phi}_i(r, s) = \frac{\mathcal{E}_i(r, s)}{\mathcal{F}_i(r_0, s)} \Phi_i(r_0, s), \quad (\text{A-6.7})$$

$$\hat{T}_i(s) = 2\pi r_0 (D \Delta z_i p_i) \frac{\mathcal{G}_i(r, s)}{\mathcal{F}_i(r, s)} \Phi_i(r_0, s), \quad (\text{A-6.8})$$

$$\mathcal{E}_i(r, s) = \mathcal{J}_1(r_d p_i) \mathcal{K}_0(r p_i) + \mathcal{J}_0(r p_i) \mathcal{K}_0(r_d p_i), \quad (\text{A-6.9})$$

$$\begin{aligned} \mathcal{F}_i(r_0, s) = & \mathcal{J}_1(r_d p_i) \mathcal{K}_0(r_0 p_i) \\ & + \mathcal{J}_0(r_0 p_i) \mathcal{K}_0(r_d p_i), \end{aligned} \quad (\text{A-6.10})$$

$$\mathcal{G}_i(r, s) = \mathcal{J}_1(r_d p_i) \mathcal{K}_1(r_0 p_i) + \mathcal{J}_1(r_0 p_i) \mathcal{K}_0(r_d p_i). \quad (\text{A-6.11})$$

The functions \mathcal{J}_0 , \mathcal{J}_1 , \mathcal{K}_0 and \mathcal{K}_1 denote modified Bessel Functions of the first and second kind. There is no simple back transformation for Eq.(A-6.8). Therefore, we propose the inversion by the numerical algorithm of Stehfest. For further reading we refer to the book of Häfner et al. (1992).

Bibliography

- Abramopoulos, F. et al. (1988). "Improved Ground Hydrology Calculations for Global Climate Models (GCMs): Soil Water Movement and Evapotranspiration". In: *Journal of Climate* 1.9, pp. 921–941.
- Alexeev, Vladimir A. (1998). *Modeling of the present-day climate by the INM RAS atmospheric model "DNM GCM"*. Tech. rep. Moscow, Russia: Institute of Numerical Mathematics.
- Barlage, M. and X. B. Zeng (2004). "Impact of observed vegetation root distribution on seasonal global simulations of land surface processes". In: *Journal Of Geophysical Research-Atmospheres* 109.D9.
- Bonan, G. B. et al. (2002). "The land surface climatology of the community land model coupled to the NCAR community climate model". In: *Journal Of Climate* 15.22, pp. 3123–3149.
- Bonan, Gordon (1996). *A Land Surface Model (LSM 1.0) for ecological, hydrological, and atmospheric studies: Technical Description and*

- User's Guide*. NCAR Technical Note NCAR/TN-417+STR. Boulder, CO, USA: National Centre for Atmospheric Research.
- Carminati, Andrea et al. (2009). "When roots lose contact". In: *Vadose Zone Journal* in press. accepted at Vadoze Zone Journal.
- Cowan, I.R. (1965). "Transport of water in the soil-plant-atmosphere system". In: *Journal of Applied Ecology* 2, pp. 221–239.
- De Willigen, P. and M. van Noordwijk (1987). "Root, Plant. Production and Nutrient Use Efficiency". PhD thesis. Agricultural University, Wageningen, Netherlands.
- Denmead, O. T. and R. H. Shaw (1962). "Availability Of Soil Water To Plants As Affected By Soil Moisture Content And Meteorological Conditions". In: *Agronomy Journal* 54.5, pp. 385–&.
- Essery, Richard et al. (2001). *MOSES 2.2 Technical Documentation*. Hadley Centre technical note 30. Bracknell, Berks, UK: Hadley Centre, Met Office.
- Feddes, R. A. and P.C. Raats (2004). "Parameterizing the soil - water - plant root system". In: *Unsaturated-zone modeling; Progress, challenges and applications*. Ed. by R.A. Feddes et al. Wageningen UR Frontis Series 6. Dordrecht: Kluwer Academic Publishers, pp. 95 –141.
- Feddes, R.A. et al. (1976). "Simulation of field water uptake by plants using a soil water dependent root extraction function". In: *Journal of Hydrology* 31, pp. 13–26.

- Feddes, Reinder A. et al. (2001). "Modeling Root Water Uptake in Hydrological and Climate Models". In: *Bulletin of the American Meteorological Society* 82, pp. 2797–2809.
- Gale, M. R. and D. F. Grigal (1987). "Vertical Root Distributions Of Northern Tree Species In Relation To Successional Status". In: *Canadian Journal Of Forest Research-Revue Canadienne De Recherche Forestiere* 17.8, pp. 829–834.
- Gardner, W. R. (1960). "Dynamics aspects of water availability to plants". In: *Soil Science* 89.2, pp. 63–73.
- Garrigues, E. et al. (2006). "Water uptake by plant roots: I - Formation and propagation of a water extraction front in mature root systems as evidenced by 2D light transmission imaging". In: *Plant And Soil* 283.1-2, pp. 83–98.
- Gollan, T. et al. (1985). "The Responses Of Stomata And Leaf Gas-Exchange To Vapor-Pressure Deficits And Soil-Water Content.3. In The Sclerophyllous Woody Species Nerium-Oleander". In: *Oecologia* 65.3, pp. 356–362.
- Gordon, H.B. et al. (2002). *The CSIRO Mk3 Climate System Model*. CSIRO Atmospheric Research Technical Paper 60. Aspendale, Victoria, Australia: Commonwealth Scientific and Industrial Research Organisation Atmospheric Research. URL: http://www.cmar.csiro.au/e-print/open/gordon_2002a.pdf.

- Green, S. R. and B. Clothier (1995). "Root water uptake by kiwifruit vines following partial wetting of the root zone". In: *Plant and Soil* 173, pp. 317–328. DOI: 10.1007/BF00011470.
- Häfner, Frieder et al. (1992). *Wärme- und Stofftransport: Mathematische Methoden*. Springer-Verlag.
- Hagemann, S. and L. D. Gates (2001). "Validation of the hydrological cycle of ECMWF and NCEP reanalyses using the MPI hydrological discharge model". In: *Journal Of Geophysical Research-Atmospheres* 106.D2, pp. 1503–1510.
- Hildebrandt, A. and E. A. B. Eltahir (2007). "Ecohydrology of a seasonal cloud forest in Dhofar: 2. Role of clouds, soil type, and rooting depth in tree-grass competition". In: *Water Resources Research* 43.11.
- Hupet, F. et al. (2002). "On the identification of macroscopic root water uptake parameters from soil water content observations". In: *Water Resources Research* 38.12.
- (2003). "Estimation of root water uptake parameters by inverse modeling with soil water content data". In: *Water Resources Research* 39.11.
- Jackson, R. B. et al. (1996). "A global analysis of root distributions for terrestrial biomes". In: *Oecologia* 108.3, pp. 389–411.
- Jacobsen, B. (1974). "Water and phosphate transport to plant roots". In: *Acta Agriculturae Scandinavica* 24, pp. 55–60.

- Kleidon, A. and M. Heimann (1998). "Optimised rooting depth and its impacts on the simulated climate of an Atmospheric General Circulation Model". In: *Geophysical Research Letters* 25.3, pp. 345–348.
- (1999). "Deep-rooted vegetation, Amazonian deforestation, and climate: results from a modelling study". In: *Global Ecology And Biogeography* 8.5, pp. 397–405.
- Krinner, G. et al. (2005). "A dynamic global vegetation model for studies of the coupled atmosphere-biosphere system". In: *Global Biogeochemical Cycles* 19.1.
- Lai, Chun-Ta and Gabriel Katul (2000). "The dynamic role of root-water uptake in coupling potential to actual transpiration". In: *Advances in Water Resources* 23 (4), 427–439. DOI: doi:10.1016/S0309-1708(99)00023-8.
- Levin, Anna et al. (2007). "Influence of root resistivity on plant water uptake mechanism, part I: numerical solution". In: *Transport in Porous Media* 70, pp. 63–79. DOI: 10.1007/s11242-006-9084-1.
- Li, K. Y. et al. (2005). "Investigation of hydrological variability in west Africa using land surface models". In: *Journal Of Climate* 18.16, pp. 3173–3188.
- Li, Y. et al. (2002). "The role of soil hydraulic conductivity on the spatial and temporal variation of root water uptake in drip-irrigated corn". In: *Plant And Soil* 243.2, pp. 131–142.

- Lier, Q. de Jong van et al. (2008). "Macroscopic Root Water Uptake Distribution Using a Matric Flux Potential Approach". In: *Vadose Zone Journal* 7, pp. 1065–1078.
- Mahfouf, J. F. et al. (1995). "The Land Surface Scheme ISBA within the Meteo-France Climate Model ARPEGE. Part I. Implementation and Preliminary Results". In: *Journal of Climate* 8.8, pp. 2039–2057.
- (1996). "Analysis of transpiration results from the RICE and PILPS workshop". In: *Global And Planetary Change* 13.1-4, pp. 73–88.
- Maidment, David R., ed. (1993). *Handbook of Hydrology*. McGraw-Hill.
- Metcalf, D. B. et al. (2008). "The effects of water availability on root growth and morphology in an Amazon rainforest". In: *Plant And Soil* 311.1-2, pp. 189–199.
- Milly, P. C. D. and A. B. Shmakin (2002). "Global Modeling of Land Water and Energy Balances. Part I: The Land Dynamics (LaD) Model". In: *Journal of Hydrometeorology* 3.3, pp. 283–299.
- Min, Dong (2001). *The NCC Atmospheric General Circulation Model - Basic Principle and User's Guide*. Beijing, China: China Meteor. Press.
- Raats, P. A. C. (2007). "Uptake of water from soils by plant roots". In: *Transport in Porous Media* 68, pp. 5–28. DOI: 10.1007/s11242-006-9055-6.
- Randall, D.A. et al. (2007). "Climate Models and Their Evaluation". In: *Climate Change 2007: The Physical Science Basis. Contribution of Working Group I to the Fourth Assessment Report of the Intergovern-*

- mental Panel on Climate Change*. Ed. by S. Solomon et al. Cambridge, United Kingdom and New York, NY, USA: Cambridge University Press.
- Roeckner, E. et al. (2007). *The Atmospheric General Circulation Model ECHAM5, Part 1*. MPI Report 349. Hamburg, Germany: Max-Planck-Institut Meteorology.
- Rosenzweig, C. and F. Abramopoulos (1997). "Land-surface model development for the GISS GCM". In: *Journal Of Climate* 10.8, pp. 2040–2054.
- Schachtman, D. P. and J. Q. D. Goodger (2008). "Chemical root to shoot signaling under drought". In: *Trends In Plant Science* 13.6, pp. 281–287.
- Schenk, H. and R. Jackson (2002). "The global biogeography of roots". In: *Ecological Monographs* 72(3), pp. 311–328.
- Schymanski, S. J. et al. (2008). "An optimality-based model of the coupled soil moisture and root dynamics". In: *Hydrology and Earth System Sciences* 12, pp. 913–932. URL: www.hydrol-earth-syst-sci.net/12/913/2008/.
- Sellers, P. J. et al. (1986). "A Simple Biosphere Model (SIB) for Use within General Circulation Models". In: *Journal of the Atmospheric Sciences* 43.6, pp. 505–531.
- (1997). "Modeling the exchanges of energy, water, and carbon between continents and the atmosphere". In: *Science* 275.5299, pp. 502–509.
- Sinclair, T. R. et al. (2005). "Daily transpiration rates of woody species on drying soil". In: *Tree Physiology* 25.11, pp. 1469–1472.

- Siqueira, Mario et al. (2008). "Onset of water stress, hysteresis in plant conductance, and hydraulic lift: Scaling soil water dynamics from millimeters to meters". In: *Water Resources Research* 44.W01432. DOI: 10.1029/2007WR006094.
- Steudle, Ernst and Carol A. Peterson (1998). "How does water get through roots?" In: *Journal of Experimental Botany* 49 (322), pp. 775–788. URL: <http://jxb.oxfordjournals.org/cgi/content/abstract/49/322/775>.
- Takata, K. et al. (2003). "Development of the minimal advanced treatments of surface interaction and runoff". In: *Global And Planetary Change* 38.1-2, pp. 209–222.
- Teuling, A. J. et al. (2006). "Observed timescales of evapotranspiration response to soil moisture". In: *Geophysical Research Letters* 33.23.
- Tiktak, A. and W. Bouten (1992). "Modeling Soil-Water Dynamics In A Forested Ecosystem.3. Model Description And Evaluation Of Discretization". In: *Hydrological Processes* 6.4, pp. 455–465.
- Verseghy, D. L. et al. (1993). "Class - A Canadian Land-Surface Scheme For Gcms.2. Vegetation Model And Coupled Runs". In: *International Journal Of Climatology* 13.4, pp. 347–370.
- Zwieniecki, Maciej A. et al. (2003). "Understanding the Hydraulics of Porous Pipes: Tradeoffs Between Water Uptake and Root Length Utilization". In: *Journal of Plant Growth Regulation* 21, pp. 315–323. DOI: 10.1007/s00344-003-0008-9.

Chapter 7

Effects of root system on plants water uptake ⁴

7.1 Introduction

The global water and carbon cycles are key issues in climate and global change research. Within these complex systems, plants are the central interface between the atmosphere and hydrosphere. Transpiration plays a crucial role for the surface energy balance as well as for the water cycle. It is also linked to the carbon cycle through its close connection with

⁴This chapter is a modified version of the paper: Schneider, C. L., Attinger, S., Delfs, J.-O., and A. Hildebrandt (2009). Implementing small scale processes at the soil-plant interface - the role of root architectures for calculating root water uptake profiles. *Hydrology and Earth System Sciences Discussions*, 6 (3), 4233-4264.

photosynthesis. Hydrological as well as climate models will benefit from an improved understanding of the process of water flow through plants, in particular because they are sensitive to root water uptake parameters (Desborough, 1997; Zeng et al., 1998). Also, great uncertainty in modeling transpiration stems from lack of knowledge about how much water is available to plant roots (Lai and Katul, 2000; Feddes et al., 2001).

Plant water uptake responds to soil moisture limitation at different time and space scales. At the seasonal time scale, plants may adapt their rooting system by root growth, in order to reach moister soil areas (Wan et al., 2002). But also at smaller time scales (like hours to days), plants have been observed to change their uptake zone, and without altering their root system (Sharp and Davies, 1985; Green and Clothier, 1995; Garrigues et al., 2006).

However, models for describing water flow at the soil-plant-atmosphere-interface (SVAT-schemes) include these processes only partially. These schemes use a heuristic parametrization for root water uptake that is applied as a sink in the one-dimensional Richards Equation. Commonly, vertical root water uptake profiles are related to the product of a water stress function and the vertical rooting density distribution (like in Feddes et al. (1976)). However, this parametrization leads to early predictions of limited transpiration, when densely rooted soil layers dry out (Feddes et al., 2001) and thus neglects the plants adaptive response to water stress.

In order to deal with these shortcomings, several algorithms have been developed to allow for a longer period of transpiration in a SVAT context. Li et al. (2001) and Teuling et al. (2006) presented models that compensate water stress in one part of the root zone by increased uptake from other soil areas without altering rooting density profiles. Also, besides compensation effects, another mechanism sustaining transpiration in dry soil, is hydraulic redistribution. It is defined as water transfer from wetter into drier soil areas, via flow through the root system. Recently, Siqueira et al. (2008) and Amenu and Kumar (2008) investigated this effect for delayed onset of water stress in a root water uptake model, again based on rooting density profiles.

The above models treat uptake and adaptation in a lumped way, and therefore do not consider the mechanisms at the scale at which they take place. Models which include more detail could be used to gain the necessary process understanding, in order to transfer it to the SVAT scale. Small scale processes of root water uptake have already been implemented in models of varying levels of complexity.

First level models distribute the transpirational demand on the soil domain simply by the spatial distribution of roots either in one (as SVAT models do), two or three dimensions (Vrugt et al., 2001; Clausnitzer and Hopmans, 1994).

Second level models include a description of microscopic water flow along the potential gradient between the soil and the root, either using an ef-

fective resistance along this gradient like Gardner (1960); Gardner (1964) or more realistic radial dependent soil hydraulic properties (Tuzet et al., 2003; Lier et al., 2006). The latter cover the nonlinear behavior of unsaturated water flow. This is an important mechanism in drying soils (Schröder et al., 2008; Hildebrandt et al., 2009), because steep potential gradients develop around the roots. These models can be extended to include root radial resistance additionally to soil resistance (Siqueira et al., 2008; Schymanski et al., 2008). For example Levin et al. (2007) showed with such a combined model that vertical uptake profiles changed depending on the assumed radial resistance. Schymanski et al. (2008) applied such a model to modify root distribution within biological constraints according to soil water availability.

The approaches above imply that the potential on the side of the root is constant throughout the root system. However, Zwieniecki et al. (2003) suggested in a combined measurement and model study that internal gradients along the root xylem exist. Depending on the ratio between the roots radial and axial resistance, the active uptake region could extend over the entire root or just part of it. This research was conducted only for a single root, but might also be relevant for uptake along the entire root system.

Third level models combine a variable xylem potential distribution along the root structure with the flow processes in the soil domain. One such model was introduced by Doussan et al. (1998). Such root water uptake models can be coupled to three dimensional soil water flow models as done

in Doussan et al. (2006) or Javaux et al. (2008). Simulations with these detailed models show that the region of water uptake moves with time to deeper and moister layers, when top layers dry out. The coupling of soil and root water flow in the vicinity of the root segments was first based on an averaging approach. A finer spatial discretization of the numerical soil grid around the roots (as shown in Schröder et al. (2009)) can represent the local gradients in soil water potential but at the cost of increased computational burden.

In summary, previous research using small scale models for water uptake indicates that both water flow in the soil near the root, but also within the root system itself shape the uptake behavior of the plant. Plant root systems vary greatly in form and morphology, not only between species, but also between individuals of the same species. This chapter contributes to answer the question, how does this variety influence the expected uptake pattern. Therefore, we propose a simplified third level model called aRoot and apply it to simulate the water uptake of an ensemble of root systems of the same species and age. Our model results suggest that water uptake profiles vary significantly between individuals.

7.2 Models and methods

The major assumption for this study is that the process of plant water uptake is gradient driven by the difference between soil water potential and

atmospheric demand. In real plants, this leads to a distribution of water potentials from the leaves (stomata control) over the trunks to the stem and finally to the root system. Hence, the outer boundaries of the plants water uptake system are the atmospheric water deficit and the soil water potential. In this model exercise, we only consider the part from the soil up to the root collar. Within this study we make a comparison between two model approaches for root water uptake. One approach uses a full 3D Richards Equation (see Section 7.2.1) coupled to the classical root length density approach combined with the Feddes reduction function (Section 7.2.4) to simulate soil water stress effects on root water uptake. The other approach again uses the 3D Richards Equation to model the bulk soil water flow combined with a smaller scale water uptake model called “aRoot” (Section 7.2.2). This “aRoot” model was divided into two scenarios of different root hydraulic parameterizations.

7.2.1 Bulk water flow in the unsaturated zone

The Richards’ equation describing the water movement in the soil system is known as

$$\frac{\partial \theta}{\partial t} = \nabla [K \nabla (\psi_{soil} + z)] - \varrho(x, y, z, t), \quad (7.1)$$

where $\theta [m^3 m^{-3}]$ is the volumetric soil water content, $\varrho [m^3 m^{-3} s^{-1}]$ is the sink term rate delivered by the root water uptake model (see Eq. (7.22) for the aRoot approach of volumetric flow rates) and $t [s]$ is time. The

numerical solution of the Richards Equation for bulk soil water flow is provided by GeoSys (Kolditz et al., 2008).

Volumetric soil water saturation θ is defined as a function of the soil water potential ψ_{soil} [m] and can be expressed by the Mualem-van-Genuchten parametrization (van Genuchten, 1980) as

$$\frac{\theta - \theta_r}{\phi - \theta_r} = \Theta = \left[\frac{1}{1 + |\alpha_G \psi_{soil}|^{n_G}} \right]^{m_G}, \quad (7.2)$$

where Θ is the normalized (or relative) water content, ϕ is the porosity of the soil and θ_r the residual volumetric water content (at so-called permanent wilting point), where α_G , n_G and m_G are soil specific parameters (see Table 7.2). K [$m s^{-1}$] in terms of normalized (or relative) water content Θ is then given by

$$K(\Theta) = K_s k(\Theta) = K_s \Theta^{\lambda_G} \left(1 - \left(1 - \Theta^{\frac{1}{m_G}} \right)^{m_G} \right)^2, \quad (7.3)$$

where Θ can be replaced by ψ_{soil} using Eq.(7.2). The saturated hydraulic conductivity K_s as well as the bulk soil porosity ϕ are given in Table 7.2. Accounting for the effect of root segments exploring a certain soil volume, within our model the porosity ϕ of all soil grid cells is decreased by the corresponding fraction of volumetric root content. This is motivated by the fact that as root volume increases in a soil volume, there is less pore

Symbol	Units	Description
r	m	radial distance
x, y, z	m	cartesian coordinates
l_r	m	root segment length
t	s	time
ψ	m	matric potential
Φ	m^2/s	matric flux potential
θ	m^3m^{-3}	volumetric water content
J, T, S	m^3/s	volumetric flow rates
K	m/s	hydraulic conductivity
R	s/m^2	hydraulic resistance
κ	m^2/s	hydraulic conductance
L_V^a	$[m/m^3]$	accumulated root length per volume (RLD)
RLD		root length density
RWU		root water uptake

Table 7.1: List of Variables and Abbreviations.

space for water to occupy. The resulting reduction of porosity was in all realizations relatively low (up to 5 % in some soil voxels)

7.2.2 The hydraulic root water uptake model “aRoot”

In the following, we present a stand alone root water uptake model called aRoot, which calculates the sink term for the bulk soil water flow model. Since we apply an analytical expression for the radial water flow towards the root, our model concept does not require intense iteration between the bulk water flow model and aRoot for each time step.

Water flow within the root system Water flow within the plants takes place as a flow from root surface to the inner root xylem (radial) and along the xylem tubes (axial). The hydraulic uptake model applied to the root system is spatially explicit consisting of a network of root segments. Each individual root segment is modeled as a series of axial and radial resistances similar to Doussan et al. (1998). These root resistances operate as an effective value for the underlying processes, like xylem development for the axial pathway and radial connectivity within the root cortex and epidermis (as described in Steudle and Peterson (1998) as the apoplastic, symplastic and transcellular pathways).

Root hydraulic properties are assigned to each root segment according to their root order given by RootTyp (see Section 7.2.3 and Table 7.2). The axial resistance R_a is calculated by multiplying the axial resistivity per length with the corresponding root length l_r , while the radial resistance R_r is estimated by dividing the specific radial resistivity (material property of each root segment) by root surface area.

The influence of osmotic potential differences are neglected as well as the effect of aquaporins changing the specific radial resistivity per root segment (Steudle, 2000) or the effect of cavitation on xylem vulnerability increasing the axial resistance (Sperry et al., 2003).

For each root segment n the axial flux is implemented by the formula

$$J_{ax}^n = \frac{1}{R_{ax}^n} (\Delta \psi_{xylem}^n + \Delta z^n) , \quad (7.4)$$

where Δ is the potential gradient along the root xylem axis between two root nodes. The radial flux, which is the inflow from the soil to the root segment n is given by

$$J_{rad}^n = \frac{1}{R_r^n} (\psi_{xylem}^n - \psi_{soil}^n(r_0)) , \quad (7.5)$$

with ψ_{xylem}^n denoting the xylem water potential within root segment n and $\psi_{soil}^n(r_0)$ the soil water potential at the root surface of the corresponding soil disc n .

By applying the Kirchhoff's Law for summing up all in- and outflows at a root node, we receive a system of equations describing the water fluxes of the root network that can be best described in matrix notation such as

$$\mathbf{A} \psi_{xylem} = \mathbf{B} \psi_{soil}(r_0) + \mathbf{c} , \quad (7.6)$$

where \mathbf{A} is the system matrix (regarding radial and axial root resistances) coupling root xylem pressure for interlinked root nodes, \mathbf{B} is the input matrix connecting xylem potential to corresponding soil potentials and \mathbf{c} is the offset vector accounting for gravitation (lifting water up over the vertical axis) and the upper boundary condition (flux or potential boundary at root

collar). The boundary condition at the root collar is initially fixed to a given flux T_{Pot} . If the corresponding variable collar potential drops below a critical value ψ_{xylem}^{crit} , then boundary switches to a potential condition and transpirational flux becomes variant.

Rearranging Eq. (7.6) gives

$$\psi_{xylem} = \mathbf{A}^{-1} \mathbf{B} \psi_{soil}(r_0) + \mathbf{A}^{-1} \mathbf{c} . \quad (7.7)$$

By rewriting Eq. (7.5) for all root segments N and introducing the conductance matrix κ_r (main diagonal matrix containing the inverse of the radial resistances $\kappa_r = \text{diag} [1/R_r^0, \dots, 1/R_r^n, \dots, 1/R_r^N]$) as well as new notations $\mathbf{E} = \mathbf{A}^{-1} \mathbf{B}$ and $\mathbf{d} = \mathbf{A}^{-1} \mathbf{c}$ leads to a system of equations for the overall radial fluxes in the root system, namely

$$\mathbf{J}_{rad} = \kappa_r [(\mathbf{E} - \mathbf{I}) \psi_{soil}(r_0) + \mathbf{d}] , \quad (7.8)$$

where \mathbf{I} is the identity matrix of dimension N , the overall number of root nodes. This system can be simplified to

$$\mathbf{J}_{rad} = \mathbf{W} \psi_{soil}(r_0) + \omega , \quad (7.9)$$

where $\mathbf{W} = \kappa_r (\mathbf{E} - \mathbf{I})$ and $\omega = \kappa_r \mathbf{d}$.

The microscopic radial water flow within the soil The microscopic flow towards the root is assumed to be only one dimensional in radial direction towards the root, where the soil domain is modeled as a cylinder of radius r_{disc} and height l_r . Local hydraulic gradients in soil water potential towards the root can be obtained with an approximated analytical solution of the Richards equation (steady state assumption after Jacobsen (1974) and De Willigen and Noordwijk (1987) where the temporal change in water content is assumed to be r independent)

$$\frac{\partial \theta_{soil}}{\partial t} = \frac{1}{r} \frac{\partial}{\partial r} \left[K(\psi_{soil}) r \frac{\partial \psi_{soil}}{\partial r} \right] = const. . \quad (7.10)$$

In matric flux potential notation, this equation becomes an ODE as

$$\frac{1}{r} \frac{\partial \Phi_{soil}}{\partial r} + \frac{\partial^2 \Phi_{soil}}{\partial r^2} = const. , \quad (7.11)$$

with the following solution

$$\Phi_{soil}(r) = \frac{\tau_3}{4} r^2 + \tau_2 \log(r) + \tau_1 , \quad (7.12)$$

where τ_p are integration constants set by boundary/initial conditions.

The matric flux potential Φ_{soil} [$m^2 s^{-1}$] is defined as a function of soil water potential ψ_{soil} by

$$\Phi_{soil}(\psi_{soil}) - \Phi_{soil}^{ref} = \int_{\psi_{soil}^{ref}}^{\psi_{soil}} K(h'_{soil}) dh'_{soil} , \quad (7.13)$$

where Φ_{soil}^{ref} and ψ_{soil}^{ref} are reference states of the system. For $\psi_{soil}^{ref} \rightarrow -\infty$, the reference matric flux potential tends to $\Phi_{soil}^{ref} \rightarrow 0$, so

$$\Phi_{soil}(\psi_{soil}) = \int_{-\infty}^{\psi_{soil}} K(h'_{soil}) dh'_{soil} . \quad (7.14)$$

The solution of this integral depends on the functional form of $K(\psi_{soil})$. Unfortunately, for the Mualem-van-Genuchten parameterization used in our soil water model, no explicit solution is known. Therefore, a closed analytical relationship between water potential h and matric flux potential Φ cannot be established. Nevertheless, within a certain range of h , the matric flux potential can be approximated by the following transfer function

$$\Phi_{soil}(r_0) = b_1 \exp \left(b_2 |\psi_{soil}|^{b_3} + b_4 \right) , \quad (7.15)$$

with b_k soil dependent fitting parameters. For our simulations, the soil parameters b_k of Eq. (7.15) were fitted to the numerical calculated Φ - h -

profile for a sandy soil set up by the Mualem-van-Genuchten parameters given in Table 7.2.

The solution of Equation 7.11 (similar to Lier et al. (2008) or Schröder et al. (2009)) with given boundary conditions (zero flux at outer boundary, radial flux J_{rad} at inner boundary and a given bulk matric flux potential at a certain radial distance r_{Φ_b}) can be written as

$$\Phi(r_0) = \Phi_b + \frac{J_{rad}}{2\pi l} \left(\frac{a^2 - \gamma + \gamma \log(a^2 \gamma)}{2 - 2\gamma} \right) , \quad (7.16)$$

with $\gamma = (r_{\Phi_b}/r_0)^2$, r_0 the root radius, r_{disc} the soil disc radius and $r_{\Phi_b} = ar_{disc}$, where $a = 0.607$ is proposed by Lier et al. (2006). The soil disc radius r_{disc} is linked to the root length in a given soil volume and is set equal for all root segments n within the same voxel.

Hence, the soil water flow corresponding to all root segments is given by the gradient in matric flux potential between the soil-root interface and the bulk soil multiplied with a function determined by the boundary conditions and hence depending on the segment geometry (given by Eq. (7.16)),

$$J_{rad}^n = g^n (\Phi_{soil}^n(r_0) - \Phi_b^n) , \quad (7.17)$$

with

$$g^n = \frac{4\pi l^n (1 - \gamma^n)}{a^2 - \gamma^n + \gamma^n \log(a^2 \gamma^n)} . \quad (7.18)$$

Writing the radial soil water flow in matrix notation for all N segments with G the main diagonal matrix containing the functional terms g^n ($G = \text{diag} [g^0, ..., g^n, ..., g^N]$), we receive

$$J_{rad} = G (\Phi_{soil}(r_0) - \Phi_b) . \quad (7.19)$$

Coupling the root and radial soil water flow The radial root water flow (7.9) and the radial soil water flow (7.19) are set equal (coupled directly via flux type condition)

$$W\psi_{soil}(r_0) + \omega = G (\Phi_{soil}(r_0) - \Phi_b) , \quad (7.20)$$

with Φ given as a nonlinear function of h depending on soil parameters (here given by Eq. (7.15)) resulting in

$$W\psi_{soil}(r_0) + \omega = G (f(\psi_{soil}(r_0)) - f(\psi_b)) . \quad (7.21)$$

This nonlinear system of equations is solved based on a certain bulk water potential and the given root system with its specific boundary condition at the root collar (forming the matrices W , G and the vector ω) leading to a distribution of the water potential at the soil-root-interface $\psi_{soil}(r_0)$.

The sink term for the macroscopic bulk water flow in the unsaturated zone Figure 7.1 shows the model scheme we use to implement the

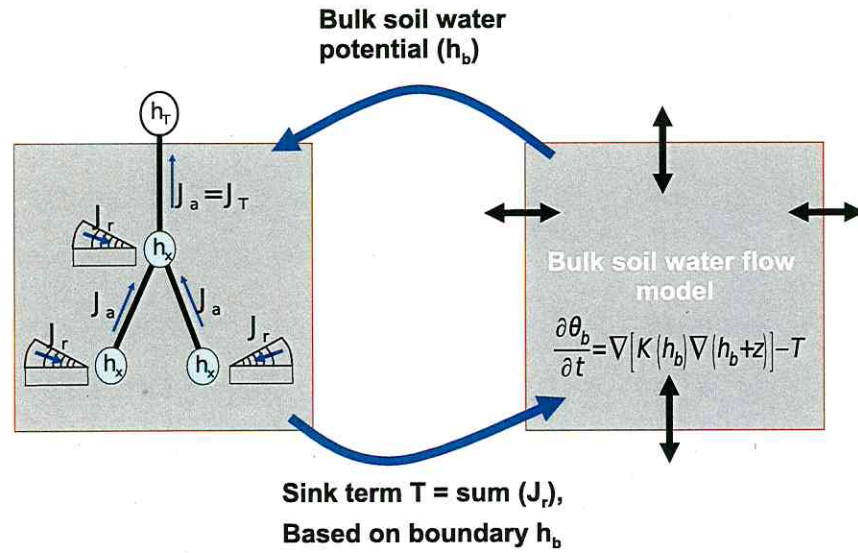


Figure 7.1: Concept of coupling microscale radial flow to bulk flow including xylem potentials for a bulk soil volume Ω_{ijk} .

sink terms into the bulk soil water flow model and how the bulk soil water potential feeds back to the microscale radial soil water flow model. Our concept underlies the assumption that all soil discs around root segments covering a certain soil volume Ω_{ijk} share uniform bulk water potential ψ_b and soil disc radii r_{disc} .

The sink term S for the bulk soil water flow model is calculated by summing up the radial fluxes J_{rad}^m of all soil discs m belonging to a certain bulk soil

volume Ω_{ijk} as

$$\begin{aligned} S(i, j, k) &= \sum_m J_{rad}^m \quad \forall J_{rad}^m \in \Omega_{ijk} \\ \Omega_{ijk} &= \{(x, y, z) \in \mathbb{R}^3 : a_i \leq x \leq a_{i+1}, \\ &\quad b_j \leq y \leq b_{j+1}, c_k \leq z \leq c_{k+1}\}, \end{aligned}$$

with $i, j \in \{1 \dots N_{hor} + 1\} \subset \mathbb{Z}$, $k \in \{1 \dots N_{vert} + 1\} \subset \mathbb{Z}$, where N_{hor} and N_{vert} are the number of bulk soil volumes in the horizontal and vertical direction and the rules for a_i , b_j and c_k are the following

$$\begin{aligned} a_i &= x_{min} + (i - 1)\Delta x; \quad \Delta x = \frac{x_{max} - x_{min}}{N_{hor}}; \\ b_j &= y_{min} + (j - 1)\Delta y; \quad \Delta y = \frac{y_{max} - y_{min}}{N_{hor}}; \\ c_k &= z_{min} + (k - 1)\Delta z; \quad \Delta z = \frac{z_{max} - z_{min}}{N_{vert}}. \end{aligned}$$

7.2.3 The root architecture model

The root architecture model used for our simulations is based on the generic model RootTyp by Pagès et al. (2004). The generator creates realizations of the same species by simulating growth as a random process covering root emission, axial and radial growth, sequential branching, reiteration, transition, decay and abscission. The interplay of these processes is parameterized plant specifically. We used a parameter set for plant species of sorghum type, which is a class of numerous grass species. The size of



Figure 7.2: 2D-plot of two arbitrarily chosen root system realizations created by the root architecture generator RootTyp.

the root system depends on the stage of plant development, hence age. All generated root systems are characterized by their interconnected root segments of a designated order. The order defines the segments axial resistance per length (due to alternating xylem vessel elaboration), specific radial resistivity (due to different stages of suberization) and root radius (see Table 7.2). Figure 7.2 shows exemplary a root system for one of the 50 realizations.

7.2.4 The RLD model

The RWU function of Feddes (like in Feddes et al. (2001)) is the following

$$\varrho(h(x, y, z)) = \beta_{rw}(h) \frac{L_V^a(x, y, z)}{\int_V L_V^a(x, y, z) dV} T_{Pot} , \quad (7.22)$$

with L_V^a [$m\ m^{-3}$] the accumulated root length per volume (RLD) at a point, V the overall volume of the soil-root domain and T_{Pot} [$m^3 s^{-1}$] the potential transpiration flow rate. To get the volumetric flow rate $S(x, y, z)$, the extraction rate (of volume of water per volume of soil per time) ϱ [$m^3 m^{-3} s^{-1}$] has to be applied to a specific soil volume Ω .

The RLD approach includes a water stress function β_{rw} , where the most common implemented stress function has the form shown in Figure 5.1.

7.2.5 Model input and scenarios

The model exercise was divided into three characteristic cases: (1) the classical RLD approach widely applied in current SVAT models, but neglecting the root systems network character as well as the microscopic radial water flow within the soil. That approach was compared for the same root systems to simulations performed with the aRoot model under two scenarios: (2) Scenario A where younger roots (higher order) have higher radial resistances and (3) Scenario B where younger roots have lower radial resistances (see Table 7.2 for those values). The reason for dividing the aRoot model

in two Scenarios (A and B) is the ongoing debate on the range of the radial resistance values (references from Steudle and Peterson (1998); Zwieniecki et al. (2003)).

We performed the simulations for all three cases on 50 root system realizations. The simulation time for root water uptake for all realizations was set to 10 days (with time steps of $\Delta t = 30$ min.) starting from a uniform, initial saturation of $\Theta = 0.4$. The bulk soil water flow model runs on a $2.5 \times 2.5 \times 2.5[cm]$ grid cell size. The overall soil domain size in x -, y - and z -direction is $27.5 \times 27.5 \times 22.5[cm]$ among all root realizations. The plants root system age was set to 1 month (28 days) where there was no further root growth applied within the simulation time.

The transpiration rate was assumed to be time invariant with $T_{Pot} = -8 \times 10^{-10} m^3 s^{-1}$ over the 10 days of unlimited uptake, as long as the root collar potential has not exceeded a given threshold. If the corresponding variable collar potential drops below this critical value ψ_{xylem}^{crit} , then the boundary switches from a flux type to a potential type condition and transpirational flux gets variant.

The specific radial resistance ζ_p (as a material constant for root order k with a given thickness of the roots radial pathway) is assumed to decline with increasing k caused by less suberization, where ζ_p is calculated by multiplying the materials resistivity χ_{pr} with the roots radial thickness r_c . Radial resistance R_r is the ratio of ζ_p to the root outer surface area ($R_r = \zeta_p / (2\pi r_0 l) [sm^{-2}]$). Also, we assume that axial resistance per length

\mathcal{R}_l increases with root order (due to decreasing root radius), multiplied by the root segment length l_r it gives the axial resistance $R_a = \mathcal{R}_l \times l_r [sm^{-2}]$. Parameters of Scenario A are in agreement to measurements by Steudle and Peterson (1998)(page 778): Root properties of segment order 2 are referenced by the mature late metaxylem measurements whereas for root order 4 characteristics are given by the early metaxylem. For Scenario B radial resistance was decreased, but only for higher order roots, so that R_a/R_r is in the range of 0.025 in accordance to the results of Zwieniecki et al. (2003).

7.3 Results

7.3.1 Influence of root architecture and hydraulic root parameters on root water uptake behavior

Figure 7.3 shows the modeled root water uptake (RWU) versus root length density (RLD). The plotted points represent entities on the bulk scale where the RLD was calculated by counting root segment lengths in each bulk soil grid cells and RWU is the given sink term of the bulk soil water flow in Eq. (7.1). We plotted all model runs (50 realizations of each, the classical RLD approach, aRoot Scenario A and aRoot Scenario B) at three different time steps (0, 5 and 10 days).

Root properties				
Segm.	r_0 [m]	ζ_p [s]		\mathcal{R}_l [sm ⁻³]
Order		Scenario A	Scenario B	Scenario A/B
0	0.006 – 0.004	5×10^{10}	5×10^{10}	1×10^9
1	0.004 – 0.003	1.5×10^{10}	1.5×10^{10}	2×10^9
2	0.003 – 0.002	7×10^9	9×10^8	6×10^9
3	0.002 – 0.001	3×10^9	5×10^8	8×10^{10}
4(\geq)	0.001 – 0.0005	1×10^9	1×10^8	1×10^{12}
Soil properties				
θ_{soil}^{init}	0.4	initial soil water status [-]		
θ_{soil}^{PWP}	0.08	permanent wilting point saturation [-]		
van Genuchten parameters for sandy soil				
K_s	1.785	saturated soil water conductivity [$\mu m/s$]		
ϕ	0.46	soil porosity [-]		
α_G	1.44	[1/m]		
λ_G	-0.215	[-]		
β_G	0.534	[-]		
m_G	0.348	$= \beta_G / (1 + \beta_G)$		
n_G	1.534	$= \beta_G + 1$		
RLD model: Feddes water stress function β_{rw} for sandy soil				
ψ_1	-1	[m]		
ψ_2	-2	[m]		
ψ_3	-100	[m]		
ψ_4	-150	[m]		
Boundary conditions				
T_{Pot}	-0.8	potential transpiration rate [mm ³ /s]		
ψ_{xylem}^{crit}	-150	critical xylem water potential [m]		

Table 7.2: Model parameters

For the initial time step plot (Figure 7.3(a)), all model runs provided very similar results. The results of the RLD approach match perfectly the 1:1 line which was expected from the model assumption. For later time steps (Figure 7.3(b) and 7.3(c)), we see that Scenarios A and B of aRoot show some compensation effects: water uptake from areas of higher RLD is decreased and this decline is compensated by increased uptake from lower RLD regions where Scenario B shows a stronger compensation than Scenario A does. Also, at $t = 5$ and $t = 10$ days, the sink terms of the RLD approach and the aRoot Scenarios A and B were comparably similar for higher RLD (between 0.1 and 0.35). Within the range of lower RLD (normalized values from 0 to 0.2), water uptake was highest for the classical RLD model and lowest for Scenario B. However, in the part of lower RLD (up to 0.1) the sink terms for the RLD approach remained mostly at the 1:1 line with no compensational effects. This missing effects are a straight result of the RLD model assumptions.

7.3.2 Influence of root architecture on vertical uptake profiles

In Figure 7.4, we plotted the vertical profiles for RLD and RWU. For this, both variables were averaged over the horizontal soil domain and normalized by the total root length respectively the potential transpiration rate T_{Pot} .

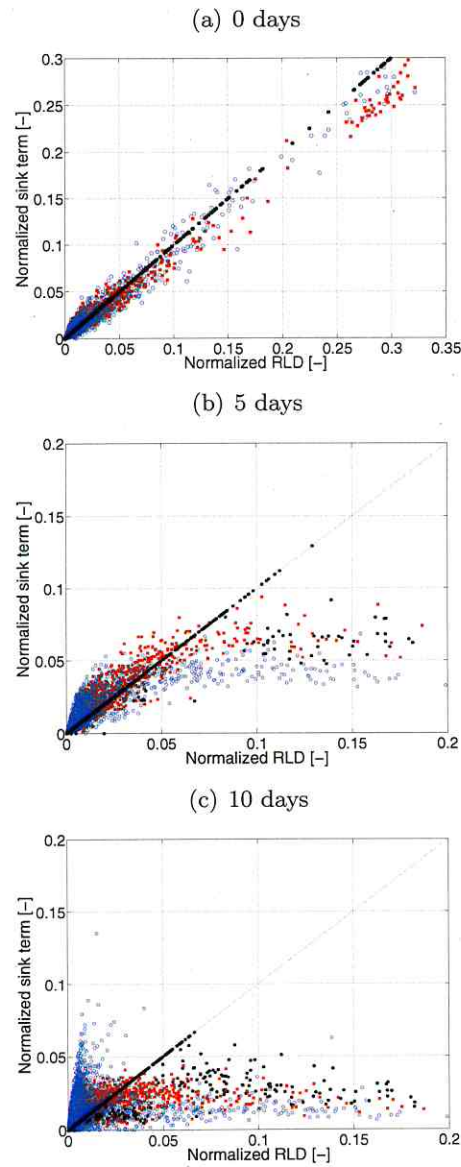


Figure 7.3: Sink term vs. RLD for 50 Realizations of Scenario A (red square), Scenario B (blue circle) and RLD (black dot) at (a) initial time step $t = 0$, (b) after 5 days and (c) after 10 days (sink terms are normalized by the potential transpiration rate T_{Pot} and RLD by total root length).

All 50 root system realizations showed a similar root length density profile resulting in a narrow 90% confidence band. For the aRoot Scenarios A and B, the RWU profiles showed larger confidence bands than the root length density profile. Moreover, during the simulation, the confidence intervals for the water uptake profiles increased in all three cases. The strongest spread could be seen for Scenario B, while the RLD approach showed only very little variation.

At the initial time step, $t = 0$ days, the mean water uptake profile for both aRoot Scenarios was in the range of the mean root length density profile. The confidence bands showed a slightly higher spread for the uptake profiles than for the RLD profiles. At $t=10$ days, the mean uptake at layers with high RLD was for Scenario B only 40% of what would be expected by the RLD profile. At the same time, it was up to 300% higher than RLD at deeper soil layers of lower rooting density. The same trends were observed for Scenario A but with smaller differences between vertical RWU and RLD because of already limited uptake.

Furthermore, the vertical water uptake profiles of Scenarios A and B showed a moving uptake front from layers of high RLD to layers of lower RLD for both scenarios. This shift was faster for Scenario B than for A. Also for Scenario A, RWU was limited earlier than for Scenario B resulting in a slighter compensation of decreased uptake from higher layers (already drier) by increased uptake from lower rooted layers (still wet).

Compared to the aRoot model, we see important differences in the RLD model: at timestep $t = 0$ days the profiles of vertical uptake do perfectly match the RLD profiles as can already be seen in Figure 7.3(a). With time the uptake in the layers of higher RLD decreases but with no compensation of water uptake from less densely rooted layers. The width of the confidence bands remains almost constant in the layers of decreased uptake while they still match the RLD profiles in the nonlimited deeper layers. This general uptake behavior leads to early limitation of water uptake compared to the aRoot model.

7.3.3 Influence of root architecture on critical point of water uptake limitation

Another important factor for modeling root water uptake is the relation between transpirational demand and resulting collar potential (or vice versa). This can only be investigated with a model where xylem potentials are resolved, which is the case for aRoot but not for the classical RLD model. Figure 7.5 shows the evolution of the root collar potentials over simulation time for all 50 realizations. The influence of root radial resistance on collar potential becomes obvious by comparing Figure 7.5(a) (Scenario A) and 7.5(b) (Scenario B). We see that plants in Scenario A would exhibit a more negative xylem pressure than in Scenario B. This is due the larger resistance in the flow path from soil to xylem. The curves also show a high variability

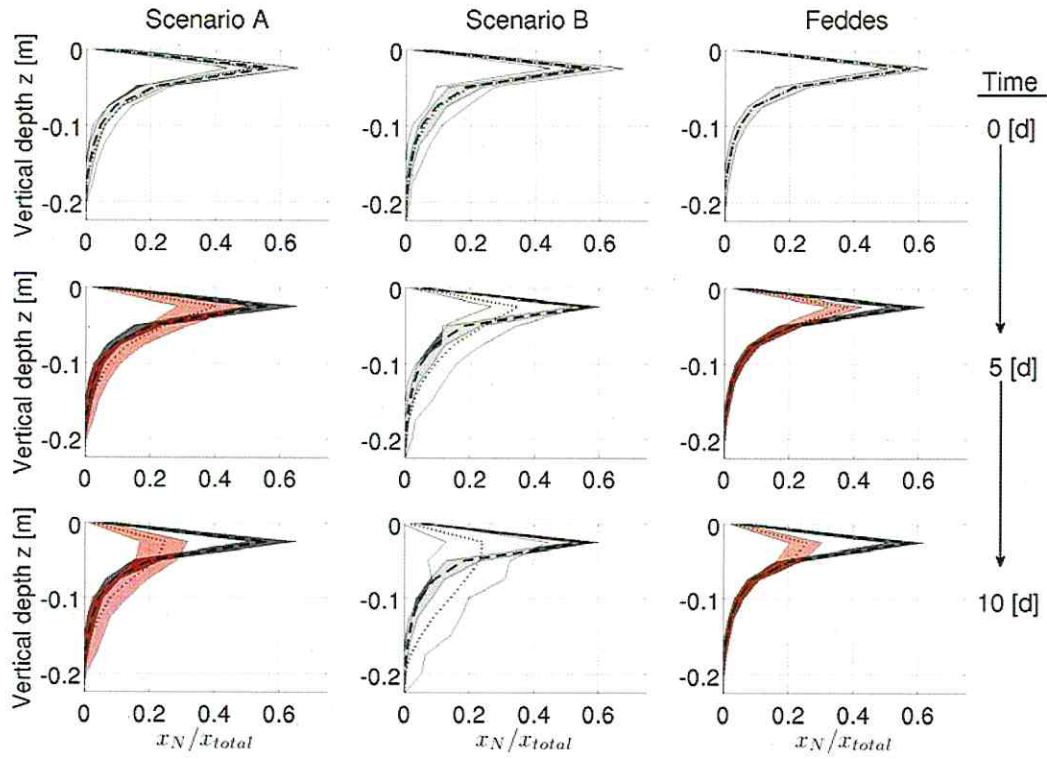


Figure 7.4: Vertical Profiles of RLD (dashed) and RWU (dotted) over soil depth for 50 Realizations of Scenario A (left), B (middle) and RLD (right) at time steps $t = 0$ (up), 5 (middle) and 10 (bottom) days. The dark gray band is the 90% confidence interval for the vertical RLD profile, where the light gray band is the 90% confidence interval for the RWU profile (transparent red bands denote limited water uptake).

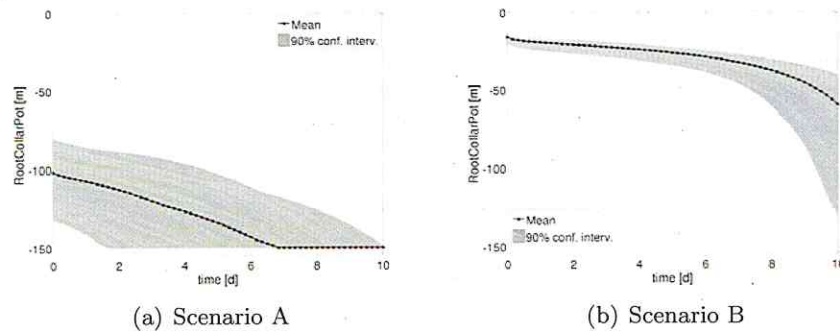


Figure 7.5: Temporal evolution of collar potentials for Scenario (a) A and (b) Scenario B. The black dotted line is the mean xylem water potential at the root collar for all 50 realizations. The gray band denotes the 90% confidence interval and the light gray lines are the individual collar potential curves.

among the realizations for Scenario A where for B, the confidence interval is narrow for most of the simulation. We also see that plants in Scenario A reach the critical point of limited water uptake much earlier than in Scenario B. There, water uptake is still unlimited at the end of the 10 day long simulations for all realizations.

In Figure 7.6, we plotted only for Scenario A mean soil saturation versus resulting actual transpiration. We observed a wide spread of expected water uptake from individual root architectures. While in early limited root systems uptake was reduced by 40 %, other systems were still not limited after 10 days of transpiration.

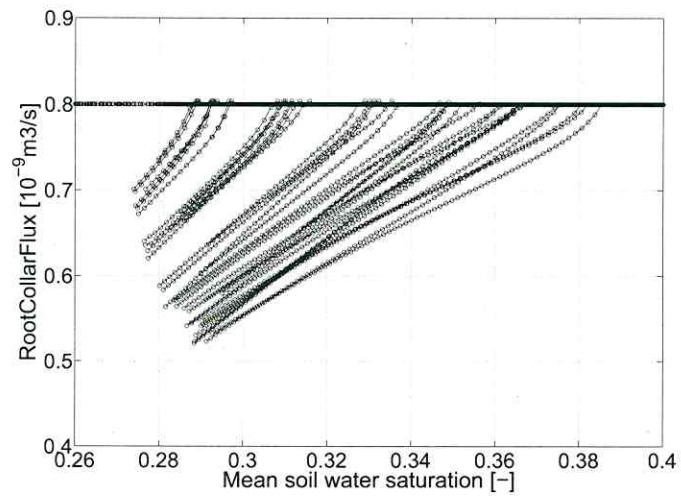


Figure 7.6: Individual collar fluxes (black dotted line) for all 50 realizations of Scenario A over mean soil saturation defined as the integral of the entire soil domain (regarding the soil domain as a simple bucket).

7.4 Discussion

In this model exercise we generated 50 root architectures using the model RootTyp of Pagès (Pagès et al., 2004). These realizations could be interpreted as 50 different individuals of the same plant species and age. The obtained root systems show similar root length density profiles, as indicated by the narrow confidence intervals shown in Figure 7.4. Root length density decreases exponentially with depth for all individuals. This is in accordance to observations not only for grasses, but for all biomes (Schenk and Jackson, 2002).

For these root systems, root water uptake was simulated over 10 days of transpiration by three model cases: the architecture based aRoot model by Scenarios A and B and the root length based approach used in many SVAT schemes. We implemented Scenarios A and B both based on current literature in plant physiology (see Steudle and Peterson (1998); Zwieniecki et al. (2003)). For Scenario A, the specific radial resistivity of higher order roots is set within the higher range, where for Scenario B it is at the lower limit. The model results for both Scenarios differ, but both show a confidence spread over all modeled individuals, either regarding the evolved collar potential and reaching limiting soil water conditions (Scenario A) or regarding the distribution of vertical uptake profiles over soil depth (Scenario B).

While Scenario A gives vertical uptake profiles that do differ less among the 50 realizations than Scenario B, it shows a high variability in xylem

potentials that need to be applied at the root collar. The temporal evolution of collar potential differs among the realizations for Scenario A already at early times, which emphasizes the role of higher root radial resistances. The opposite holds for Scenario B: We see more scatter among the vertical uptake profiles than for Scenario A but less scatter in the evolution of root collar potentials. This variability in the vertical RWU profiles is due to the effects of local soil water depletion. Thus, the influence of root architecture on RWU is either more on the plants side (concerning the temporal evolution of collar potentials, Scenario A) or on the soils side (concerning the vertical uptake profiles, Scenario B).

In our aRoot simulations the modeled root water uptake moves from densely to less densely rooted layers with time. This is in agreement with observation (Garrigues et al., 2006; Lai and Katul, 2000) as well as with results from detailed 3D models for root water uptake ((Doussan et al., 2006; Javaux et al., 2008). Our results suggest that the dynamic of this shift depends on the individual root architecture as well as on root properties (here the range of radial resistances). The classical RLD approach does not show this moving uptake behavior (as the model does not consider such effects) and additionally lacks the scattering in water uptake rates versus RLD caused by root system architecture.

Our simulations show that the occurrence of decreasing water uptake is not at a unique critical point in soil water potential (corresponding to point ψ_3 in Figure 5.1). This was the case, although we used the same soil

environment and same plant species (with similar RLD profiles). Rather, this study shows that root architecture influences the critical point of bulk soil water content where water uptake becomes limiting. The diverse access of the root systems hydraulic active roots to the soil water storage explains this model result. Of course, this results need to be explicitly tested and validated by experimental investigations. However, Javaux et al. (2008) already pointed out, the parameterization based on RLD seems to have little biophysical basis. Our results support this interpretation.

The proposed model aRoot underlies certain assumptions or simplifications. Schröder et al. (2008) has shown, that the local soil hydraulic conductivity drop around the roots becomes important when increasing the size of the bulk soil grid cells. We accounted for this by implementing a microscale radial flow model coupled to the bulk soil water flow. In their model study, Schröder et al. (2009) concluded that for coarser soil discretization, separating the microscale (radial) flow from bulk soil water flow as done in aRoot (similar to their method C) gave the best results compared to fine discretized RWU models. The assumption of uniform bulk water content and soil disc radii for all soil discs covering a certain soil volume is discussed in Lier et al. (2006). Further work would be necessary to quantify the influence of this assumption.

Further on, within the current model version of aRoot no root growth occurs within the 10 days long simulation. Although we have not implemented root growth, our simulations can be regarded as a stepwise analysis of

water uptake related to a certain soil water distribution. Coupling root growth to soil water availability would change the focus of this chapter from the role of root architecture on RWU to adaptivity issues. Nevertheless, root growth can be implemented into aRoot later where we mainly expect changes in estimating the point of water limitation (appearing later) due to root systems adaptation to water stress.

For the field scale, an effective simulation of water uptake by the spatial explicit aRoot model would be computationally very expensive. Nevertheless, application of models such as aRoot can help to identify, what sensitive processes and parameters shape the root water uptake behaviour, beside classical root length density distribution. The model can be applied also for communities of plant individuals, and can be used to find effective parameters at the plant community scale, by horizontally averaging. Thus, complex models like aRoot can contribute to defining alternative field scale approximations.

7.5 Summary and conclusions

In this chapter we developed a simplified model, that captures small scale features of plant-water uptake but is still computationally fast. Although our model currently runs with a 3D Richards Model it is intended for later implementation in SVAT schemes and for testing hypotheses on optimal root behavior in different environments.

With our model, we found a wide range of vertical water uptake profiles even for very similar vertical RLD profiles, which is a result of the individual behavior of each root architecture and its hydraulic parameters. Root architecture becomes more important for the spatial distribution of uptake with time as shown by the increase of confidence bands for the vertical uptake profiles.

The model predictions with the architecture based model aRoot show different behavior than the classical RLD model. The RLD model distributes and limits root water uptake based on two key properties of the plant or plant community: (1) the root length density profile, and (2) the critical point where water uptake starts to be limited by soil moisture (see ψ_3 in Figure 5.1). Our modeling results with aRoot suggest that both of these properties are not suitable for describing the distribution of real water uptake. While the root length density distribution was similar for all 50 root system realizations, root water uptake profiles differed considerably between individuals. This was especially the case, when assuming relatively low values of root radial resistance (scenario B). Also, transpiration started to be limited at a wide range of bulk water contents, particularly for scenario A, where large root radial resistance was assumed.

Our results suggest that root water uptake behavior might vary greatly between individuals of a particular species. More research is necessary to support this conclusion, and to identify such root properties, which are suitable for describing root water uptake profiles. Also, roots have a com-

plex effect on soil hydraulic properties and the flow of water through the soil, especially if the interaction between root growth and the surrounding soil is considered. In case of roots clustering in a certain soil volume this might significantly affect the pore space distribution, further impacting the water holding capacity, pore distribution and soil water movement.

Bibliography

- Amenu, G. G. and P. Kumar (2008). "A model for hydraulic redistribution incorporating coupled soil-root moisture transport". In: *Hydrology and Earth System Sciences* 12, pp. 55–74. URL: www.hydrol-earth-syst-sci.net/12/55/2008/.
- Clausnitzer, V. and J.W. Hopmans (1994). "Simultaneous modeling of transient three-dimensional root growth and soil water flow". In: *Plant and Soil* 164, pp. 299–314.
- De Willigen, P. and M. van Noordwijk (1987). "Root, Plant. Production and Nutrient Use Efficiency". PhD thesis. Agricultural University, Wageningen, Netherlands.
- Desborough, C. E. (1997). "The impact of root weighting on the response of transpiration to moisture stress in land surface schemes". In: *Monthly Weather Review* 125(8), pp. 1920–1930. DOI: 10.1175/1520-0493(1997)125<1920:TIORWO>2.0.CO;2.

- Doussan, C. et al. (1998). "Modelling of the Hydraulic Architecture of Root Systems: an Integrated Approach to Water Absorption - Model Description". In: *Annals of Botany* 81, pp. 213–223.
- Doussan, Claude et al. (2006). "Water uptake by plant roots: II - Modelling of water transfer in the soil root-system with explicit account of flow within the root system - Comparison with experiments". In: *Plant And Soil* 283 (1-2), pp. 99–117. DOI: 10.1007/s11104-004-7904-z.
- Feddes, R.A. et al. (1976). "Simulation of field water uptake by plants using a soil water dependent root extraction function". In: *Journal of Hydrology* 31, pp. 13–26.
- Feddes, Reinder A. et al. (2001). "Modeling Root Water Uptake in Hydrological and Climate Models". In: *Bulletin of the American Meteorological Society* 82, pp. 2797–2809.
- Gardner, W. R. (1960). "Dynamics aspects of water availability to plants". In: *Soil Science* 89.2, pp. 63–73.
- (1964). "Relation of root distribution to water uptake and availability". In: *Agronomy Journal* 56, pp. 41–45.
- Garrigues, Emmanuelle et al. (2006). "Water Uptake by Plant Roots: I - Formation and Propagation of a Water Extraction Front in Mature Root Systems as Evidenced by 2D Light Transmission Imaging". In: *Plant And Soil* 283 (1-2), pp. 83–98. DOI: 10.1007/s11104-004-7903-0.

- Green, S. R. and B. Clothier (1995). "Root water uptake by kiwifruit vines following partial wetting of the root zone". In: *Plant and Soil* 173, pp. 317–328. DOI: 10.1007/BF00011470.
- Hildebrandt, Anke et al. (2009). "A critique on combining the water stress function with root density distribution to find vertical water uptake profiles in SVAT models". In: *Earth Interactions*. subm.
- Jacobsen, B. (1974). "Water and phosphate transport to plant roots". In: *Acta Agriculturae Scandinavica* 24, pp. 55–60.
- Javaux, M. et al. (2008). "Use of a Three-Dimensional Detailed Modeling Approach for Predicting Root Water Uptake". In: *Vadose Zone Journal* 7, pp. 1079–1089. DOI: 10.2136/vzj2007.0115.
- Kolditz, Olaf et al. (2008). "Numerical analysis of coupled hydrosystems based on an object-oriented compartment approach". In: *Journal of Hydroinformatics* 10(3), pp. 227–244. DOI: DOI:10.2166/hydro.2008.003.
- Lai, Chun-Ta and Gabriel Katul (2000). "The dynamic role of root-water uptake in coupling potential to actual transpiration". In: *Advances in Water Resources* 23 (4), 427–439. DOI: doi:10.1016/S0309-1708(99)00023-8.
- Levin, Anna et al. (2007). "Influence of root resistivity on plant water uptake mechanism, part I: numerical solution". In: *Transport in Porous Media* 70, pp. 63–79. DOI: 10.1007/s11242-006-9084-1.

- Li, K.Y. et al. (2001). "An exponential root-water-uptake model with water stress compensation". In: *Journal of Hydrology* 252, pp. 189–204.
- Lier, Q. de Jong van et al. (2008). "Macroscopic Root Water Uptake Distribution Using a Matric Flux Potential Approach". In: *Vadose Zone Journal* 7, pp. 1065–1078.
- Lier, Quirijn de Jong van et al. (2006). "Root water extraction and limiting soil hydraulic conditions estimated by numerical simulation". In: *Vadose Zone Journal* 5, pp. 1264–1277. DOI: 10.2136/vzj2006.0056.
- Pagès, Loïc et al. (2004). "Root Typ: a generic model to depict and analyse the root system architecture". In: *Plant and Soil* 258, pp. 103–119.
- Schenk, H. and R. Jackson (2002). "The global biogeography of roots". In: *Ecological Monographs* 72(3), pp. 311–328.
- Schröder, T. et al. (2008). "Effect of local soil hydraulic conductivity drop using a 3D root water uptake model". In: *Vadose Zone Journal* 7, pp. 1089–1098. DOI: 10.2136/vzj2007.0114.
- (2009). "Implementation of a microscopic soil-root hydraulic conductivity drop function in a 3D soil-root architecture water transfer model". In: *subm. to Vadose Zone Journal*.
- Schymanski, S. J. et al. (2008). "An optimality-based model of the coupled soil moisture and root dynamics". In: *Hydrology and Earth System Sciences* 12, pp. 913–932. URL: www.hydrol-earth-syst-sci.net/12/913/2008/.

- Sharp, R. E. and W. J. Davies (1985). "Root Growth and Water Uptake by Maize Plants in Drying Soil". In: *Journal of Experimental Botany* 36(170), 1441–1456. URL: <http://jxb.oxfordjournals.org/cgi/content/abstract/36/9/1441>.
- Siqueira, Mario et al. (2008). "Onset of water stress, hysteresis in plant conductance, and hydraulic lift: Scaling soil water dynamics from millimeters to meters". In: *Water Resources Research* 44.W01432. DOI: 10.1029/2007WR006094.
- Sperry, John S. et al. (2003). "Xylem hydraulics and the Soil-Plant-Atmosphere Continuum: Opportunities and Unresolved Issues". In: *Agronomy Journal* 95 (6), pp. 1362–1370. URL: <http://agron.sci-journals.org/cgi/content/abstract/95/6/1362>.
- Steudle, Ernst (2000). "Water uptake by plant roots: An integration of views". In: *Plant and Soil* 226, pp. 45–56.
- Steudle, Ernst and Carol A. Peterson (1998). "How does water get through roots?" In: *Journal of Experimental Botany* 49 (322), pp. 775–788. URL: <http://jxb.oxfordjournals.org/cgi/content/abstract/49/322/775>.
- Teuling, A. J. et al. (2006). "Impact of plant water uptake strategy on soil moisture and evapotranspiration dynamics during drydown". In: *Geophysical Research Letters* 33.L03401. DOI: 10.1029/2005GL025019.

- Tuzet, A. et al. (2003). "A coupled model of stomatal conductance, photosynthesis and transpiration". In: *Plant, Cell & Environment* 26.7, pp. 1097–1116. DOI: 10.1046/j.1365-3040.2003.01035.x.
- van Genuchten, M.Th. (1980). "A closed-form equation for predicting the hydraulic conductivity of unsaturated soils". In: *Soil Science Society of America Journal* 44, pp. 892–898.
- Vrugt, J. A. et al. (2001). "One-, two-, and three-dimensional root water uptake functions for transient modeling". In: *Water Resources Research* 37 (10), pp. 2457–2470. URL: <http://www.agu.org/journals/wr/v037/i1010/2000WR000027/>.
- Wan, C. et al. (2002). "Seasonal soil-water availability influences snakeweed root dynamics". In: *Journal of Arid Environment* 51, pp. 255–264. DOI: 10.1016/j.jare.2001.0942.
- Zeng, X. et al. (1998). "The role of root distribution for climate simulation over land". In: *Geophysical Research Letters* 25(24), pp. 4533–4536. URL: <http://www.agu.org/pubs/crossref/1998/1998GL900216.shtml>.
- Zwieniecki, Maciej A. et al. (2003). "Understanding the Hydraulics of Porous Pipes: Tradeoffs Between Water Uptake and Root Length Utilization". In: *Journal of Plant Growth Regulation* 21, pp. 315–323. DOI: 10.1007/s00344-003-0008-9.

Chapter 8

Synthesis

8.1 Summary and Conclusions

Humans extract water from the subsurface water storage mainly by installing wells and pumping groundwater whereas vegetation covers its water demand mainly from the soil water storage. In this dissertation, we hypothesized that singular small scale hydraulic properties close to the water extraction point strongly influences larger scale water removal. Hence, the main focus was to effectively describe and quantify the impact that local heterogeneities and nonlinearities of the hydraulic properties have on the overall water extraction. By local impacts we refer to processes that occur close to the extraction point where strong gradients in water flux evolve.

We reviewed the theoretical aspects of subsurface water flow relevant for this thesis in Chapters 2 and 5. For both groundwater and soil water flow, we illustrated the case of radial flow towards a sink. Groundwater extraction from heterogeneous aquifers was studied in Chapter 3 and 4 whereas root water uptake under unsaturated conditions was investigated in Chapter 6 and 7.

The work described in Chapter 3 and 4 differs by the scale at which the water extraction is studied. By separating the heterogeneity that hydraulic properties approach at multiple scales, we distinguish between small scale and large scale well flows. Small scale well flows explore small scale heterogeneities in the order of decimeters to meters. By definition the affected area of lowered hydraulic heads exhibits only a few meters in the horizontal plane. Hence, the heterogeneity covered by these small scale tests is in the range of the varying hydraulic conductivity field. In addition to those small scale heterogeneities, larger scale heterogeneities may appear on scales up to 100 meters or higher. Pumping the aquifer to such an extent, the draw-down and flow rates will be governed by these heterogeneities.

Correspondingly, both Chapters are based on the distinction between equivalent and coarse grained parameters. We find that applying the derived coarse grained transmissivity (large scale) respectively conductivity field (small scale) gives better estimates for the parameters than commonly used equivalent media approaches. This is because our procedure takes subscale processes, especially in the vicinity of the extracting well, into account. It

is hence not based on an equivalent uniform value. In contrast, the coarse grained field is a radial distance dependent function, which represents both, the drawdown and flow rates across the flow field at the scale of human observation.

Chapter 3 deals with the interpretation of large scale pumping tests in a confined aquifer. The focus was to find an effective description for the flow towards a well, given the spatial heterogeneity of the aquifers properties. By combining a multiscale technique called Coarse Graining with Renormalization Group analysis, we derived an explicit formula for the coarse grained aquifer transmissivity. For an ensemble of pumping tests we see that close to the well the coarse grained aquifer transmissivity equals the harmonic mean of the heterogeneous transmissivity field whereas in the far field the coarse grained transmissivity approaches the geometric mean. The transition between both zones is mainly determined by the correlation length.

However, real pumping tests are usually performed by only installing a single well that pumps water. We show that the performance of a single large scale pumping test is significantly determined by the local hydraulic transmissivity around the well. Therefore, the local transmissivity - and not any upscaled equivalent transmissivity - shapes the pressure drawdown at the well pumping with a prescribed discharge. Our closed analytical formula offers a simple possibility to cover this effect.

Chapter 4 followed the line of interpreting pumping tests, but with the focus on well flows at smaller scales. These tests have to be interpreted in three dimensions, since the vertical extent given by the aquifer thickness is within the same order of magnitude as the horizontal extent. Therefore, the crucial variable is now the hydraulic conductivity, which varies in both the horizontal and vertical direction. However, for small scale well flows the distinction between single and ensemble pumping tests becomes obsolete. Since the hydraulic head measured at a certain observation point can be regarded as either the arithmetic (given head) or harmonic mean (given discharge) of the appearing heads along the boreholes axis, this value represents already the vertical heterogeneity of the aquifer. The proposed method for small scale well flows covers the estimation of the statistical properties of the hydraulic conductivity field. Our estimates for geometric mean, horizontal correlation length, variance and anisotropy ratio are in very good agreement to the values given for a virtual aquifer test.

Chapter 6 and 7 treat subsurface water flow to and through plants describing the physical principles of root water uptake. Compared to the previous Chapters, we still focus on applying a sink term to the flow equation. But for the water flow in the unsaturated zone, the flow equation (Richards' equation) becomes nonlinear since the hydraulic conductivity depends on the soil water potential.

As an outcome of the well flow study, we conclude that the local conductivity in the vicinity of the sink may affect the extraction process significantly.

Whereas this finding within the saturated zone was based on the spatial heterogeneity of the hydraulic properties, we expect this effect to be even more pronounced in unsaturated media due to the local conductivity decrease when soil gets dry. For this reason the methodically focus changed from the parameters' spatial heterogeneity to the nonlinearity in the flow-to-potential relationship.

In Chapter 6 we investigated the influence of local hydraulic gradients around the root in shaping large scale uptake patterns. For this we considered a numerical split root experiment with two soil compartments of same size and hydraulic properties, but different rooting density. We see that while rooting density distribution is the same, the distribution of root water uptake changes considerably with time, particularly for the period when soil moisture is not yet limiting uptake. This is due to the nonlinear nature of water flow towards the roots. Our results show that bulk parameterizations tend to underestimate water uptake from less densely rooted layers.

Additionally to the occurring potential gradients in the vicinity of the root, in Chapter 7 we included another important process on the plant scale that is water flow within the plant and the resulting variation of potentials within the root system. We simulated the water uptake of an ensemble of root system realizations. Our results suggest that root water uptake behavior might vary greatly between individuals of even the same species.

It also turns out that root abundance is not a good proxy for estimating the distribution of root water uptake.

In summary, we showed that singular small scale hydraulic properties close to the water extraction point essentially determine larger scale water extraction. This dissertation contradicts commonly used equivalent media approaches where uniform hydraulic properties are defined to model the large scale behavior. We therefore contribute to the concept that for plant water uptake and aquifer pumping local processes need to be taken into account in order to model the system behavior on the scale of human interaction. We proposed solutions to describe, model and quantify this subscale effects of water extraction from the subsurface and show an improvement of the model prediction at the larger scale.

8.2 Outlook

Regarding groundwater extraction, the proposed solutions for the coarse grained hydraulic property functions can be used for a characterization and parameterization of the heterogeneous aquifer. This is a prerequisite for groundwater modeling in heterogeneous media. A detailed characterization of this heterogeneity is very often neither feasible nor affordable. Based on our findings we consider the methods described in Chapters 3 and 4 as a cheap alternative to the collection and statistical analysis of core samples with the aim to identify correlation lengths of aquifer transmissivities on

large scales or aquifer conductivities on smaller scales. The next step for future work will be to test this method under field conditions, using real long time pumping test data. For this purpose a suitable data set is provided from an environmental test site in Germany (Horkheimer Insel). At this site aquifer heterogeneity has been the subject of previous investigations. Measured grain-size distributions of the aquifer sediments have been used to estimate the spatial distribution of hydraulic conductivity.

Regarding plant water extraction from soil, a first step in future will be the validation of our root water uptake model (called aRoot) against measurements of water uptake by single plants. The developing imaging techniques for rhizosphere studies like Neutron and X-ray tomography are suitable for comparing the modeled and observed water flow and plant uptake mechanisms. Further, we will extrapolate the root water uptake model to a plant community and test if our results also apply there. To do so, the software used (GeoSys for bulk soil water flow and aRoot for root water uptake) needs to be parallelized to overcome the computational burdens for such an extrapolation step. Of course, we want to highlight the need for more research towards understanding, which root system properties, other than root abundance, shape root water uptake profiles. Some particularly interesting questions are: what is the role of hydrogels around roots (Moradi and Carminati, in preparation), and what is the role of shrinking roots (Carminati et al., 2009) or aquaporins (Javot and Maurel, 2002). All these mentioned phenomena may significantly effect the local soil water flow to-

wards the root and hence impact the overall uptake behavior additionally to our findings.

Selbständigkeitserklärung

Ich erkläre, dass ich die vorliegende Arbeit selbständig und unter Verwendung der angegebenen Hilfsmittel, persönlichen Mitteilungen und Quellen angefertigt habe.

18. Dezember 2009, Leipzig

Unterschrift des Verfassers/der Verfasserin

Danksagung

Die Entstehung der vorliegenden Arbeit wäre ohne die uneigennützigste Unterstützung von Kollegen und Freunden nicht möglich gewesen.

Mein besonderer Dank gilt meinen beiden Betreuerinnen Prof. Dr. Sabine Attinger und Dr. Anke Hildebrandt für das ungebrochene Interesse an meiner Arbeit über die letzten 3 Jahre. Ich danke Euch beiden für Eure Diskussionsbereitschaft, Eure Hilfe bei der Ausrichtung und Strukturierung der Gedanken sowie deren versierter Ausformulierung. Diese Arbeit gilt als Versprechen, damit nicht aufhören zu wollen. Die durch meine wissenschaftliche Arbeit möglich gewordenen Besuche der Konferenzen in Montpellier 2007 sowie der AGU 2008 und EGU 2009 werde ich in bleibender Erinnerung behalten. Ich danke Euch beiden dafür.

Für das spontane und gewissenhafte Korrekturlesen möchte ich neben meinen beiden Betreuerinnen auch Sven Arnold und Falk Heße ein herzliches Dankeschön sagen. Für die Unterstützung bei den Zeichnungen ein großes Lob an Emma Eßbach.

Denen, die institutsübergreifend mit mir zusammen geforscht haben, spreche ich ebenso meinen Dank aus, vor allem Jens-Olaf Delfs, Thomas Kalbacher,

Olaf Kolditz, Mathieu Javaux, Tom Schröder, Sascha Oswald, Doris Vetterlein, Ahmad Moradi und Andrea Carminati.

Ich freue mich außerdem das Büro mit Euch zu teilen oder geteilt zu haben: Oliver, Sven, Claudia, Juliane, Hu Yao und zu guter Letzt Falk, der mit mir wohl die meisten Abendstunden in diesem Zimmer verbrachte. Die Zeit, in der sich das Institut leerte und alles ruhiger wurde, war meist die Zeit größter Einsichten. Euch allen vielen Dank. Rohini - either married or unmarried - I would like to visit your home village - I promise we will go there one day.

Ich möchte auch allen anderen Kollegen des Departments Hydrosystemmodellierung danken. Allen voran dem Mann, der sogar eine Woche vor mir am Helmholtzzentrum für Umweltforschung in Leipzig unter Sabines Federführung anfang zu einer Zeit als dieses noch UFZ hieß - Luis, durch dich weiß ich jetzt, dass die Antwort auf die letzte "Wer wird Millionär?"-Frage immer nur Fortran lauten kann.

Mr. Carminati, you misprized captain of poesy, thank you so much. Ihr alle habt für viele Anregungen in meiner wissenschaftlichen Arbeit gesorgt.

Ein großer Dank gilt auch meiner Familie, besonders meinen Eltern - Frank und Margit, Eure Unterstützung war stets ein Anreiz für mich diese Arbeit

fertigzustellen. Ebenso darf meine Großmutter aus Paska nicht unerwähnt bleiben: Omi, ohne deine Weisheit hätte ich diese Arbeit nicht abschließen können. Das geht natürlich nicht ohne einen weiteren Paskaer zu erwähnen - Lutz, ich danke Dir sehr für den Teil, den du an dieser Arbeit trägst.

Bella Andrea, tausend Dank für dein unheimlich großes Verständnis. Ich widme diese Doktorarbeit unserem Murkel.

Curriculum Vitae (deutsch)

Christoph Schneider wurde am 1. September 1980 in Schleiz, Deutschland geboren. Er besuchte das Dr.-Konrad-Duden Gymnasium in Schleiz bis 1999. Im Oktober 2000 nahm er ein Studium an der Technischen Universität Ilmenau auf, dass er im Dezember 2005 erfolgreich mit dem Erlangen des Dipl.-Ing. der Ingenieurinformatik (Gesamtnote: sehr gut) abschloss. Anfang 2006 begann Christoph Schneider als wissenschaftlicher Mitarbeiter am Helmholtz Zentrum für Umweltforschung Leipzig, ab Dezember 2006 war er als Doktorand angestellt. In dieser Zeit fertigte Christoph Schneider am Department für Hydrosystemmodellierung unter Betreuung von Prof. Dr. Sabine Attinger und Dr. Anke Hildebrandt die hier vorliegende Doktorarbeit an. Die Dissertation wurde im August 2009 zur Erlangung des akademischen Grades doctor rerum naturalium an der Chemisch-Geowissenschaftlichen Fakultät der Friedrich-Schiller-Universität Jena eingereicht und am 21. Oktober 2009 ebendort verteidigt.

Curriculum Vitae (english)

Christoph Schneider was born on the 01st of September, 1980 in Schleiz, Germany. He attended Dr.-Konrad-Duden Grammar School in Schleiz until 1999, before perusing further education at the University of Technology Ilmenau from October 2000 on. In December 2005, after completing his Diploma's thesis, he graduated with a Dipl.-Ing. (grade very good) in Computer Science and Engineering. In the beginning of 2006 he started to work as a scientific assistant at the Helmholtz Center for Environmental Research Leipzig, Germany, where he took up the position for his doctoral research in December 2006 at the Department of Computational Hydrosystems under the supervision of Prof. Dr. Sabine Attinger and Dr. Anke Hildebrandt. However, his dissertation was completed in August 2009 and submitted to the School of Chemical and Earth Sciences at the Friedrich Schiller University of Jena, Germany, where the defense took place on the 21st of Octobre 2009.

Helmholtz Centre
for Environmental Research – UFZ
Permoserstraße 15 | 04318 Leipzig | Germany
Internet: www.ufz.de

